NOBLE AND TRANSITION METAL AROMATIC FRAMEWORKS: SYNTHESIS, PROPERTIES, AND STABILITY

A Thesis
Presented to
The Academic Faculty

by

Cantwell G. Carson

In Partial Fulfillment
of the Requirements for the Degree
Doctor of Philosophy in the
School of Materials Science and Engineering

Georgia Institute of Technology
August 2009

NOBLE AND TRANSITION METAL AROMATIC FRAMEWORKS: SYNTHESIS, PROPERTIES, AND STABILITY

Approved by:

Professor Rina Tannenbaum, Advisor
School of Materials Science and Engineering
Georgia Institute of Technology

Professor Rosario Gerhardt, Co-advisor
School of Materials Science and Engineering
Georgia Institute of Technology

Professor Preet Singh
School of Materials Science and Engineering
Georgia Institute of Technology

Professor E. Kent Barefield
School of Chemistry and Biochemistry
Georgia Institute of Technology

Professor R. Bruce King
Department of Chemistry
University of Georgia

Professor Karl Jacob
School of Polymer, Textile & Fiber Engineering
Georgia Institute of Technology

Date Approved: 23 April 2009

To my uncle,

Dr. George Tiller,

whose standard of excellence has ever called me to go further.

ACKNOWLEDGEMENTS

First off, I want to thank my wife for her unflagging support in this endeavour, my advisors for gently cracking whips about my ears and getting me to finish this document, my parents for teaching me by example to strive for excellence in all things, and lastly the Good Lord for letting me get this far.

Beyond that, there were many many people whose assistance was invaluable that I would like to thank. In no particular order they include:

Dr. Kenneth Hardcastle of the Department of Chemistry at Emory University, for solving our crystal structures

Dr. Braga and David Jenson at the School of Chemistry and Biochemistry for maintainance of the EPR equipment and their assistance therewith.

Dr. Christina Hoffmann at the TOPAZ beamline at the Spallation Neutron Source at Oak Ridge National Laboratory, for teaching me how to perform Reitveld refinement, and for putting me in touch with –

Dr. Yu-Sheng Chen at the ChemMATCARS beamline at the Advance Photon Source at Argonne National Laboratory, for his wonderful conversations and for introducing me to chemical crystallography and solving one of my structures.

Dr. Justin Schwartz and Xao-Tao Liu for their assistance measuring our samples at the National High Magnetic Field Laboratory.

Dr. Angus Wilkinson, for allowing us to use his XRD equipment free of charge.

Dr. Brent Carter, for the use of his XPS equipment.

Dr. William Koros and Jason Ward at the School of Chemical and Biochemical Engineering for performing surface area measurement and analysis for us.

Dr. Seung-Soon Jang, Seung-Geol Lee, and Giuseppe Brunello, for helping me better understand the desolvated structure and theoretical underpinnings of computational calculations.

My fellow group members, past and present: Dan Cipiari, Dave Mebane, Melissa Zubris, Jeremy Walker, Kasi David, Run-Qing Ou, Siva Kumar, Erin Camponeschi, Larry Pranger, Surajit

Kumar, Charlie Cappozzi, Lex Nunnery, Chun-Qing Peng, Brian Bertram, Jake Waddell, Rolando Gittens, Jun-Hwa Park, Il-Tae Kim, Salil Joshi, Ricky Whelchel, John Boyea, Will Gibson, Kenter Wu, Shantanu Talapatra, and Laurissa Prystaj.

I would also like to thank the Institute for Paper Science and Engineering at the Georgia Institute of Technology for their generous support of this research.

TABLE OF CONTENTS

LIST OF TABLES

LIST OF FIGURES

SUMMARY

In the first section, the electrical conductivity of rhodium phenylene-diisocyanide polymer is reported to be 3.4×10^{-11} S·cm^{-1}. However, the conductivity also exhibits an inverse exponential decay in air with τ = 8 days. This change is attributed to the oxidation of the isocyanide functional group to an isocyanate, leading to a degradation in the long-range metal-metal bonding, the dominant conductivity mechanism. Using a more stable carboxylate ligand, the Cu terephthalate (TPA) system is studied and compared against the Mg, Co, Ni, and Zn terephthalates. A synthesis in *N*,*N*-dimethylformamide (DMF) is developed and large quantities of the Cu(TPA)·DMF can be synthesized in air. The crystal structure of the Cu(TPA)·DMF is shown to be in the C*2/m* spacegroup. Upon desolvation, the Cu(TPA) is shown to have a large surface area of 625 m^{2}g^{-1}. The magnetic susceptibility of the Cu(TPA) indicates anti-ferromagnetic coupling between adjacent Cu centers in the same dimer. The thermal stability of the Zn, Ni, Co, and Mg terephthalates is shown to increase with decreasing symmetric carboxylate stretch in the IR. The magnetic susceptibilities of the Co and Ni terephthalates have paramagnetic behavior, with a Weiss temperature of Θ = -12.9 K and Θ = 8.8 for Co(TPA)·DMF and Ni(TPA)·DMF respectively. A heterometallic Zn-Cu terephthalate is synthesized with Cu concentrations ranging from 0 to 100%. Upon the addition of Cu, Zn-rich frameworks increase in surface area, change in thermal stability, and increase solvent retention from 16% to 25%. Zn is shown to couple with Cu in the same dimer at a high rate, changing the behavior of the dimer from anti-ferromagnetic to paramagnetic. The Weiss temperature suggests weak ferromagnetic interaction.

CHAPTER I

INTRODUCTION

It would appear that the challenge of the materials chemist is to synthesize that which has useful properties, ease of synthesis, and is environmentally robust. This challenge is visible at the intersection of organic and inorganic chemistry. The field of organometallic chemistry has produced countless compounds that display unique and fascinating properties, yet these often incorporate expensive elements, are difficult to synthesize, and oxidize readily in air. Only in the absence of a more suitable alternative, and with great caution, will such compounds be produced in large scale for application in consumer materials.

1.1 Rhodium diisocyanide

This thesis begins by demonstrating the difficulties that can occur when an organometallic compound is used in a real-world setting. We chose a rhodium diisocyanide polymer that had been shown previously to demonstrate anisotropic electrical conductivity. The work of Rh diisocyanobenzene was originally motivated by an interest in molecular electronics. Interest in molecular electronics has been driven principally by the desire to utilize synthetic molecules and short-chain oligomers as wires [1–4], rectifiers [5], transistors [6], and switches [7]. This research very often entails the use of a "bottom up" approach to the fabrication of microelectronic devices through the intermediacy of self-assembled monolayers (SAM) [1,4,5,8–10]. The advantage of this approach is that molecules on smooth metal surfaces can assemble into specific and regular arrangements. The two-dimensional nature of this approach makes the comparison of the electrical properties of different molecules and substrates fairly straightforward. Moreover, the electrical properties of these potentially conductive molecules have also been examined after being coordinated to individual metal ions in solution. By studying these materials either in the bulk or in the solution phase, it becomes possible to also observe the effects of different architectures and crystal structures on their electrical properties [11–15]. This approach offers a way to explore the discrete behavior and stability of the conduction mechanisms of these organic molecules, which is not otherwise available

with SAM methods.

One of the most promising platforms to probe discrete electrical properties of molecular species is in the context of coordination polymers. These are formed when potentially conducting organic molecules with electron-donor properties are coordinatively bonded to discrete metallic centers to form macromolecular structures. More specifically, coordination polymers represent a class of materials in which bi-dentate, non-chelating ligands act as coordination bridges between metal centers to form polymers having 1, 2 or 3 dimensions, depending on the coordination geometry of the metals [16]. The choice of metallic centers, ligands and substituents allow for flexibility in tailoring the chemical, optical, physical, and electrical properties. As a result, these polymers have attracted attention owing to their potential application in solid state devices and catalytic processes [14]. The class of coordination polymers that contains metal atoms as an integral part of the main chain is of special interest, as this allows us to characterize the effect of structure and chemistry on the electrical properties of the metal-ligand bond.

Coordination polymers are generally insulating. However, conduction bands can be created with the proper choice of ligand, metal center, and the position of that metal center in the polymer chain [17, 18]. For example, the resonance effect of π-conjugated molecules coordinated between metallic centers can generate an effective semi-conducting mechanism. In addition, conduction bands can arise when large numbers of adjacent metal atoms are close enough to promote overlap of their d_{z^2} orbitals. In both scenarios, free electrons can then move from one metal atom to the next or along the π-bonds in the π-conjugated molecular bridges. If there are enough of these atoms or molecules connected in such a fashion, then the conductivity of the material can be greatly increased by the presence of these extended conducting chains [19].

These types of coordination polymers can optimally be synthesized by combining linear, bidentate, rigid ligands with metallic centers having square-planar coordination geometry. For the current study, 1,4-phenylene diisocyanide (pdi) was chosen because of its rigid, π-conjugated backbone and its ability to form strong, linear ligand to metal coordination bonds (acting as an effective π-acid) [16, 20–25]. In addition, the electrical behavior of the metal-isocyanide bond has been a recent area of interest owing to its low conduction barrier [1]. Isocyanides have also been shown to displace CO in metal-carbonyl complexes, which are common precursors for organometallic syntheses [25].

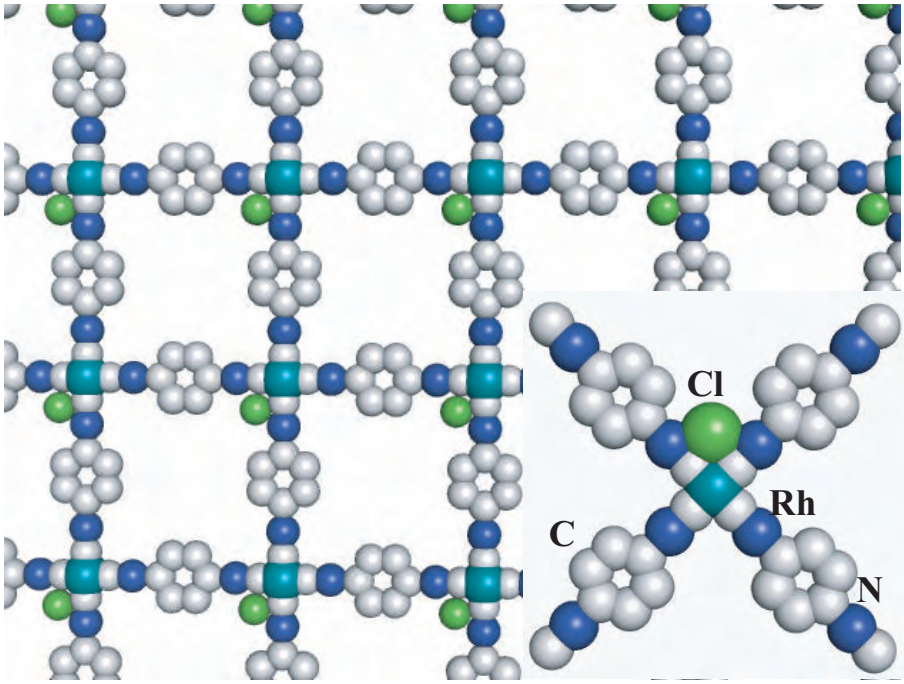

Figure 1.1: A schematic representation of poly-$[Rh(pdi)^{+}_{4/2}(Cl)^{-}]_n$ square planar two-dimensional network. The inset shows a model of a monomer, with atoms labeled [26].

Rh(I) was used as a d_6 metal center because it possesses square-planar coordination geometry and its carbonyl complex precursor is commercially available. The product, poly-$[Rh(pdi)^{+}_{4/2}(Cl)^{-}]_n$ is an ideal test bed for studying the relationship between structure, chemistry, and electrical properties in metal-isocyanide complexes. As the idealized model in Figure 1.1 shows, the reaction between $[Rh(CO)_2Cl]_2$ and pdi creates a sheet-like square grid of Rh(I) atoms separated by rigid pdi ligands. The π-conjugated pdi ligands allow for extended π-conjugation throughout the whole polymer while the weak attraction between metal atoms on adjacent sheets causes polymer sheets to stack, aligning Rh(I) atoms into connected columnar chains [19].

In the absence of intervening factors, this property could become very useful as a sensor or molecular wire. However, as we demonstrate, the ambient environment can interact with the organometallic solid to interrupt this metal-metal bonding and cause the solid to lose the conductivity that made it tantalizing in the first place. Having demonstrated the difficulties associated with organometallic polymers, we then show that some of these difficulties can be overcome by replacing the metal-carbon bond with a more ionic metal-oxygen bond that occurs in metal-organic frameworks (MOFs).

1.2 Metal Organic Frameworks

The term metal organic framework (MOF) describes a class of materials in which organic, polyfunctional ligands form coordination bonds with multiple metal atoms to form extended polymeric structures in one, two, and three dimensions. They are often crystalline, highly porous and resistant to structural collapse upon evacuation [27, 28]. The variation of the ligand character, functionality, spacer length, metal atom, and synthesis environment has given rise to the formation of a large number of porous compounds with a correspondingly large variety of properties and applications [29]. These materials have the capacity to perform great tasks at comparatively low cost. Applications ranging from gas sieving [30], gas storage [31], nonlinear optical materials [32], and catalysis [33] have been investigated using various metal carboxylates.

While the popularity of metal organic frameworks (MOFs) has surged in recent years, MOFs incorporating terephthalic acid (TPA) have been known since at least 1967. Thus a nickel terephthalate compound was being synthesized by Acheson and Galwey [34]. Other hydrated metal terephthalates (Fe, Cr, Co, Cu, Ag, Mn, La) were synthesized by Sherif [35]. It was not until recently; however, that advances in single-crystal diffraction and computational refinement allowed adequate structural determinations of these insoluble crystalline solids. The subsequent ease of structural determination has allowed investigation of metal terephthalates as porous metal organic frameworks (MOFs). Consequently, the number of such structures published in the literature has grown enormously over the past few years, sometimes at the expense of proper attribution. For example, the adduct of a copper salt with terephthalate in water was first reported by Sherif in 1970, but the crystal structure was only later solved by Cueto in 1991 [36].

Early MOFs were synthesized almost completely in water. Their structural collapse upon dehydration left little to no porosity remaining in the framework. This began to change when the research group of Omar Yaghi developed many of the contemporary synthetic techniques for MOFs, starting with alcohols and hydrothermal synthesis [37–40]. They used a room temperature synthesis in *N*,*N*-dimethylformamide (DMF) with slow diffusion of toluene to create a zinc terephthalate that came to be known as MOF-2 in 1998 [41]. MOF-2 was the first in a long line of high-surface area zinc dicarboxylate materials [42]. Although the synthesis of copper terephthalate was reported earlier [42],

MOF-2, a polymorph of zinc terephthalate, became the most studied system of the simple metal terephthalates [41, 43]. Additional studies to solve polymorphs to MOF-2 found that, in addition to the P21/*c* structure of MOF-2, there was another possible C2/*m* polymorph [44, 45].

By adopting polar aprotic solvents like DMF as reaction media, the higher boiling point and increased solubility of TPA decreased reaction times from weeks to hours and increased product quantities from micrograms to kilograms [46]. The additional benefit of such bulkier solvents was that they were bound more weakly, and their removal resulted in less damage to the framework. This had the effect of making possible structures that were air porous upon desolvation [41]. The technological advances, the dramatic increase in synthetic throughput, and the prospect of a material with a competitively high surface area led to a rapid growth in the number of syntheses and structural solutions of metal carboxylate frameworks [27, 47].

The MOF that we chose to study first was copper terephthalate. While ours was not the first synthesis of such a material, we developed a synthetic procedure that could create gram quantities in a matter of hours, in contrast to previous reports. Moreover, these syntheses can be carried out in air at ambient pressure and the resulting product retains its structure and properties for at least a year. The resulting product lacks the overlapping d_{z^2} orbitals and anisotropic conductivity of the rhodium diisocyanide polymer. But it has other useful properties, namely a high surface area.

We then set out to compare this copper terephthalate framework against terephthalate frameworks synthesized from adjacent elements in the periodic table: cobalt, nickel, zinc, and magnesium. Although magnesium is not strictly speaking adjacent to the transition metals on the Mendeleev periodic table, it serves as a comparison to zinc. Both Zn(II) and Mg(II) have closed electron shells and would thus be expected to react similarly in some ways with the carboxylate group of the terephthalate ligand. This comparison also serves to highlight why different metal terephthalate frameworks have different crystallization or thermal degradation behaviors.

1.3 Heterometallic organic frameworks

Last, we discuss the attempts to modify the crystallization of one metal terephthalate framework by adding another metal ion. Understandably, most of the MOF structures that have been reported incorporate a single metallic species. Reports of microporous heterometallic MOFs have appeared

in the literature since 2004, with a Co-Na TPA biphenyldicarboxylate acid [48]. The majority of the research in this field has been restricted to 3d-4f heterometallic frameworks owing to the variety of coordination geometry that the lanthanides and actinides possess [32]. Often the two species are offered different coordination environments with heterofunctional ligands, offering hard and soft bonding sites for different species [49]. Fewer systems have been studied where the two metals have similar character. One recent study looked at $[Zn_2(ox)_3]$ $[Cu(I)_2(4,4\text{-bipy})_2]$ (ox = oxalate, 4,4-bipy = 4,4–bipyridine), forming alternating 2D sheets and 1D chains [50]. Our interest in heterometallic systems came from a desire to modify an existing, well understood MOF system by the addition of a heterometallic center.

Our results demonstrate how the nucleation and growth of these crystalline frameworks can be controlled and directed by the presence of a second metal. Specifically, the entire compositional range of the zinc-copper terephthalate framework is presented and analyzed. The presence of a minority copper concentration in a majority zinc solution is found to alter crystallization of the framework, resulting in a higher surface area. Furthermore, the possibility of creating copper-zinc dimers in the framework is discussed. It is hoped that, should these specific metal organic frameworks ever be produced on a large scale, this finding will increase the efficiency of such an operation.

1.4 Future directions

In the course of this project, many leads were generated that could not be followed by the author. Some of these are left to others currently interested in this line of research. This thesis concludes with a summary of the new directions immediately visible being carried out by others. There are computational models of copper terephthalate being constructed to assist with molecular calculations. Others are calculating the permeability and gas separation constants of such a material. Others still are making membranes from the copper terephthalate and measuring the ability of copper terephthalate to separate gases effectively. Furthermore, copper terephthalate could be used as a surface coating on Zeolite particles to increase adhesion to a mixed membrane without decreasing the permeability. Even beyond these immediate leads, others remain unexplored. The properties of mixed transition metal organic frameworks remain, for the most part unexplored. Preliminary

findings hint at exciting new properties and possibilities.

CHAPTER II

EXPERIMENTAL DETAILS

2.1 Synthetic procedures

For the rhodium diisocyanide experiments, the chlorodicarbonylrhodium(I) dimer, $[Rh(CO)_2Cl]_2$, (Strem) and reagent grade CH_2Cl_2 (Sigma-Aldrich, 99.5%) were used without purification. Phenylene diisocyanide (Aldrich, 99%) was sublimed in vacuum to obtain white crystals. For the metal terephthalate experiments, all chemicals were used without further purification. Cobalt nitrate hexahydrate ($Co(NO_3)_2{\cdot}6H_2O$), nickel nitrate hexahydrate ($Ni(NO_3)_2{\cdot}6H_2O$), and magnesium nitrate hexahydrate ($Mg(NO_3)_2{\cdot}6H_2O$), and copper nitrate trihydrate ($Cu(NO_3)_2{\cdot}6H_2O$) were purchased from Alfa-Aesar. Zinc nitrate hexahydrate ($Zn(NO_3)_2{\cdot}6H_2O$) and terephthalic acid (TPA) were purchased from Fluka. *N*,*N*-dimethylformamide (98%) was purchased from Sigma-Aldrich.

2.1.1 Rhodium diisocyanobenzene experiments

The synthesis was carried out at room temperature in a three-necked, round bottom flask under nitrogen. $[Rh(CO)_2Cl]_2$ in the amount of 155 mg was dissolved in 26 ml CH_2Cl_2 and poured into the flask. Phenylene diisocyanide (pdi) in the amount of 202 mg, a twofold molar excess, was dissolved in 50 ml of the same solvent and added dropwise to the $[Rh(CO)_2Cl]_2$. After 45 min, a dark green precipitate was obtained which was then filtered, washed with CH_2Cl_2 (4 x 50 mL), and dried overnight under vacuum at 126 torr, 110°C.

2.1.2 Copper terephthalate experiments

To make Cu(TPA)·(DMF), equimolar quantities of copper nitrate trihydrate (241 mg) and TPA (166 mg) were dissolved in DMF (20 mL). This solution was placed in a closed 30 mL flask in an oven at 110 °C for 36 hrs. Small blue precipitated crystals were visible inside the flask upon removal from the oven. After repeated centrifugation and washing, samples were sent to Atlantic Microlab (Norcross, GA) for microanalysis. The analysis calculated for $C_{11}H_{11}NO_5Cu$: C 43.93, H 3.69, N 4.66, O 26.60; found: C 43.33, H 3.67, N 4.67, O 26.49. Upon drying at 225 °C, the analyses

for $C_8H_4O_4Cu$ were as follows: calculated: C 42.21, H 1.77, N 0.00, O 28.11; found: C 40.83, H 1.81, N 0.16, O 27.81. The remaining portion should have been Cu, but the microanalyses indicated a small amount of impurities in the original specimen (calcd Cu 21.13, found 21.85), and a much larger impurity content in the specimen desolvated at 225 °C (calcd 27.91, found 29.41).

2.1.3 Copper - Zinc Terephthalates

Copper nitrate ($Cu(NO_3)_2 \cdot 2.5H_2O$), zinc nitrate ($Zn(NO_3)_2 \cdot 6H_2O$), and TPA ($C_8H_6O_4$) were each dissolved in 43.7 mL DMF at 0.1 M concentrations. Then the salt solutions were mixed in Erlenmeyer flasks at 0, 1, 10, 30, 50, 70, 85, 95, and 100% Cu concentrations. To this was added an equimolar amount of the TPA solution. These were then covered with foil and placed in an oven at 100 °C for 22 hours. Upon removal, the precipitate was filtered and then washed repeatedly in DMF.

2.1.4 Metal terephthalates

The metal nitrate salts were dissolved in 10 mL of DMF at 1mM concentrations in scintillation flasks. To this was added 10 mL of 1mM TPA solution in DMF. These were then capped off and placed in an oven heated to 100°C for 24 hours. The solutions were then removed from the oven and washed repeatedly with DMF.

2.2 Characterization techniques

2.2.1 Electrical measurements

Electrical measurements were carried out only for the rhodium diisocyanide compounds. The resulting powder was ball-milled for 7 hours, pressed into pellets under uniaxial pressure of 5 tons for 20 minutes and sputter-coated with platinum. The thickness of the pellets was measured by a micrometer and the area was measured by analysis of digital photographs. This was necessary because the pellets were extremely brittle and had uneven shapes. Samples were placed in a specially designed test fixture and lowered into a Schlenk bottle for testing. To control the temperature and humidity, the schlenk bottle contained a small amount of desiccant at the bottom and was wrapped with flexible electric heating tape. A picture is shown in Figure 2.1 The temperature inside the schlenk tube was controlled by an Omega CN9122A PID controller. Temperature readings were

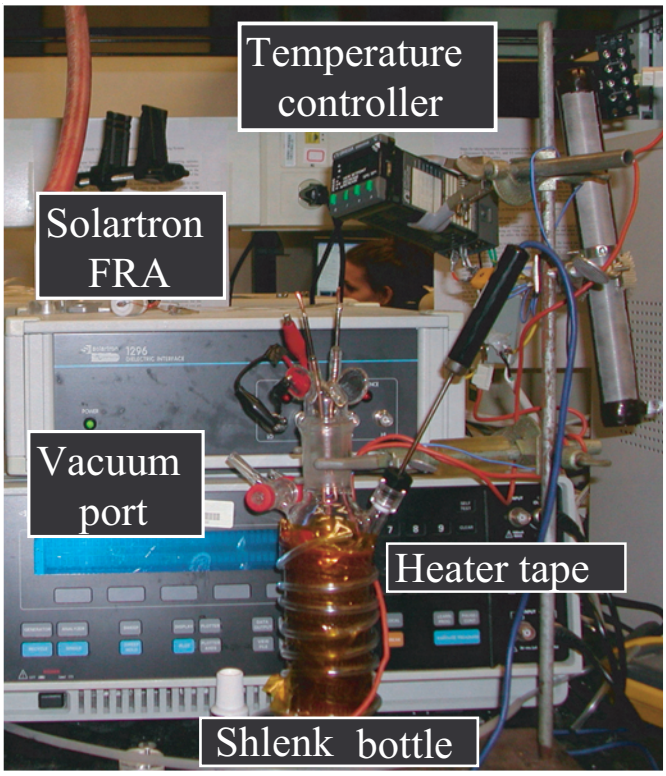

Figure 2.1: A photograph showing the Schlenk bottle and the temperature controller used to control the test environment. Also visible is the Solartron Frequency Response Analyzer used to carry out the electrical measurements. The copper wires extending out the top of the Shlenk bottle were the feed-throughs that connected the FRA to the specimen in the test fixture.

taken from a thermocouple inside the flask. Samples were stored under lab air at 21°C from the time of synthesis until being tested. At the time of measurement, all samples had been heated to 100°C under a vacuum of 5 in Hg.

Electrical experiments were conducted using a Solartron (Farnborough, Hampshire, England) SI 1260 Impedance Analyzer and a 1296 Dielectric Interface in the frequency range of 10 mHz to 10 MHz with 0.1 V r.m.s. Multiple impedance spectra were collected at each temperature to ensure representative behavior. Complex impedance plots were used to estimate the DC conductivity (with geometric considerations, see Chapter 3).

2.2.2 Infrared spectroscopy

A Nicolet (now ThermoFisher, Waltham, MA) Nexus 870 Infrared Spectrometer was used for all specimens. Each graph was obtained using over 500 scans with 2 cm^{-1} resolution. For the poly-$[Rh(pdi)^{+}_{4/2}(Cl)^{-}]_n$ spectra, scans were collected from NaCl pellets into which had been ground a small amount of the specimen. For the other scans, an Attenuated Total Reflectance (ATR) accessory was used to collect the data. All the metal terephthalate scans were corrected for the ATR and for ambient moisture.

2.2.3 X-ray powder diffraction

During the course of these experiments, four different X-ray diffractometers were used. Table 2.1 compares the different instruments used during the course of the thesis. All the diffractometers were configured in the Bragg-Brentano geometry. The initial work with rhodium diisocyanide was conducted on a Phillips 1800PW powder diffractometer (Philips Analytical Inc., Natick, MA) operated at 30 kV with Cu Kα radiation. This device had no adjustable optics and ceased functioning shortly after the completion of these experiments. For the work with copper terephthalate, powder diffraction scans were taken with a Rigaku Mini-Flex (Tokyo, Japan) with Cu K_α operating at 0.6 kV. After these experiments, this machine stopped working as well. High temperature powder diffraction scans were taken with a Panalytical X'Pert Pro MPD (Almelo, The Netherlands) at the Oak Ridge National Lab with Cu K_α radiation at 45 kV. The Anton-Parr HTK 1200 oven furnace was used to control the temperature under a He atmosphere. Information about the optics used was not recorded.

For subsequent experiments, including work with the Cu-Zn terephthalate system and other metal terephthalates, diffraction profiles were measured using an Alpha-1 Panalytical Diffractometer (Almelo, The Netherlands) at 45 kV and 40 mA. A symmetrical incident beam Johansson monochromator was used to ensure that only the $K_\alpha 1$ component of Cu radiation was used. Data acquisition was carried out with a solid-state position sensitive ultrafast detector (X'Celerator, Panalytical, Almelo, The Netherlands). As for the optics used, a 20 mm mask was inserted to adjust the size of the probing X-ray spot to the Si 510 zero-background sample holder. The incident beam path used a divergence slit of 1/4° and Soller slits of 0.02 rad to reduce instrumental effects. The

Table 2.1: A table displaying the different X-ray diffractometers used throughout the experiments.

Material	Diffractometer	Radiation	Sample Holder
Rh(PDI)	Phillips 1800PW	Cu K_α	Powder pellet
Cu(TPA)	Rigaku Mini-Flex	Cu K_α	Powder pellet
Cu(TPA) (HT)	MPD	Cu K_α	Powder pellet
Cu-Zn(TPA)	Alpha-1	Cu $K_\alpha 1$	Si 510
Mg(TPA)	Alpha-1	Cu $K_\alpha 1$	Si 510
Mg(TPA) (HT)	MPD	Mo K_α	Si 510
Co(TPA)	Alpha-1	Cu $K_\alpha 1$	Si 510
Zn(TPA)	Alpha-1	Cu $K_\alpha 1$	Si 510
Ni(TPA) (HT)	MPD	Cu K_α	Powder pellet

diffracted beam also carried the 0.02 rad. Soller slits as well as a 5.0 mm anti-scattering slit. Si-640B powder was used as an internal standard to correct the scans for sample displacement errors. X'Pert Highscore Plus by Panalytical (Almelo, The Netherlands) was used to refine the single crystal parameters to the measured powder diffraction profile. Jade from Materials Data (Livermore, CA) was also used to analyze powder diffraction data and match that to previously reported structures.

2.2.4 Single crystal analysis for Cu(TPA)·DMF

These measurements and analyses were carried out at the Crystallography lab at Emory University. The crystal structure of blue block-shaped crystals of Cu(TPA)·(DMF) were analyzed at 173 K: monoclinic, space group C2/*m* with a = 11.4143 (3) Å, b = 14.2687 (4) Å, c = 7.7800 (2) Å, β = 108.119 (1)°, V = 1204.27 (6)Å^3, Z = 4, d_{calc} = 1.637 g·cm^{-3} and mu_a (Mo K_α) = 1.824 mm^{-1}. Data collection was carried out at 173 K on a Bruker (Billerica, MA) D8 SMART APEX CCD sealed tube diffractometer using Mo K_α radiation with a graphite monochromator and ω scans out to 25.96°, giving 1159 unique reflections. The structure was solved by direct methods (SHELXTL, V6.12) and refined to a standard discrepancy index of R = 0.0348 and R_w = 0.0818 for 1046 reflections with $F > 2\sigma(F)$ and a goodness of fit on F^2 = 1.093. Anisotropic thermal parameters were refined for all non-hydrogen atoms; hydrogens were refined isotropically as riding atoms. Some of the hydrogens could not be resolved, and thus were not included in the analysis.

2.2.5 Thermogravimetric analysis

The thermogravimetric analyses were carried out on a TA Instruments (New Castle, DE) Q50 thermogravimetric analyzer from room temperature up to 500 °C at a heating rate of 5 °C/min under nitrogen and oxygen. This data was analyzed using Universal Analysis 2000 from TA Instruments. For the Cu-Zn terephthalate work, the different mass loss events were compared by fitting peaks under the curves of the derivative of mass loss with temperature in Jade. PowDLL Converter [51] was used to convert two column data from Universal Analysis into the .xrdml files, which can be opened by Jade.

2.2.6 X-ray photoelectron spectroscopy

X-ray photoelectron spectroscopy was conducted on a Surface Science Instruments (Sunnyvale, CA) SSX-100 small spot ESCA spectrometer with Al K General Survey. The pass energy was 150 eV with a take-off angle of 55° from the normal. All samples were charge compensated by indexing the aromatic C(1s) line at 284.8 eV [52]. All scans were analyzed using ESCA 2000 A Analysis Software from Service Physics.

2.2.7 Surface area analysis

Surface area measurements for the Cu(TPA) and Zn-Cu(TPA) samples were obtained with a Micromeritics (Norcross, GA) ASAP 2020. All samples were degassed at 220 °C for one day prior to measurement. A preliminary freespace measurement was taken on each sample before a secondary outgassing at 220 °C for 4 hours. This ensured accurate results by making the analyzing gas the first gas to contact the evacuated sample after outgassing. Surface area measurements were also taken for the other metal terephthalates, Mg, Co and Ni(TPA). These were measured on a Micromeritics Gemini V surface area and pore size analyzer. These samples were degassed at 300 and 200 °C for 3 hours for Mg and Co(TPA), respectively. Cu, Co, and Ni(TPA) were also measured on a Beckmann-Coulter (Fullerton, CA) SA-3100, however these the results obtained with this machine were consistently lower than what was obtained with both Micromeritics machines, so they are assumed to underestimate the true surface area.

2.2.8 Magnetic susceptibility measurements

For the magnetic susceptibility measurements, a Quantum Design (San Diego, CA) SQUID MPMS magnetometer at Florida State University was used with a background magnetic field of 100 Oe and a sample size of approximately 1 gram. For most of the cases, only the zero field cooled case is shown, as there was only a minimal difference between the field cooled and zero field cooled case.

2.2.9 Electron paramagnetic resonance

Room temperature X-band electron paramagnetic resonance measurements were carried out with a X-band Bruker (Billerica, MA) EMX Spectrometer equipped with a Bruker HS4119 high-sensitivity cavity at a power of 0.633 mW and modulation frequency of 100 kHz.

CHAPTER III

EFFECTS OF AMBIENT ENVIRONMENT ON METAL-DIISOCYANIDE FRAMEWORKS

3.1 Introduction

The goal of this chapter is to study the effect of structure and chemical stability on the electrical properties of coordination polymers. To our knowledge, this is the first full report to apply impedance spectroscopy over a large frequency range to insoluble coordination polymers. These measurements allow us to extrapolate DC conductivity of poly-$[Rh(pdi)^{+}_{4/2}(Cl)^{-}]_n$ as well as the AC dielectric properties. This work also attempts to characterize the chemical stability of poly-$[Rh(pdi)^{+}_{4/2}(Cl)^{-}]_n$ upon exposure to air using X-ray diffractometry (XRD), thermo-gravimetric analysis (TGA), and X-ray photoelectron spectroscopy (XPS). An earlier report focused on the effect of moisture in poly-$[Rh(pdi)^{+}_{4/2}(Cl)^{-}]_n$. Using this technique, we were able to show a tendency for poly-$[Rh(pdi)^{+}_{4/2}(Cl)^{-}]_n$ to become more conducting in a dry environment [53].

3.1.1 Electrical characterization

Although this is not the first report of the electrical properties of poly-$[Rh(pdi)^{+}_{4/2}(Cl)^{-}]$ [17], new methods and instrumentation are now available to clarify the physical basis for the electrical semiconductivity of this class of materials and examine their chemical stability. Because this chapter deals extensively with electrical characterization, a brief introduction is provided.

The analysis of electrical properties under AC current, or impedance spectroscopy, reveals the collective response of microscopic polarization processes under an applied external AC electric field [54]. Under an AC field, frequency dispersion can be observed by measuring the electrical impedance and susceptibility of a given material owing to the different polarization and relaxation mechanisms present [55]. The complex impedance $Z^*(\omega)$ and the complex permittivity $\varepsilon^*(\omega)$ are obtained as a function of frequency as follows: [56]

$$\varepsilon^* = \varepsilon' - i\varepsilon'', Z^* = Z' - iZ'' = \frac{1}{i\omega\varepsilon^* C_0} \tag{3.1}$$

where $i = \sqrt{-1}$ and ω is the frequency in radians. The real parts are denoted by a single prime (ε' and Z') and the imaginary parts by a double prime (ε'' and Z''). The geometric capacitance C_0 is used to calculate the dielectric constant κ and the conductivity σ of the sample. For a thin disk of area A and thickness t the geometric capacitance is obtained as $C_0 = \varepsilon_0 A/t$, where ε_0 is the permittivity of free space. The dielectric constant is then $\kappa = \varepsilon'/C_0$ and the conductivity is $\sigma = \varepsilon_0/(C_0 Z')$.

When modeled as a single resistance in parallel with a capacitance, the impedance takes the form of a semi-circle [57]. If the measurements are taken down to a sufficiently low frequency, then the DC resistance can be estimated from the intercept of the semi-circle with the real axis. The DC conductivity can be written as:

$$\sigma_{DC} = \lim_{\omega \to 0} \frac{\varepsilon_0}{C_0 Z'} \tag{3.2}$$

This method is preferred when the impedance is sufficiently high that it cannot easily be measured with DC methods. The use of impedance spectroscopy in coordination polymers has been limited to thin films of metal substituted organic complexes [58, 59] and polymers with incorporated organometallic fragments [59]. Reports of the use of impedance spectroscopy to characterize pressed bulk powders of coordination polymers are virtually nonexistent in the literature. Crayston et al. published a study concerning the pressed powder conductivity of poly-[$RuCl_2$(pdi)$_{3/2}$(dimethyl sulfoxide)], a compound very similar to poly-[Rh(pdi)$^+_{4/2}$(Cl)$^-$]$_n$ [60]. Using the four-probe method, they measured a conductivity of $2 \cdot 10^{-12}$ S·cm^{-1} for the Ru-based polymer. Another study investigated the conductivity of thick films of poly-chelate poly-[M(4,4-bis[(N-butane salicylaldehyde-diamine diamine-5)azo]biphenyl)], where M = Mn(II), Fe(II), Ni(II), Zn(II), Cd(II), measuring conductivities with an electrometer between 10^{-8} and 10^{-11} S·cm^{-1} [61].

3.2 Results

3.2.1 Vibrational and structural characterization

Poly-$[Rh(pdi)^{+}_{4/2}(Cl)^{-}]_n$ was prepared from the reaction of chlorodicarbonylrhodium(I) dimer with two-fold molar excess of pdi under mild experimental conditions [23]. This reaction is shown in Equation 3.3

$$(n/2)[Rh(CO)_2Cl]_2 + 2(pdi) \xrightarrow[\text{Air, } 20^\circ]{CH_2Cl_2} [Rh(pdi)^{+}_{4/2}(Cl)^{-}]_n + 2n(CO) \tag{3.3}$$

Figure 3.1 shows the X-ray powder diffraction patterns as well as the FT-IR peak used to confirm the presence of poly-$[Rh(pdi)^{+}_{4/2}(Cl)^{-}]_n$. The IR peak shown corresponds well to the isocyanide stretching frequency, ν(CN), of 2140 cm^{-1} previously reported for poly-$[Rh(pdi)^{+}_{4/2}(Cl)^{-}]_n$ [62]. Based on the X-ray diffraction peaks, the structure is presumed to be tetragonal, with a = 10.6 Åand c = 3.3 Å. The X-ray trace shows the (100) peak at 2θ = 8.3°, corresponding to a, the approximate length of a single pdi ligand molecule. This assignment is supported by the peaks at 10.1 and 5.4 °2θ, which are assigned to the (110) and (200) peaks. The peak at 2θ = 26° is assigned to the (001) plane and attributed to the close proximity of 3.3 Å between Rh(I) ions in adjacent ligand sheets [22]. Taking both peaks together, the X-ray diffraction pattern indicates that the polymer exists as layered sheet-like lamella, with interplanar spacings of 3.3 Å. Figure 3.1 also shows that thorough washing was found to play an important role in allowing the (001) X-ray peaks to be detected. On the basis of matching chemical and structural data, we conclude that the synthesized structure is similar to the one depicted in Figure 3.2.

3.2.2 Electrical properties

Electrical measurements were conducted to determine the electrical activation energy for conduction and possible contribution of Rh-Rh bonds to the conductivity. Figure 3.3 shows the initial real and imaginary conductivities as a function of frequency for a range of temperatures. In keeping with Equation 3.1, the DC conductivities are estimated by taking the reciprocals of the low frequency intercepts of the complex impedance curves, shown in Figure 3.4 (with geometry accounted for) or from the frequency independent flat region in Figure 3.3.

However, the powder began to change color over time, going from a deep green to a dark

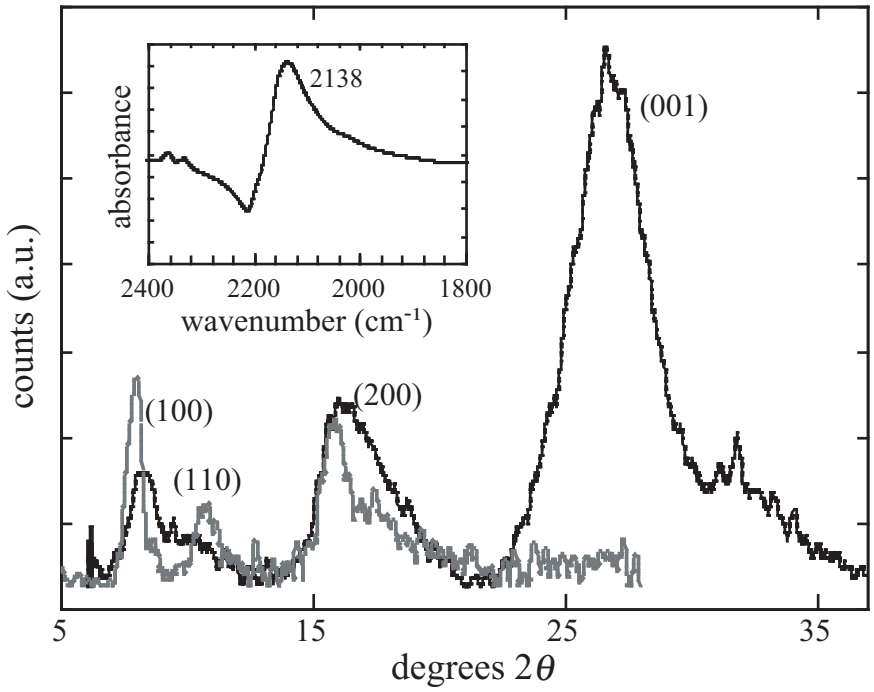

Figure 3.1: X-ray diffraction patterns of poly-$[Rh(pdi)^{+}_{4/2}(Cl)^{-}]_n$. The (100) peak corresponds to a *d*–spacing of 10.6 Å, the length of the pdi ligand. The (001) peak corresponds to the Rh-Rh distance of 3.3 Å. The gray line shows an X-ray diffraction pattern for unwashed poly-$[Rh(pdi)^{+}_{4/2}(Cl)^{-}]_n$, with no (001) peak present. The inset shows the ν(CN) absorbance peak of the poly-$[Rh(pdi)^{+}_{4/2}(Cl)^{-}]_n$ taken after drying [26].

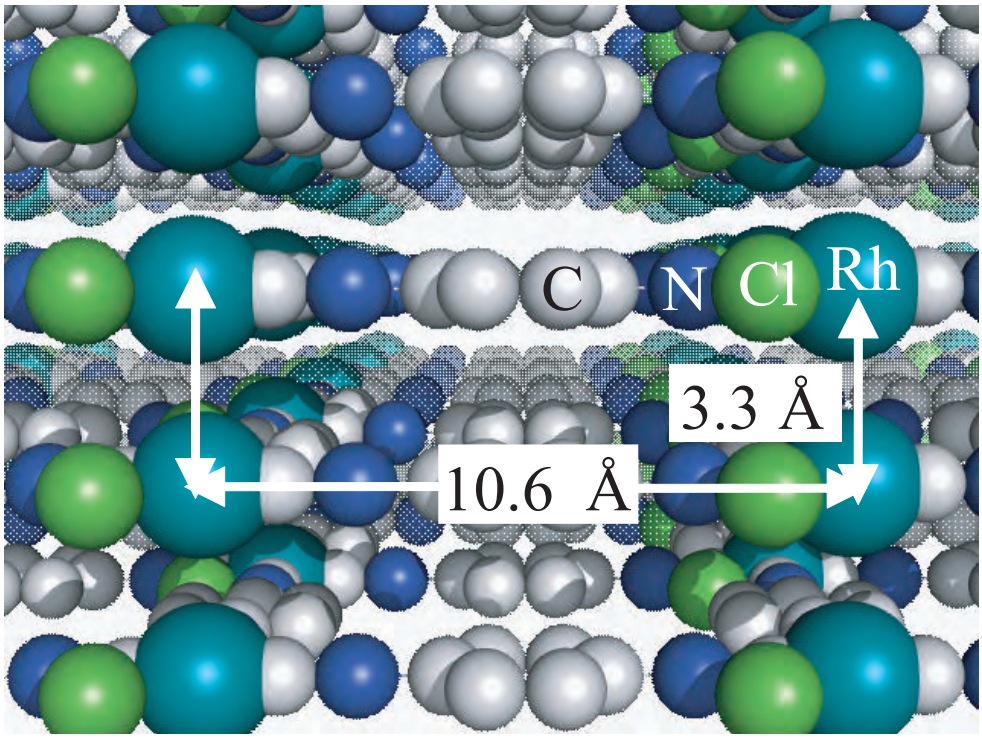

Figure 3.2: A representation of poly-$[Rh(pdi)^{+}_{4/2}(Cl)^{-}]_n$ as viewed perpendicular to the [001]direction. The H atoms are omitted for clarity. The close proximity of the Rh atoms creates a conducting pathway in the [001]direction [26].

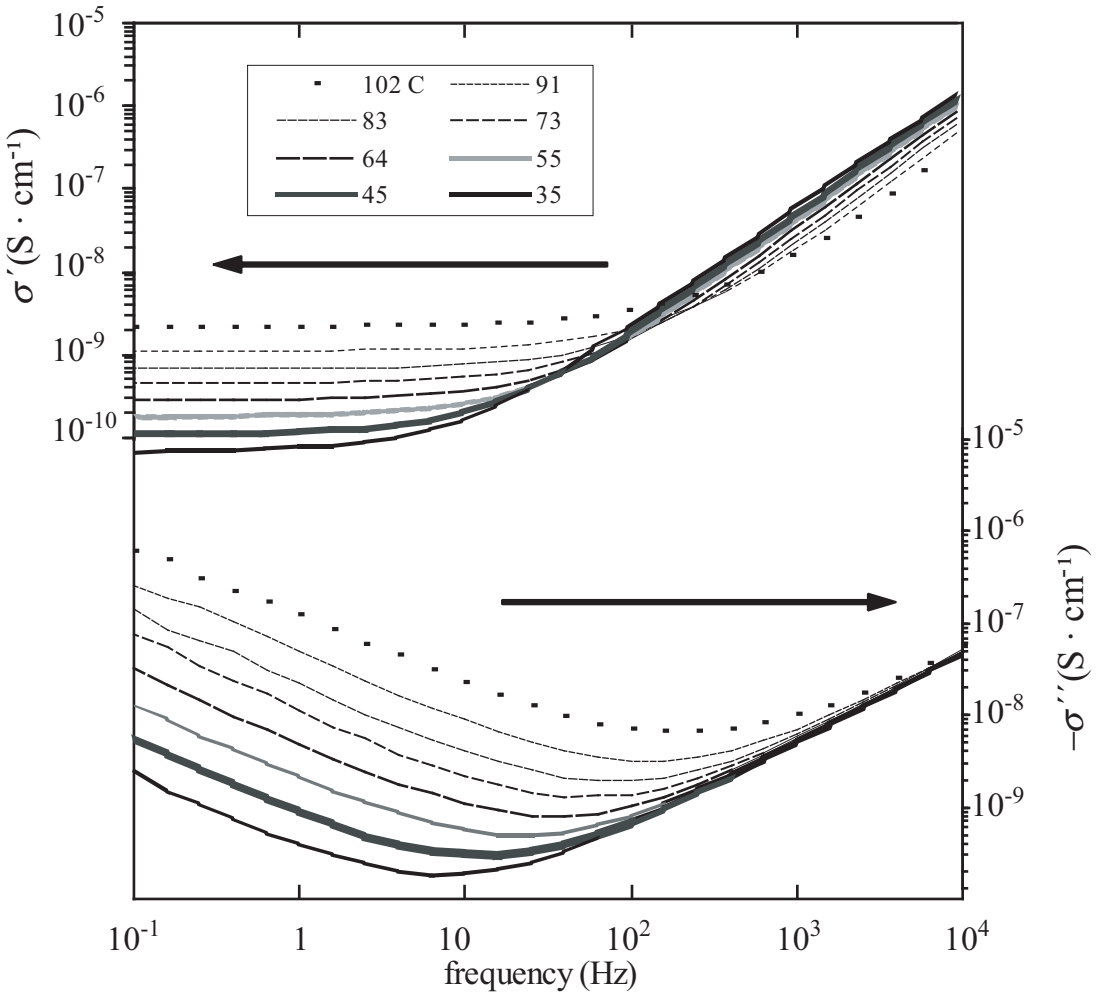

Figure 3.3: The real and imaginary conductivity of poly-$[Rh(pdi)^{+}_{4/2}(Cl)^{-}]_n$, σ' and σ'', respectively, are plotted as a function of log frequency for eight different temperatures [26].

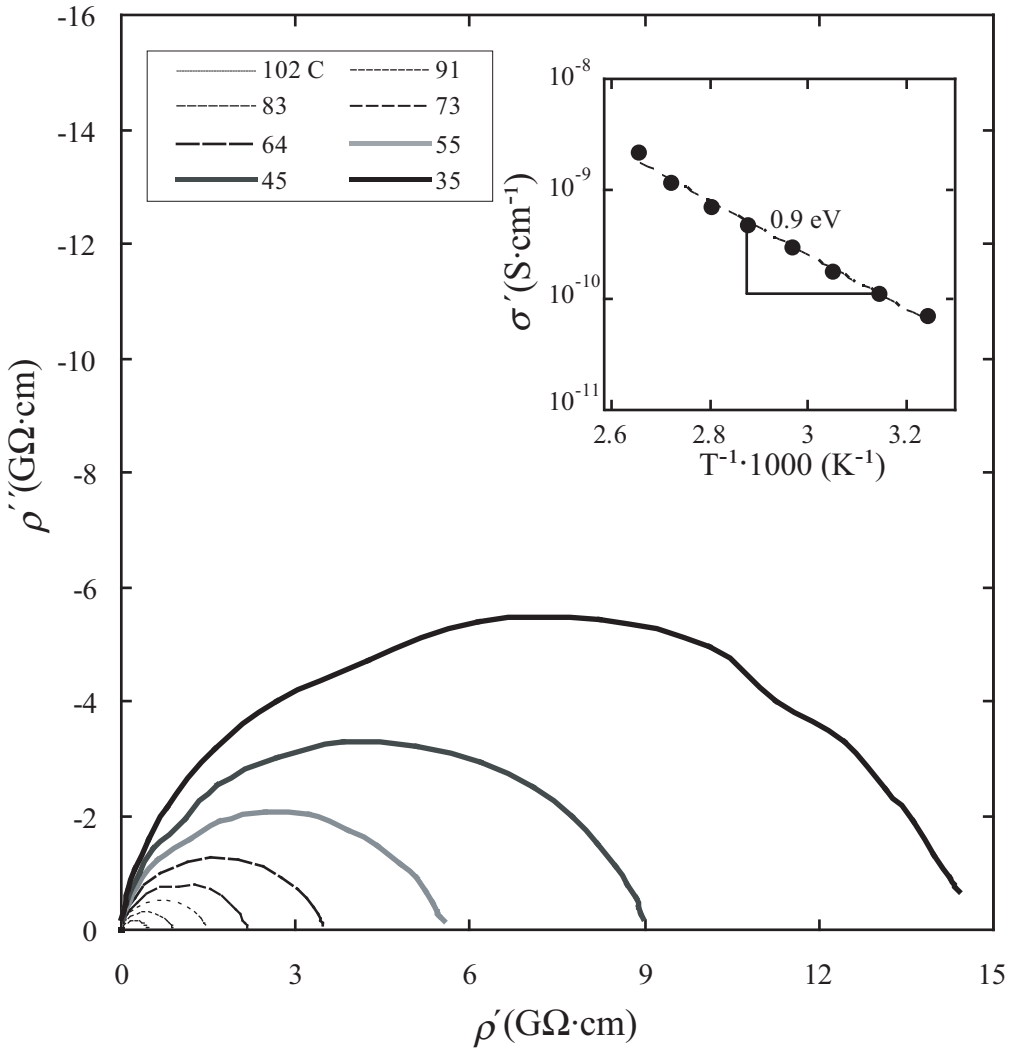

Figure 3.4: The complex resistivity curves of poly-$[Rh(pdi)^{+}_{4/2}(Cl)^{-}]_n$ for a range of temperatures from 101–35 °C are shown. The low frequency intercepts on the real axis indicate the estimated DC resistivity, from which the DC conductivity is calculated. The inset shows the conductivity plotted against T^{-1}, indicating the slope from which the electrical activation energy is calculated [26].

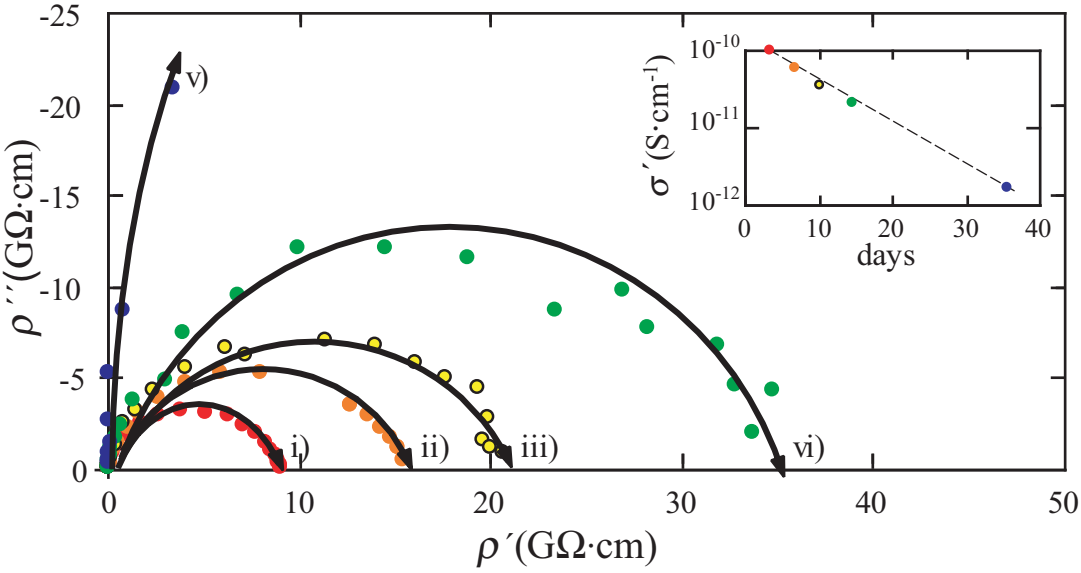

Figure 3.5: In (a), the complex impedance plots of poly-$[Rh(pdi)^{+}_{4/2}(Cl)^{-}]_n$ for 3, 7, 10, 14, and 36 days after synthesis are shown in (i), (ii), (iii), (iv), and (v), respectively. All measurements were taken at 45 °C in an evacuated Schlenk tube. The inset shows the conductivities calculated from the low frequency intercepts of these curves, indicating that the material becomes less conductive with time. The dashed line indicates an exponential fit with a time constant of 8 days [26].

brown. As the conductivity of more specimens were tested, it became apparent that the measured conductivity decreased as the specimens aged. After 36 days, the estimated DC conductivity was less than 1% of its estimated initial value. In order to examine the effect of the decrease in the bulk conductivity, the conductivities of the specimens collected at 45 °C were graphed as a function of time (i.e. measurement time after synthesis). Figure 3.5, along with the corresponding normalized impedance spectra, shows the conductivity decreasing over time.

Figure 3.7 shows the dielectric constant with an estimated initial value of 7.5 at room temperature and decreasing by 15% over 36 days. Data are reported at a frequency of 10 kHz because the dielectric constant is independent of frequency in this range, but sensitive to dispersion at lower frequencies.

3.2.3 Structural characterization

The changes in color from specimen to specimen were indicative of a structural change taking place in the polymer. Therefore, over a period of one and a half months, X-ray diffraction patterns were collected to monitor this change. Figure 3.8 shows a series of X-ray scans of poly-$[Rh(pdi)^{+}_{4/2}(Cl)^{-}]_n$

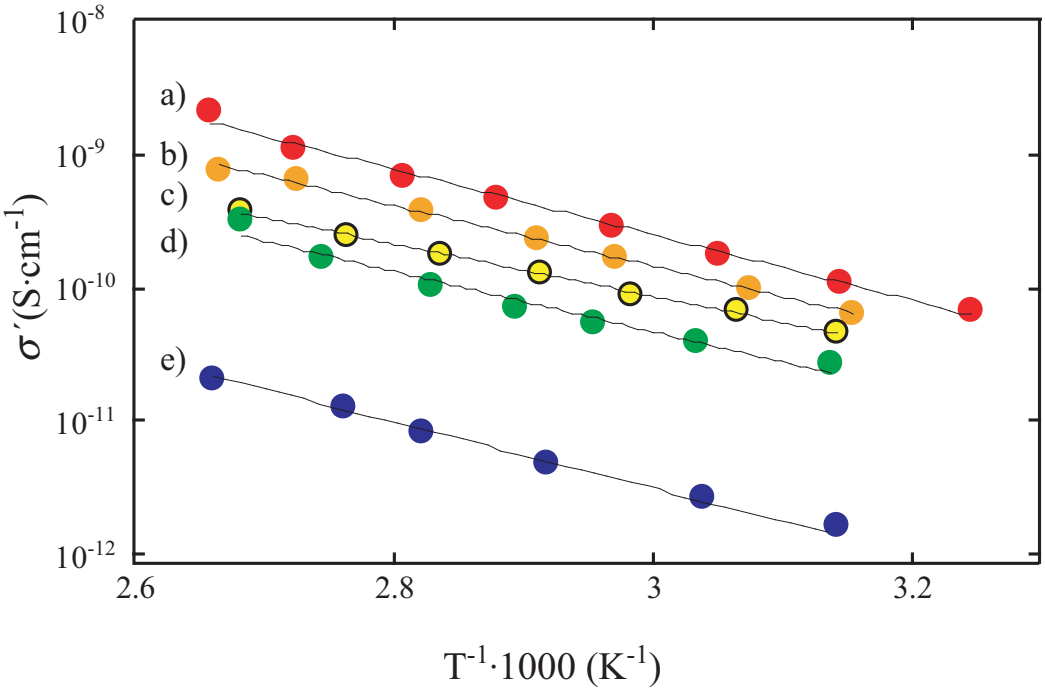

Figure 3.6: Plots indicating the electrical activation energy of poly-$[Rh(pdi)^{+}_{4/2}(Cl)^{-}]_n$ for 3, 7, 10, 14, and 36 days after synthesis are shown in a, b, c, d, and e, respectively. While the fitted activation energy remains relatively constant at 0.9 eV, the magnitude of the conductivity drops with increasing time in air [26].

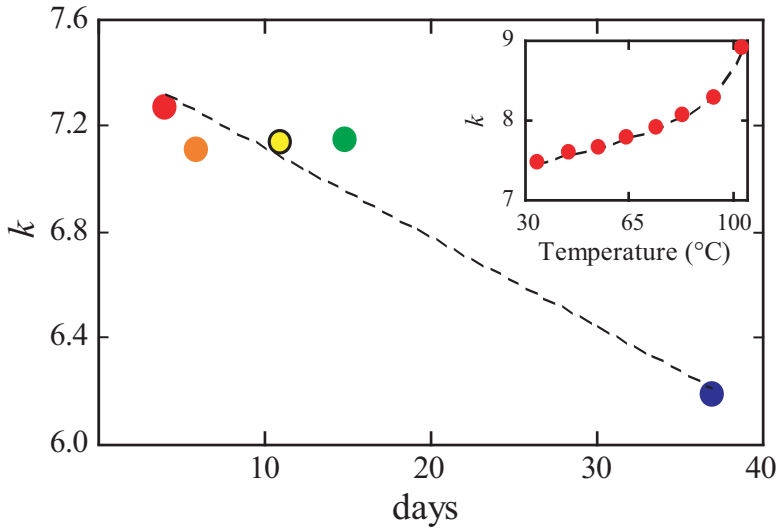

Figure 3.7: The frequency dependent dielectric constant at 10 kHz of poly-$[Rh(pdi)^{+}_{4/2}(Cl)^{-}]_n$ at 45 °C. The dielectric constant is shown to decrease over 36 days. The inset shows the temperature dependence of the dielectric constant at 10 kHz taken 3 days after synthesis. Symbols match the curves in (a) - (e) in Figure 3.6 [26].

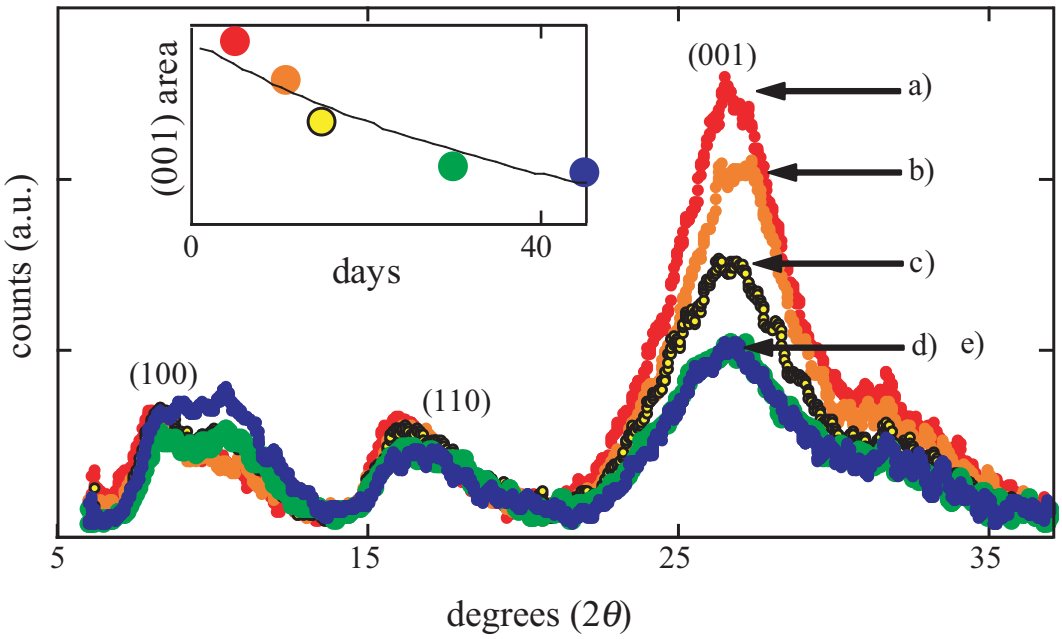

Figure 3.8: X-ray diffraction scans of poly-$[Rh(pdi)^{+}_{4/2}(Cl)^{-}]_n$ for 5, 11, 15, 31, and 45 days are shown in a, b, c, d, and e, respectively. The change of the (001) peak height with days from synthesis is shown in the inset. Note that the (100) and (110) peaks do not change appreciably over time [26].

over a period of 45 days. The specimens were left exposed to open atmosphere from the time of synthesis until analysis. These scans show the evolution of the crystal structure in the polymer over that time. Although the peak height of the (100) and (110) peaks remains constant, the (001) peak decreases in intensity over the course of a month to half its original value.

3.2.4 Thermal properties

Thermo-gravimetric analysis (TGA) is one way to probe the strength of these bonds and their chemical sensitivity. However, we also wanted to investigate the effect of atmosphere on thermal degradation. Figure 3.9 shows a comparison between two TGA curves taken under oxygen and nitrogen.

3.2.5 X-ray photoelectron spectroscopy

In metal-isocyanide systems, XPS has been used to characterize the presence of non-isocyanide chemical species present in the system. Accordingly, XPS measurements were performed to see if there were any shifts in the binding energies of the N 1s and C 1s electrons that would indicate a particular degradation process. Figures 3.10 and 3.11 show high-resolution XPS scans of the N 1s

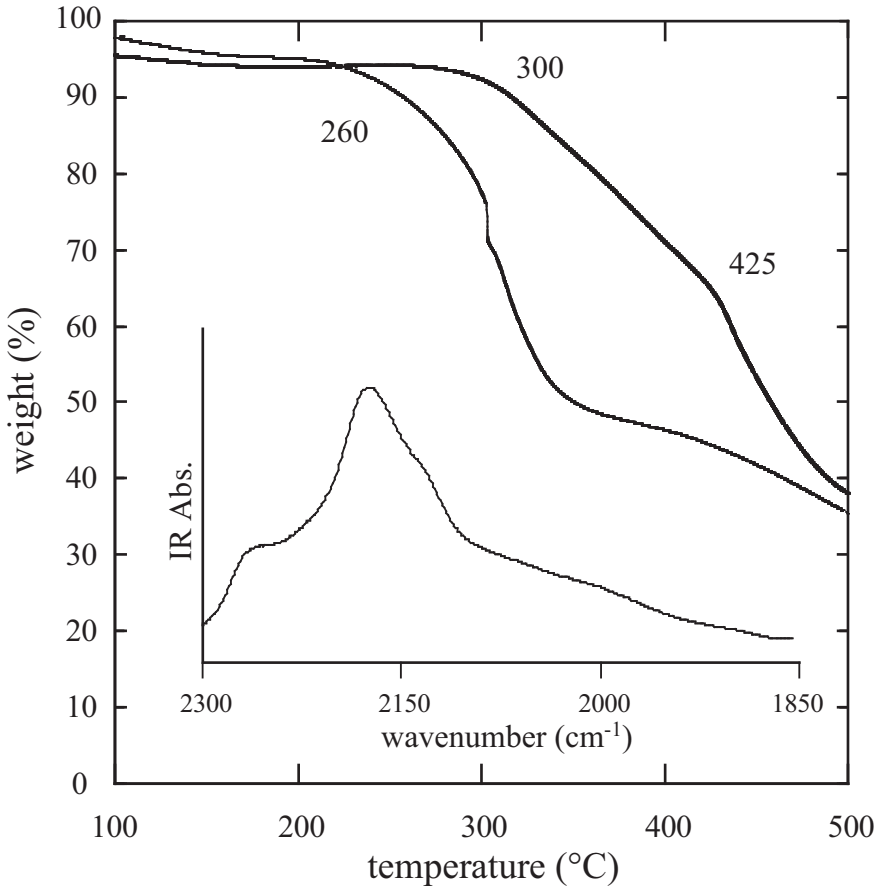

Figure 3.9: TGA of poly-$[Rh(pdi)^{+}_{4/2}(Cl)^{-}]_n$ under both nitrogen (–) and oxygen (-). Note the existence of two decomposition temperatures, at 300 and 425 °C under N_2. Under O_2, the decomposition starts at 260 °C. This coincides with the boiling point of 1,4-diisocyanatobenzene. The FTIR spectrum of poly-$[Rh(pdi)^{+}_{4/2}(Cl)^{-}]_n$ after being heated to 260 °C under oxygen is shown in the inset. The shoulder at 2267 cm^{-1} is indicative of the ν(CN) of an isocyanate [26].

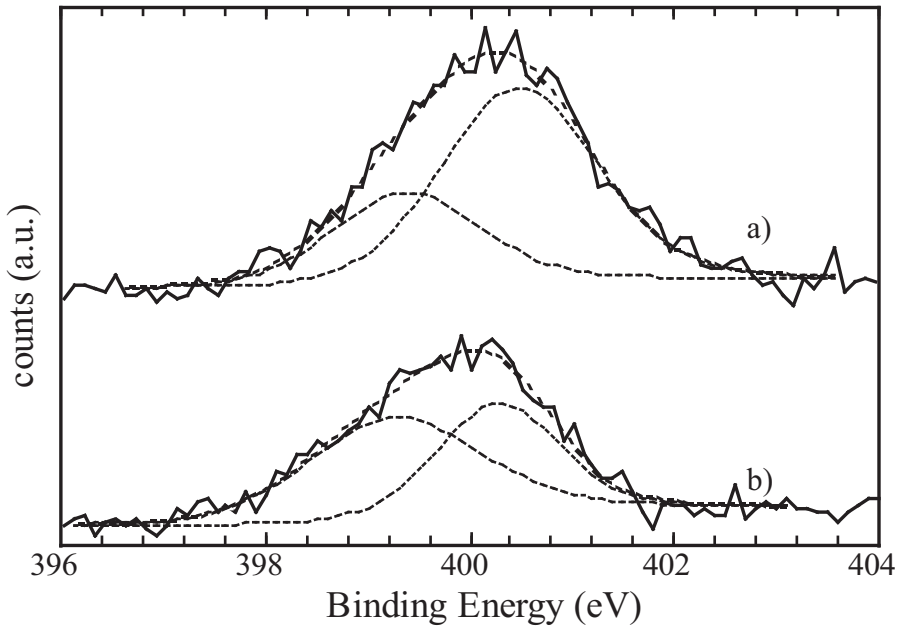

Figure 3.10: High resolution XPS of the N 1s region of poly-$[Rh(pdi)^{+}_{4/2}(Cl)^{-}]_n$. In (a), a pressed pellet has been stored under Ar, with little exposure to air for one week. In (b), another pressed pellet has been stored under lab air for the same amount of time [26].

and C 1s peaks of two samples held for one week under argon and lab air, respectively. This was done to differentiate between any non-oxidative degradation and oxidative degradation.

3.3 Discussion

The long-term oxidative stability of isocyanide-metal junctions has been the subject of recent research [4, 63–67]. Impurities have been shown to arise in different isocyanides for self-assembled monolayers on gold [4, 63, 64], nickel [65], copper [66], as well as cobalt-diisocyanobenzene multilayer thin films [67]. Although no such degradation studies have been carried out on Rh surfaces, diisocyanides have been shown to bond to Rh linearly through a single isocyanide group, similar to the bonding on Au(111) [68–70]. Rhodium has also been shown to be catalyze the oxidation of poly-isocyanides, possibly making the isocyanide sensitive to attack from oxygen or atmospheric ozone. [4, 71–74]. This would imply that there are at least two routes to oxidative degradation available to poly-$[Rh(pdi)^{+}_{4/2}(Cl)^{-}]_n$: conversion from isocyanide to isocyanate and polymerization to form poly-isocyanides.

Figure 3.5 showed the decrease in conductivity with time. This decrease can be modeled as an exponential decay with time t from synthesis, $\sigma_0 \exp(-t/\tau)$, with $\tau = 8$ days and $\sigma_0 = 1.4\times10^{-10}\pm0.5$

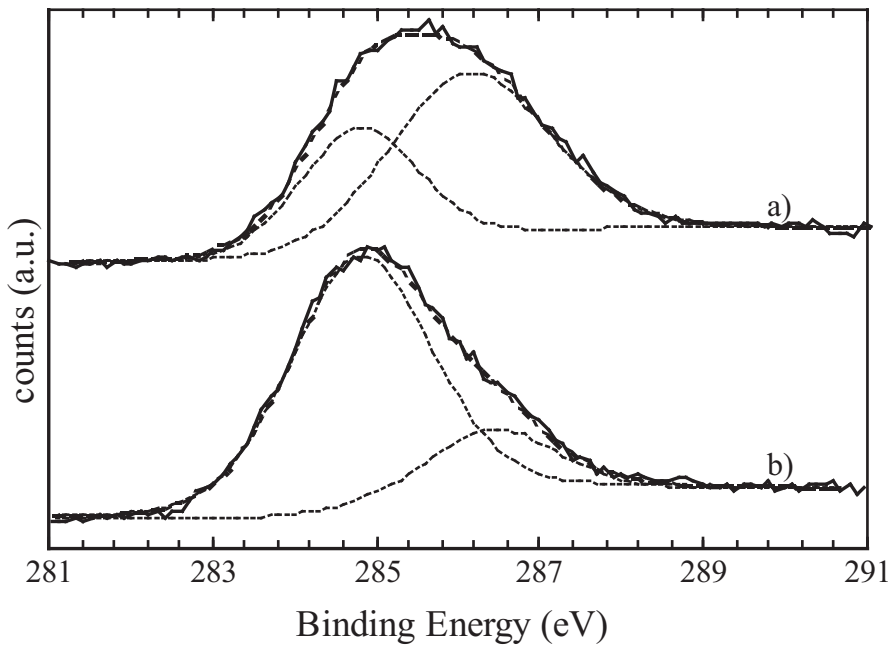

Figure 3.11: High resolution XPS of the C 1s region of poly-$[Rh(pdi)^{+}_{4/2}(Cl)^{-}]_n$. In (a), a pressed pellet has been stored under Ar, with little exposure to air for one week. In (b), another pressed pellet has been stored under lab air for the same amount of time [26].

$S{\cdot}cm^{-1}$ at 45°C. By treating poly-$[Rh(pdi)^{+}_{4/2}(Cl)^{-}]_n$ as a semiconductor in the intrinsic region, the activation energy can be calculated according to Equation 3.4:

$$\sigma_{DC} = \sigma_0 \exp\left(\frac{-E_a}{kT}\right) \tag{3.4}$$

In this equation, E_a is the activation energy, T is the temperature in Kelvin, and k is the Boltzmann constant and σ_0 is the pre-exponential constant. Our calculation of the electrical activation energy comes from the slope of the $\ln(\sigma_{DC})$ vs $1/T$ curves shown in the inset of Figure 3.4. These curves indicate that the electrical activation energy of poly-$[Rh(pdi)^{+}_{4/2}(Cl)^{-}]_n$ is 0.9 eV. The time-dependent behavior displayed in Figure 3.5 was not temperature specific, but occurred throughout the range of temperatures measured. Figure 3.6 shows the activation energy plots for specimens from 3 to 36 days after synthesis hovering around 0.9 eV. This would appear to indicate that the basic conduction mechanism remains the same; as a change in electrical activation energy would be evidence of a different mechanism.

By using the electrical activation energy, the room temperature σ can be estimated to be 3.4 ×

10^{-11} S·cm^{-1}. This conductivity is much lower than the value of 4.4×10^{-4}S·cm^{-1} previously reported at 1 kHz for this material [17]. However, it is much closer to the reported conductivity of 2×10^{-12} S·cm^{-1} reported for poly-[$RuCl_2(pdi)_{3/2}$(dmso)] by Crayston et al [60, 75].

While not as drastic, the dielectric constant of poly-$[Rh(pdi)^{+}_{4/2}(Cl)^{-}]_n$ was also found to decrease as a function of time with exposure to air. To our knowledge, the dielectric properties of these polymers have never been reported. As a dielectric material, the polymer can be modeled as a collection of one-dimensionally conducting regions where the charge carriers (electrons) have very high mobility [76]. Lattice translations or crystal defects could effectively reduce the length of these regions and reduce the polarizability and the dielectric constant. It should be noted that the process of pressing the bulk powder leaves a fraction of the volume of the pellet occupied by porosity. This causes the density of the pellet to be lower then the theoretically expected value and it consequently also lowers the measured dielectric constant. While we were not able to determine the volume fraction of the porosity in the specimens, the dielectric constant of the pure polymer with no porosity is likely to be higher than shown.

Although a molecular wire on a smooth metal surface depends on a one-dimensional bonding mechanism for conduction, poly-$[Rh(pdi)^{+}_{4/2}(Cl)^{-}]_n$ has bonding in two dimensions, in-plane and out-of-plane. This means that the conductivity is extremely sensitive to even a small change in the concentration of the connected Rh-Rh molecular wires. This sensitivity is evident in these experiments, where a reduction in the Rh-Rh bonded regions by a factor of two has caused the conductivity to decrease by a factor of 100. This might also explain the decrease in the dielectric constant. The drop in dielectric constant is explained in terms of a decrease in the average length of the domain that a charge carrier can traverse. Initially, the material has a large polarizability owing to the mobility of charge carriers on these extended conductive regions. The length of these highly conductive domains decreases as the metal-metal bonding decreases. This would cause the polarizability to decrease, decreasing the dielectric constant. In light of these results, a degradation mechanism, similar to that observed in SAMs [4], is proposed to cause the change in the electrical properties of poly-$[Rh(pdi)^{+}_{4/2}(Cl)^{-}]_n$.

The long-range Rh-Rh chains are the most electrically important features of this polymer. As

these have been shown to be the most electrically conductive bonds in the material [19], the existence of the (001) peak in the X-ray diffraction pattern is of primary importance if a one-dimensional metal is desired. Because the samples were stored in air, an oxidative process is suspected of introducing disorder into the delicate lattice supporting the extended Rh-Rh chains. This would indicate a reduction in Rh-Rh interactions over time, possibly owing to chemical attack at the isocyanide moiety.

This hypothesis is supported by the TGA analyses. Under nitrogen, the initial decomposition starts at 300 °C and a secondary one at 425 °C, consistent with a previous report [23]. Under oxygen, the initial decomposition starts at 260°C and is accompanied by the appearance of an absorbance peak at 2270 cm^{-1} in the FT-IR spectrum, visible in the inset of Figure 3.9. This absorbance peak in the IR suggests that an isocyanate (N=C=O) is most likely present in the polymer [4]. Because the boiling temperature of 1,4-phenylene diisocyanate is 260 °C, the conversion of diisocyanide to diisocyanate would proceed according to Equation 3.5.

$$(\mathrm{Rh} \leftarrow \mathrm{C} \equiv \mathrm{N} - \mathrm{R} - \mathrm{N} \equiv \mathrm{C} \rightarrow \mathrm{Rh})^{2+} + 2\mathrm{Cl}^{-}(\mathrm{s}) \xrightarrow{\mathrm{O_2}\ 260^\circ}$$
$$2\mathrm{RhCl}(\mathrm{s}) + 2(\mathrm{O} = \mathrm{C} = \mathrm{N} - \mathrm{R} - \mathrm{N} = \mathrm{C} = \mathrm{O})(\mathrm{g}) \qquad (3.5)$$

This process is certainly accelerated in the TGA by high temperature and the presence of an oxygen-rich environment, but it may occur more slowly in air at room temperature. In addition, the close proximity of adjacent Rh(I) atoms might enable them to insert O^{-2} into nearby isocyanide moieties through diatomic cleavage [77]. If so, it would indicate that the degradation process involves the insertion of oxygen into the N≡C→Rh bond to form N=C=O(Rh). The effect of this oxidation is not only to stop any in-plane conduction, but also to disrupt Rh-Rh bonding, decreasing the crystallinity and lowering the conductivity.

By analysis of chemical shifts in the N 1s binding energy, the presence of a non-isocyanide species in poly-$[\mathrm{Rh(pdi)}^{+}_{4/2}(\mathrm{Cl})^{-}]_n$ is apparent. A binding energy between 399.9 - 400.6 eV has been assigned to metal bonded isocyanides [65,67]. N 1s peaks with lower binding energies in these systems, from 399.3 to 398.7, have been assigned to polyisocyanides [65, 67] and isocyanates [4]. As shown in Figure 3.10, the N 1s peak of the sample held under Ar showed two peaks when

deconvoluted: a smaller peak centered at 399.3 eV and a larger one at 400.6 eV. Upon extended exposure to lab air, the resulting spectrum shows the peak at 400.1 eV greatly reduced, but the peak centered at 399.3 eV now much larger, consistent with a conversion from isocyanide to isocyanate.

In like manner, the C 1s peak, shown in Figure 3.11, can be fitted with two curves. In both samples, the lower binding energy (BE) peak at 284.8 eV is fitted to aromatic carbon. Because of the strong upward shift observed in the C 1s peak observed for isocyanides [78], the higher BE peak, at 286.2 eV for the sample stored in argon and 286.4 eV in air, is assigned to carbon in isocyanide. The isocyanide peak is the larger of the two in the sample stored under argon, but the smaller of the two in the sample stored under air. This shift to a lower binding energy could be attributed to adventitious carbon, but that is unlikely, as both samples were stored in sealed containers under identical conditions (except for atmosphere). Instead, the decrease is attributed to the conversion of isocyanide to a lower BE isocyanate, similar to the decrease in BE observed in methyl isocyanide [78].

It can be speculated that the effect of the high-temperature oxidation is the same as that observed in the room-temperature oxidation of poly-$[Rh(pdi)^{+}_{4/2}(Cl)^{-}]_n$. Evidence for this is given by the decrease in the metal-isocyanide bonding present in the polymer and the disruption of the metal-ligand lattice necessary for metallic conduction. It should be noted that the lower BE peak could also be caused by a conversion of isocyanide to polyisocyanide, generally denoted by an N 1s peak in the XPS around 398.7 [4, 6, 65, 66]. While we cannot rule this out, we do not expect it because the IR showed no evidence for the formation of polyisocyanides in the poly-imide region (1570 - 1670 cm^{-1}).

There are some IR peaks that do not support the proposed oxidation mechanism from poly-$[Rh(pdi)^{+}_{4/2}(Cl)^{-}]_n$ to poly-[RhCl (phenylene diisocyanate)]. Although a shoulder at 2267 cm^{-1} was visible after high temperature oxidation, this feature did not appear on room temperature samples, even for long aging times. Moreover, there was no noticeable decrease in the isocyanide peak at 2138 cm^{-1}. It is possible that, at room temperature, the oxidation is occurring principally at the surface of the specimen pellets, while the interior remains largely unaffected. This would imply that a pellet of this powder would be composed of crystalline, conductive grains surrounded by an oxidized shell of amorphous insulating materials. The O 1s peak in the XPS was also found

to be invariant to atmosphere, appearing in samples stored under air and Ar. If a conversion from N≡C→Rh ⇒ N=C=O(Rh) was taking place, the O 1s signal in the XPS would be expected to increase accordingly. However, the presence of the O 1s peak may also be attributed to unreacted carbonyl in the specimens or contamination by ambient moisture prior to insertion into the XPS chamber [22]. Even so, our data indicates that the changes in conductivity, dielectric constant, color, and crystallinity are not coincidental, but directly caused by an oxidative process occurring in ambient conditions.

3.4 Conclusions

The estimated electrical conductivity of poly-$[Rh(pdi)^{+}_{4/2}(Cl)^{-}]_n$ of 3.4×10^{-11} S·cm^{-1} at room temperature is far less than what had originally been reported by previous investigators [62]. This difference is attributed to the lack of proper measurement technique. The present research indicates that this conductivity showed a strong dependence on the metal-metal stacking interactions of the Rh atoms in the polymer. The drop in the intensity of the (001) peak, attributed to a loss in Rh-Rh bonding, and the conductivity upon exposure to air showed a direct correlation with one another. This sensitivity to air is attributed to the oxidation of the ligand at the Rh atom. Thermogravimetric analysis taken in oxygen indicates that there is a decomposition that takes place at 260 °C, attributed to an isocyanide - isocyanate conversion. Evidence of this conversion is also seen in the N 1s and C1s regions of the XPS, where exposure to air appears to produce an isocyanate in the polymer. This research shows that further attention is required before poly-$[Rh(pdi)^{+}_{4/2}(Cl)^{-}]_n$, and any other materials that incorporate metal-isocyanide bonds, see widespread use as molecular conductors.

CHAPTER IV

COPPER TEREPHTHALATE: SYNTHESIS, AND STRUCTURE

4.1 Introduction

One of the early metal terephthalate complexes characterized as porous MOFs, was a copper terephthalate trihydrate Cu(II)(TPA)·3H_2O synthesized by Cueto et al. [36], which was further studied for conductivity and magnetic susceptibility [79]. The first copper terephthalate with a large surface area was reported by Mori et al [42,80]. The presumed structure was one of a paddlewheel similar to the MOF-2 structure that would be reported one year later [41]. But no structure was ever provided by them or anyone else. There have been mono- and di-hydrated copper terephthalate complexes reported by Deakin et al. [81], but these structures have a different coordination geometry and they lack the lamellar, paddlewheel coordination geometry predicted by Mori. One apparent attempt at the solvothermal synthesis of the paddlewheel Cu(TPA) complex yielded Cu(TPA)($NHMe_2$)$_2$, achieved by the hydrolysis of DMF during synthesis [82]. However, this resulted in a 5-coordinate square-pyramidal Cu, where only three of the bonds were composed of TPA and two were the ligand NHMe. Another similar structure reported was the Cu(1,3-BDC)(H_2O) reported by Gao [83].

Research groups have since used copper terephthalate as a platform for the construction of MOFs with larger porosities, incorporating triethylenediamine [84] and dimethylamine [82]. However, we know of no published structure of copper terephthalate. As applications of MOFs for catalysis are investigated, MOFs with open coordination sites, like copper terephthalate, will be scrutinized for both homogeneous and heterogeneous catalytic behavior [33]. The Cu(TPA) MOF, though similar to MOF-2, has exhibited a markedly higher surface area, making it a superior candidate for gas separation and sieving applications. Unlike MOF-2, the magnetic properties of Cu(TPA) also render it an attractive template for the development of high surface area magnetic materials. A solvothermal version was later developed by BASF [46]. Other groups have used electrochemical methods to speed up the synthesis [85].

Although the structure of MOF-2 and some of the associated polymorphs are well studied

[43, 45, 86, 87], we know of no equivalent high-throughput syntheses for the isostructural copper terephthalate. Along similar lines, we have used DMF at elevated temperatures and ambient pressure to carry out the reaction shown in Equation 4.1.

$$Cu(NO_3)_2 + C_6H_4(COOH)_2 \xrightarrow[\text{Air, } 110^\circ C]{\text{DMF}} Cu[C_6H_4(COO)_2]_n + 2HNO_3 \quad (4.1)$$

4.2 Results

4.2.1 Single crystal synthesis and structure

As the only previous synthesis for this framework was one that created micrograms over weeks [42], we endeavored to expand the options available for synthesis of Cu(TPA) in the absence of one that would generate large quantities suitable for bulk measurements. This led to a series of experiments where many different solvents were used under high-pressure solvothermal conditions including hexane, pyridine, water, methanol, and DMF. The results often included a shiny metal deposit on the sides of the reaction vessel, indicating the reduction of the metal salt. This two-phase mixture was deemed unsuitable for bulk methods, and was not used. Finally, a method was found whereby the reaction could be placed in a scintillation vial, capped off, and placed in an oven at 100 °C overnight. The resulting solid appeared to be a single phase blue crystalline material.

The analysis of single crystals of the resulting blue powder generated by our novel high-throughput synthesis, yielded a framework of Cu(TPA)·(DMF), depicted in Figure 4.1. This structure consists of a dimer of Cu cations, each of which is coordinated in square-planar fashion to the same four terephthalate anions. This then creates large sheets of square grids. At the apical position on each Cu cation is coordinated one molecule of DMF through the O atom on the DMF. Each sheet is staggered by a stacking fault of [1/2, 1/2], creating an AB structure. The sheet-like grid and the stacking fault create a pore where two Cu-coordinated DMF molecules are located. The ORTEP depiction of the asymmetric unit, along with atomic positions, bond lengths, and angles is included in the appendix.

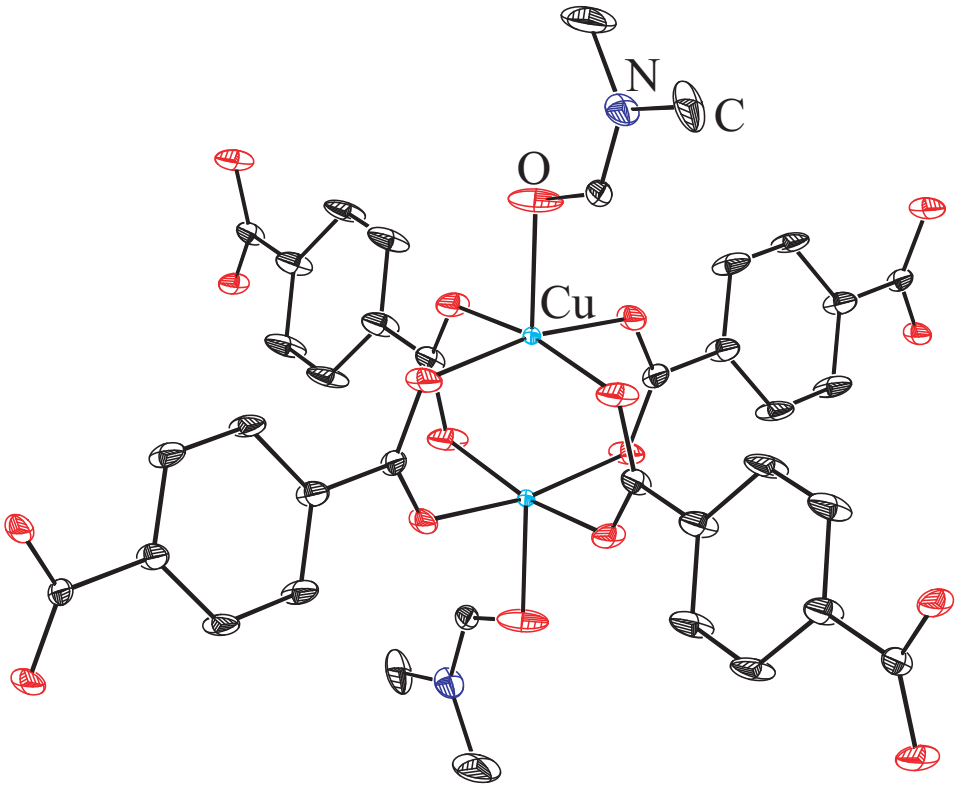

Figure 4.1: A depiction of the sheet-like crystal structure Cu(TPA)·DMF. Thermal ellipsoids are drawn at 50% probability [88].

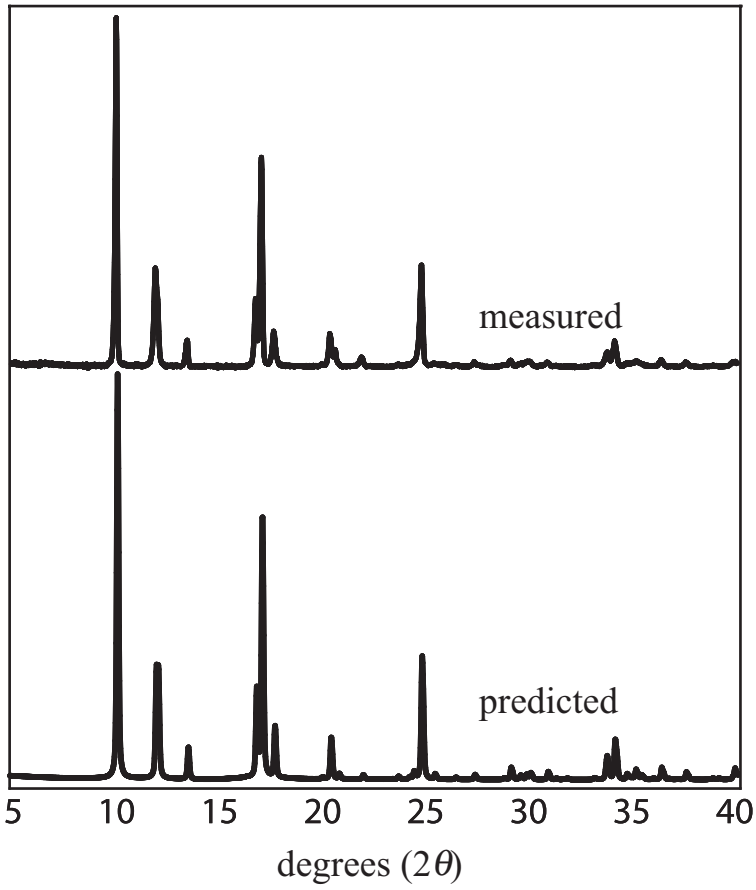

Figure 4.2: A comparison is shown between the measured powder diffraction profile taken from a sample of Cu(TPA)·DMF synthesized in open air and the predicted powder pattern based on the structure solution of the single crystal of Cu(TPA)·DMF [88].

4.2.2 High-throughput synthesis

It was found that the same reaction takes place in a round bottom flask at 125 °C under ambient conditions. This meant that large quantities can be made with relative ease in a matter of hours. We carried out X-ray powder diffraction experiments to verify the crystal structure assignment of Cu(TPA)·DMF synthesized under ambient conditions in a round bottom flask and to examine the effect of temperature and solvent on the crystal structure. The similarity of these scans, shown in Figure 4.2, demonstrate that the moderate pressures and controlled atmosphere needed for high-quality single crystal growth were not necessary to make large quantities of powder.

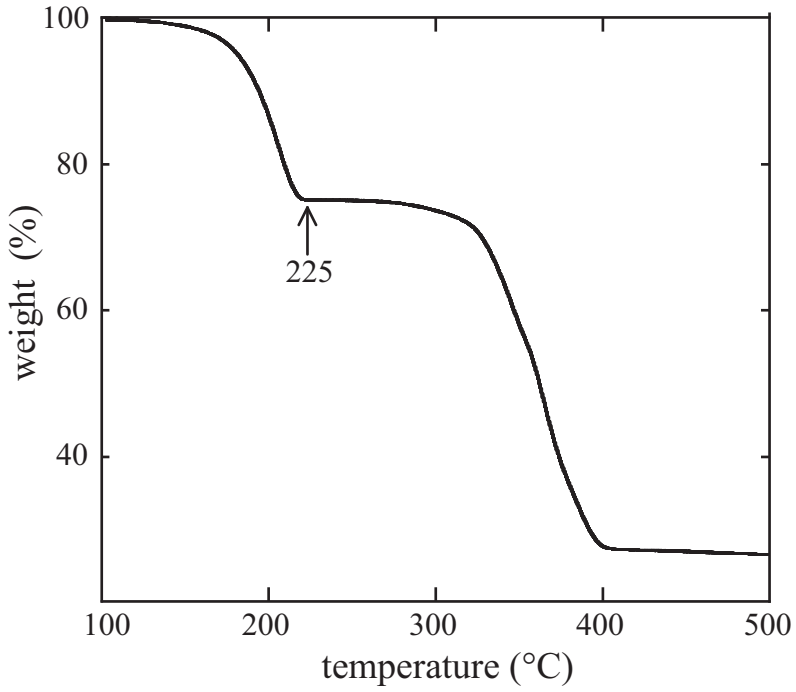

Figure 4.3: The thermogravimetric analysis (TGA) trace of Cu(TPA)·DMF shows two clear weight loss events, one from 180 to 220 °C and another from 300 to 400 °C. These weight loss events are attributed to desolvation of Cu(TPA)·DMF to Cu(TPA) and structural collapse, respectively [88].

4.2.3 Thermo-gravimetric analysis

Because large amounts of powder could be easily and quickly synthesized, thermogravimetric measurements were conducted to determine the thermal stability of the resulting solid. As shown in Figure 4.3, there are two clear weight loss steps, indicating that the DMF molecule present after synthesis can be removed through thermal desorption, yielding a desolvated structure referred to as Cu(TPA). This transition is also visible in a high-temperature XRD powder diffraction scan, shown in Figure 4.4.

4.2.4 Infrared spectroscopy

IR measurements were carried out to determine the characteristic IR absorbances and to confirm the loss of solvent at 225 °C. Figure 4.5 shows the results of measurements taken before and after thermal desolvation. Observe how three peaks at 675, 1105, and 1663 cm^{-1} disappear after solvation. A more detailed and annotated graph is shown in Appendix A in Figure A.2. Table 6.1 in Chapter 6 features more detailed lists of prominent peaks and their assignments.

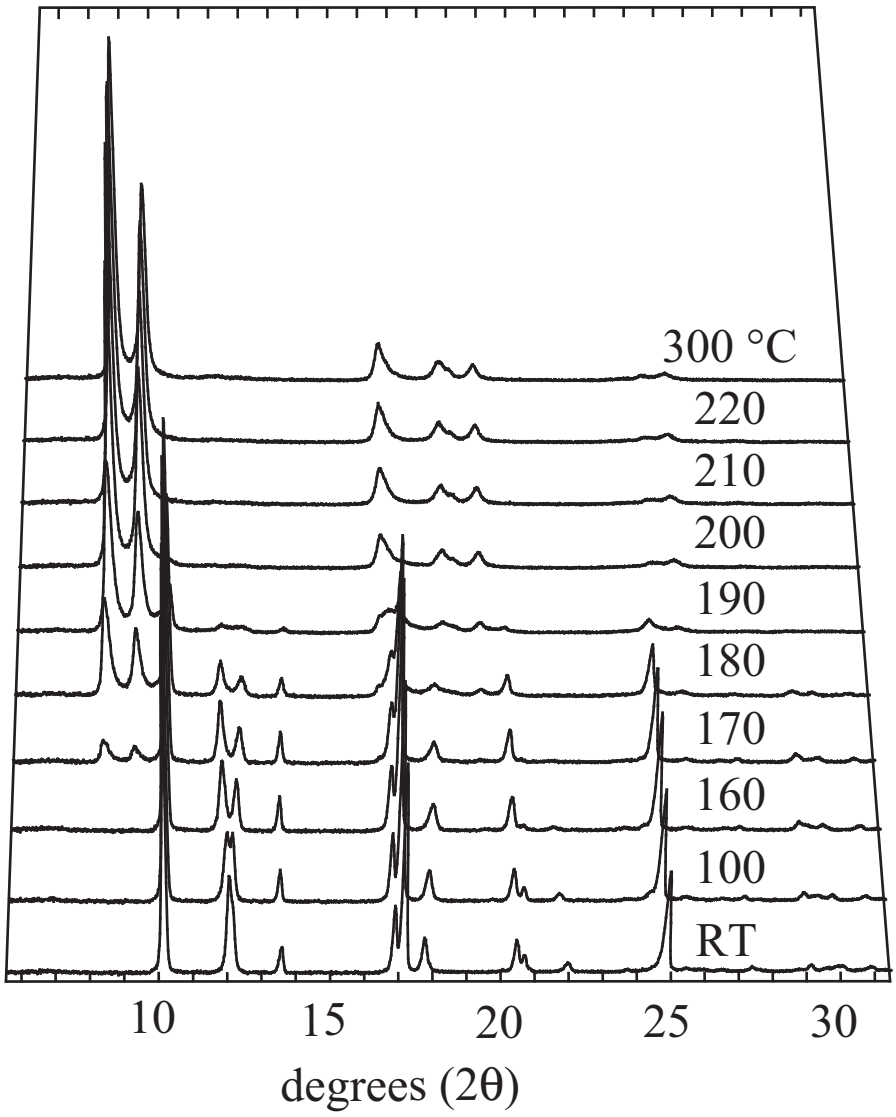

Figure 4.4: This series of powder X-ray diffraction traces shows the transition in structure from Cu(TPA)·DMF to Cu(TPA) in increments of 10 °C. Note that the pattern of the Cu(TPA) remains stable above 300 °C [88].

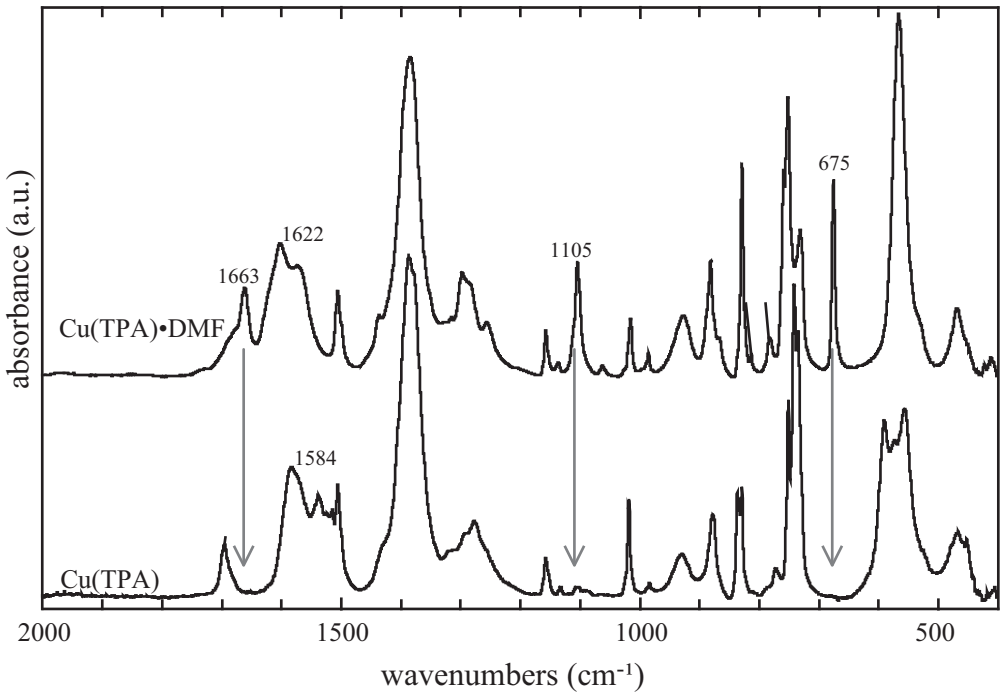

Figure 4.5: The IR spectra of Cu(TPA)·DMF prior to desolvation, and Cu(TPA) after desolvation are shown. The peaks at 675, 1105, and 1663 cm^{-1}, present in Cu(TPA)·DMF, disappear after thermal desolvation. Moreover, the $\nu(COO)_{a,op}$ shifts from 1622 to 1584 cm^{-1} [88].

4.2.5 Desolvation and solvent rewetting

A specimen of desolvated Cu(TPA) powder was washed in N methyl pyrrolidone (NMP) at 120 °C for 30 min. We also exposed the desolvated Cu(TPA) to a similar treatment in ethanol, refluxing for 30 min. X-ray powder diffraction scans, shown in Figure 4.6 of these specimens were taken to determine the ability of the framework to re-coordinate solvent after desolvation. Apparent in these scans is the similarity between the Cu(TPA)·DMF prior to desolvation and powder pattern present after the desolvated powder was exposed to NMP. What is also clear is that exposure to ethanol did not have the same effect as exposure to NMP, as the powder pattern was not significantly changed from that of the desolvated Cu(TPA).

4.2.6 Surface area and porosity

Gas sorption experiments were performed to estimate the effect of DMF removal on the microporosity and accessible internal surface area of the metal organic framework. Sorption with N_2 at 77 K revealed that the evacuated structure shows a type I isotherm (shown in Figure 4.7) with a BET

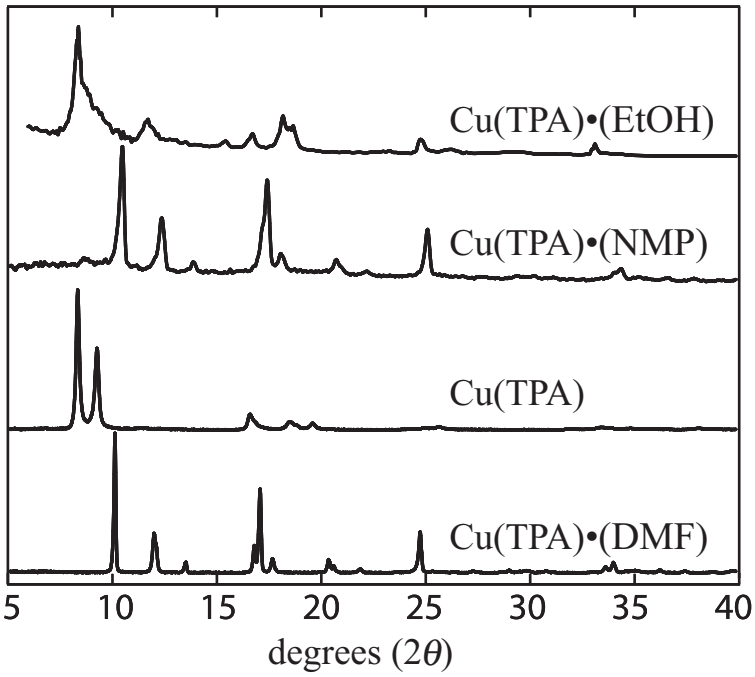

Figure 4.6: The X-ray powder diffraction scans of Cu(TPA) under four different solvent environments are shown. Cu(TPA)·EtOH, Cu(TPA)·NMP, Cu(TPA), and Cu(TPA)·DMF correspond to Cu(TPA) washed in ethanol, Cu(TPA) washed in NMP, desolvated Cu(TPA), and freshly synthesized Cu(TPA)·DMF. Notice how the Cu(TPA)·NMP and Cu(TPA)·DMF have similar patterns, indicating similar coordination, while the similarity between the Cu(TPA)·EtOH and the desolvated Cu(TPA) indicates that ethanol cannot coordinate to the Cu as effectively [88].

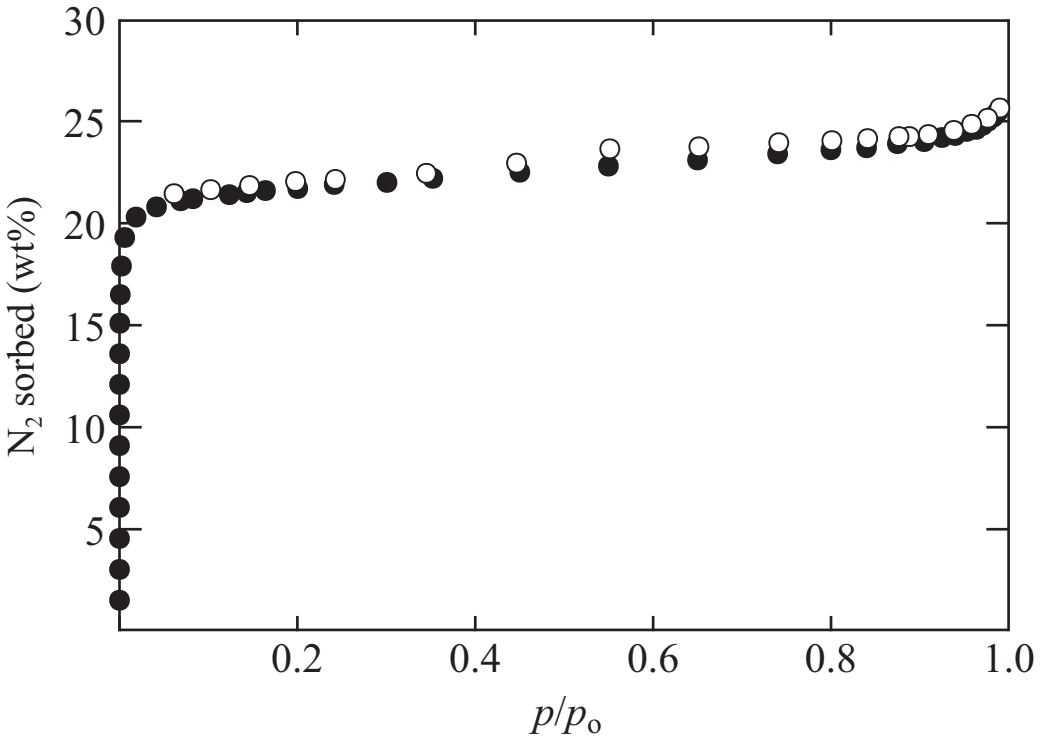

Figure 4.7: The adsorption of N_2 on Cu(TPA) at 77 K shows a type I isotherm with BET surface area of 625 m^2g^{-1} [88].

surface area of 625 m^2g^{-1}, a Langmuir surface area of 752 m^2g^{-1} and a micropore volume of 0.282 cm^3g^{-1}. The monolayer volume of 181 cm^3g^{-1} (at STP) indicates that the uptake of N_2 at 77 K is 22.8% on a mass basis.

4.2.7 Magnetic Susceptibility

Magnetization experiments, shown in Figure 4.8, were carried out to examine the magnetic susceptibility of Cu(TPA)·DMF. These experiments were conducted to determine the extent of interaction between adjacent copper atoms in a dimer. To verify the gyromagnetic radius, electron paramagnetic resonance measurements were also carried out on an identical specimen. The results of these measurements are shown in Figure 4.9. Visible in the EPR measurement is the large resonance corresponding to a *g*–factor of 2.12. This resonance appears to be broadened by the presence of paramagnetic impurities in the solid.

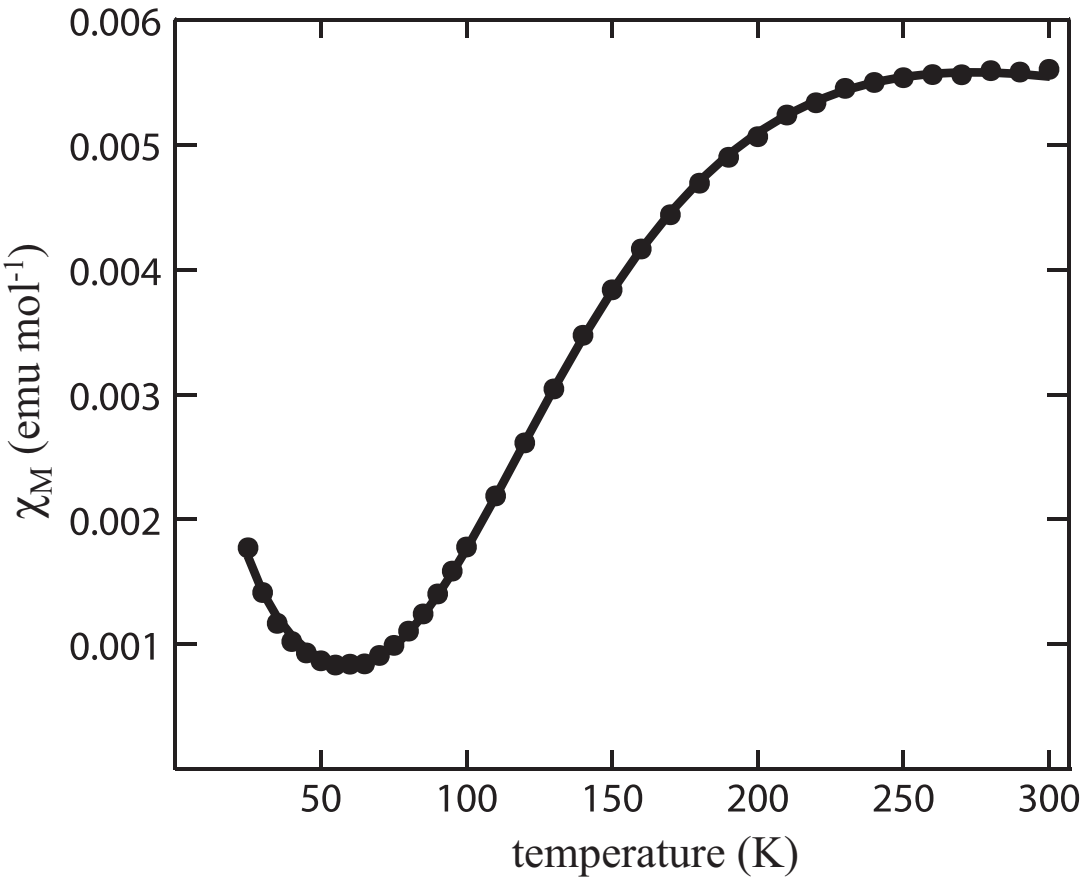

Figure 4.8: The magnetic susceptibility indicates an antiferromagnetic coupling between adjacent copper atoms in the same dimer of J = -311 cm^{-1} [88].

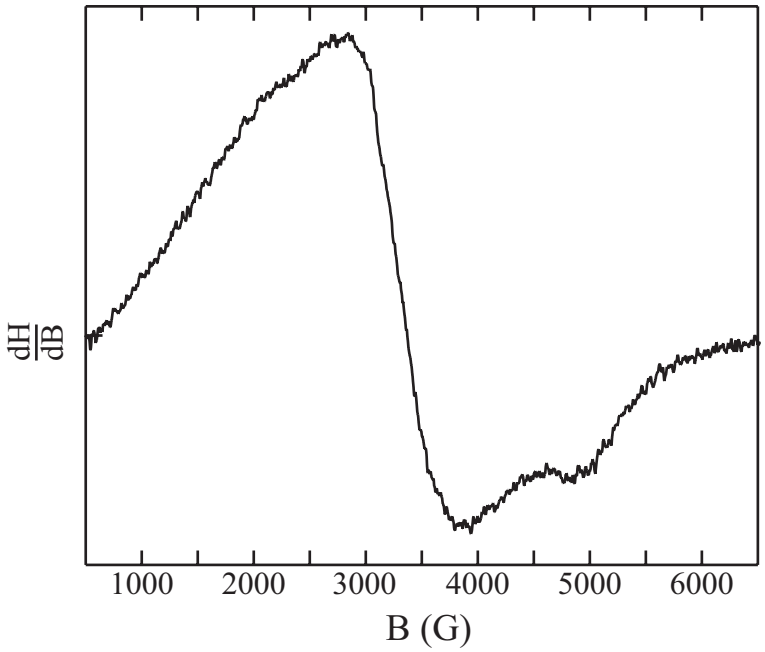

Figure 4.9: The electron paramagnetic resonance curve indicates that the major radical indicates that the gyromagnetic factor corresponds to g = 2.12. There also appears to be a secondary radical at g = 1.53 that remains unassigned [88].

4.2.8 Electrical conductivity

The electrical conductivity of a sample of Cu(TPA)·DMF was measured as a comparison to the poly-$[Rh(pdi)^{+}_{4/2}(Cl)^{-}]_n$. The results of the ac impedance measurement are shown in Figure 4.10. Although only ac data was collected, the incomplete semi-circle in the complex impedance plane allows the extrapolation of the dc conductivity of 4×10^{-12} S·cm^{-1}. This appears to be equivalent to the insulating form of the poly-$[Rh(pdi)^{+}_{4/2}(Cl)^{-}]_n$, indicating little metal to metal electron transfer, if any.

4.3 Discussion

Terephthalate ligands are coordinated in this complex in a bi-dentate bridging fashion to a Cu(II) dimer, separated vertically by 2.63 Å. Each Cu(II) atom is also coordinated to a molecule of DMF, giving the Cu(II) atoms a square pyramidal coordination geometry. This leads to a structure where the Cu(II) atoms are coordinated to the TPA linkers in the ($\overline{2}$ 0 1) planes. These sheets are then bonded through weak stacking interactions, similar to MOF-2 [41]. Clausen et al. reported the structure of a polymorph of MOF-2 that has the same space group and similar unit cell parameters

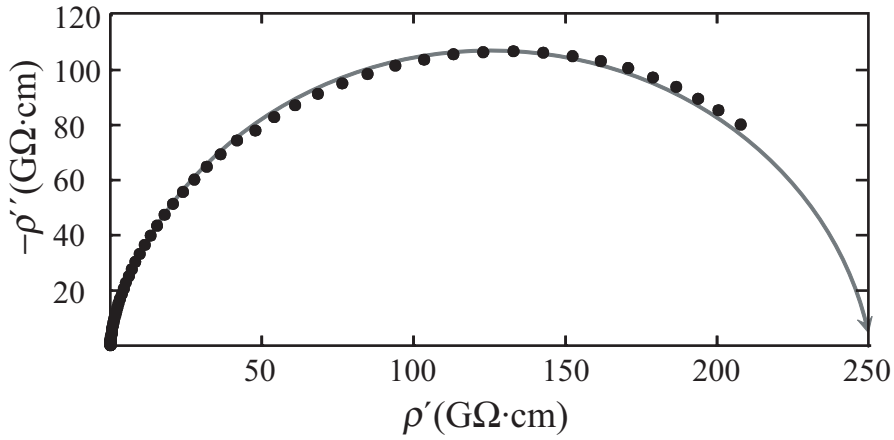

Figure 4.10: The complex impedance of Cu(TPA)·DMF, shown above, indicates a DC conductivity of 4×10^{-12} S·cm^{-1}, equivalent with the insulating form of the poly-$[Rh(pdi)^{+}_{4/2}(Cl)^{-}]_n$.

[45].

The crystal structure of the Cu(TPA)·DMF indicates that the solvent DMF molecules are occupying the pore spaces, indicating the need for thermal activation if a high surface area material is desired. The consequent measurement of the thermogravimetric profile shows a clear weight loss step starting at 160 °C and ending by 220 °C. This weight loss of 26% corresponds well to the loss of one solvent molecule per monomer, leading to a desolvated Cu(TPA) phase. The hypothesis that this weight loss is effected by the loss of solvent is supported by IR measurements. After being dried at 225 °C, the IR peaks at 675, 1105, and 1663 cm^{-1} corresponding to DMF can no longer be seen, while the Cu(TPA) is still very visible. The stability of the phase above 220 °C is indicated by the fact that there is no significant weight change until pyrolysis at 325 °C.

The IR spectrum also provides information about the effect of solvent coordination on the solvent and on the framework. The DMF ν(CO) appears red-shifted from the usual value of 1676 cm^{-1} for the free molecule to 1663 cm^{-1} for a molecule that is coordinated to the Cu(II) center. This is explained in terms of electrostatic interactions between the compensated Cu(II) ion and the electronegative lone pairs on the O of the carbonyl. This results in a destabilization of the OC bond and a red-shifting of the ν(CO). The asymmetric stretch of the carboxylate group of the TPA, ν_a(COO), also appears to be blue-shifted in the presence of DMF. After removal of the DMF at 225 °C, the $\nu(COO)_{a,op}$ red-shifts from 1622 cm^{-1} to 1584 cm^{-1}. This would be an indicator that the DMF is stabilizing the coordination of the carboxylate ligand to the Cu metal center, possibly through the O

atom on the DMF.

This hypothesis was also supported by the comparison of rewetting with NMP and ethanol. After treatment with NMP, the washed powder had a powder diffraction pattern almost identical to the original Cu(TPA)·DMF. This indicates that, like DMF, NMP coordinates to the Cu(II) through the carbonyl group. The effect of the treatment in ethanol was different than that using DMF or NMP, as the diffraction pattern appears to become a more amorphous version of the original desolvated structure. This indicates that the ethanol, lacking the appropriate carbonyl group, does not coordinate to the Cu(II) in the same way that DMF and NMP do. This selectivity for coordinating certain functional groups over others would make Cu(TPA) a candidate for molecular sieving and gas separation applications. This also indicates that the structure could be modified by exposure to different solvents, tailoring the chemical properties and bond strength between adjacent Cu(TPA) sheets.

The results of the magnetic susceptibility measurements, shown in Figure 4.8, indicate a strong antiferromagnetic coupling between adjacent metal centers with a small paramagnetic impurity. The temperature dependence of the molar susceptibility was modeled with the Bleaney-Bowers-Kahn Equation [89]

$$\chi_M = \frac{2N_a g^2 \mu_B^2}{k} \left\{ \left[3 + \exp\left(\frac{-J}{kT}\right) \right]^{-1} \frac{(1-\rho)}{T} + \frac{\rho}{4T} \right\} \tag{4.2}$$

Here, the spin Hamiltonian used is $\hat{H} = -JS_1S_2$. $\hat{H}$ denotes the operation between the singlet and triplet spin states (S_1 and S_2, respectively) in the Cu dimer, and $-J$ is the measure of the energy difference that arises between those two degenerate states in the presence of a magnetic field. N_a, g, μ_B, k, and T have the usual meanings as the Avogadro constant, gyromagnetic factor of the free electron, Bohr magneton, Boltzmann coefficient, and sample temperature, respectively. The symbol ρ denotes the fraction of uncoupled paramagnetic impurity atoms present in the sample. The line of best fit is indicative of J = -311 cm^{-1} and ρ = 1.1%. The Bleany-Bowers equation can also be used to fit the g-factor. Our attempts to do so, however, always resulted in abnormally high values of g. As a result, the X-band EPR was used to measure the g-factor directly. The trace of desolvated Cu(TPA) is shown in Figure 4.9. This can be done with $g = (h\nu/\mu_B H)$ where h, ν, and H, are Planck's constant, the measurement frequency, and magnetic field, respectively. Because the scan

is taken as a derivative, the value of H is read from the part of the curve with the highest negative slope. This calculation yields a value of $g = 2.12$ for the largest radical with a small radical centered at $g = 1.53$, attributed to an impurity. Taken together, the values for $-J$ and g are consistent with other Cu dimer complexes, including the similar compound synthesized by Mori [42, 90].

When thermally activated, the open porosity of the structure becomes available, yielding a BET surface area of 625 m^2g^{-1}, a Langmuir surface area of 752 m^2g^{-1}, and a micropore volume of 0.282 cm^3g^{-1}. These values compare favorably with the surface areas of 545 and 708 m^2g^{-1}, for the BET and Langmuir surface areas respectively, reported by Seki for Cu(TPA) synthesized in methanol [84]. It is interesting to note that, while Cu(TPA) and MOF-2 are structurally similar in many aspects, Cu(TPA) exhibits a Langmuir surface area and micropore volume roughly double that of MOF-2 (270 m^2g^{-1} and 0.093 cm^3g^{-1}, respectively for MOF-2) [41]. Cu(TPA) is also similar to the copper trimesate, HKUST-1 reported by Chui [91]. The principal difference is that HKUST-1 is coordinated in three dimensions to make empty FCC cubes with large square pores, whereas Cu(TPA) appears to have a lamellar geometry that creates two dimensional tunnels. Although Cu(TPA) has around half the surface area of HKUST-1 [92], it may be desired if confinement to one dimension is desired or as a comparison to determine the effect of pore geometry on a particular material property.

At this time, no solution has been found to the desolvated structure that possesses the properties of interest. As Figure 4.4 shows, this thermal desolvation of Cu(TPA)·DMF to Cu(TPA) corresponds to a change in the crystal structure. The change of Cu(TPA)·DMF to Cu(TPA) upon desolvation also results in the solid crumbling to a fine powder, bereft of crystals of sufficient quality to perform single-crystal analysis. The drastic reduction in crystallite size also results in size-broadening of the X-ray peaks. This makes structure solution from powder diffraction almost impossible. As a result, the structure of the desolvated Cu(TPA) could not be solved through conventional methods.

The Cu(TPA) phase is believed to consist of stack like sheets and form 1-dimensional channels with open porosity. Figure 4.11 depicts the channels that are believed to form upon desolvation. We suspect that this is the structure based on the similarity it shares with copper *trans*-1,4-cyclohexanedicarboxylate solved in 2007 [93]. Figure 4.12 shows a comparison between the predicted powder pattern based on the crystal structure from Cu *trans*-1,4-cyclohexanedicarboxylate

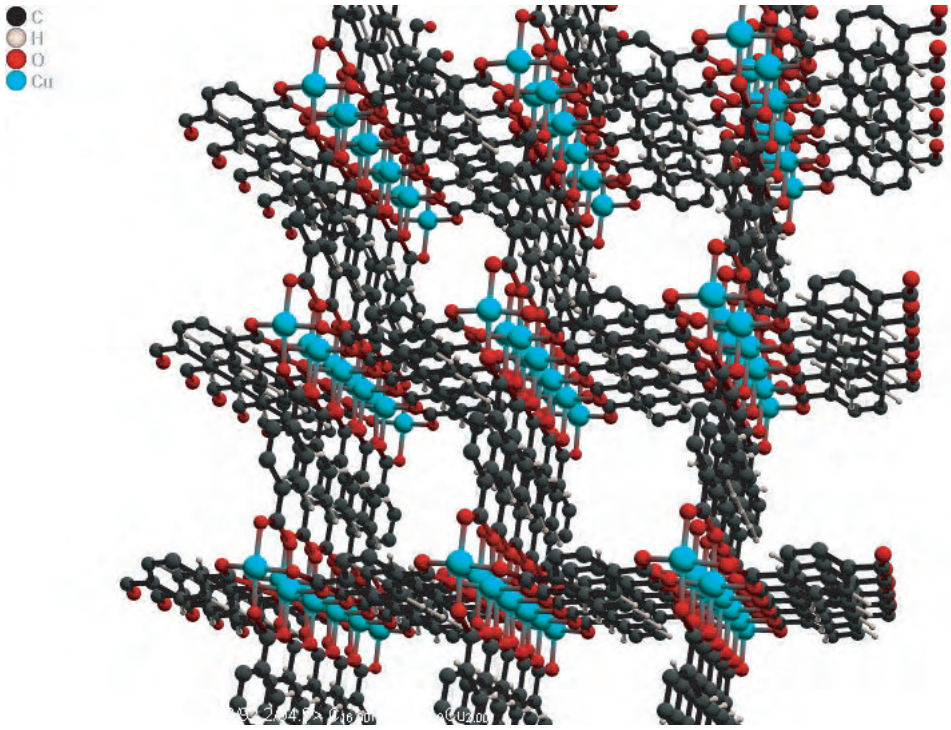

Figure 4.11: The hypothetical desolvated Cu(TPA) structure based on the solution to the copper *trans*-1,4-cyclohexanedicarboxylate crystal structure [88].

and Cu(TPA). Apparent in the figure is that, with the exception of two small peaks located at 11.5 and 13.9 °2θ, the patterns are so similar as to be almost identical. As a result, while the unit cell lengths and angles cannot be definitively resolved at this time, it is reasonable to assume that the structure of Cu(TPA) is similar to the one shown in Figure 4.11. As in Cu *trans*-1,4-cyclohexanedicarboxylate, Figure 4.11 shows the sheets of Cu(TPA) stacked almost directly atop one another. The stacking fault present in the solvated structure has disappeared and instead, the Cu atoms appear to be interacting with the carboxylate oxygens on adjacent sheets. As these sheets stack they appear to form one-dimensional tunnels consisting of phenyl rings along the sides and Cu dimers at the corners.

4.4 Conclusions

The results presented in this work indicate that the high-throughput synthesis of copper nitrate and terephthalic acid in DMF can yield large amounts of the copper terephthalate metal-organic framework with antiferromagnetic coupling and a surface area comparable to other high surface area materials. These properties make it a compelling candidate for application in gas separation and

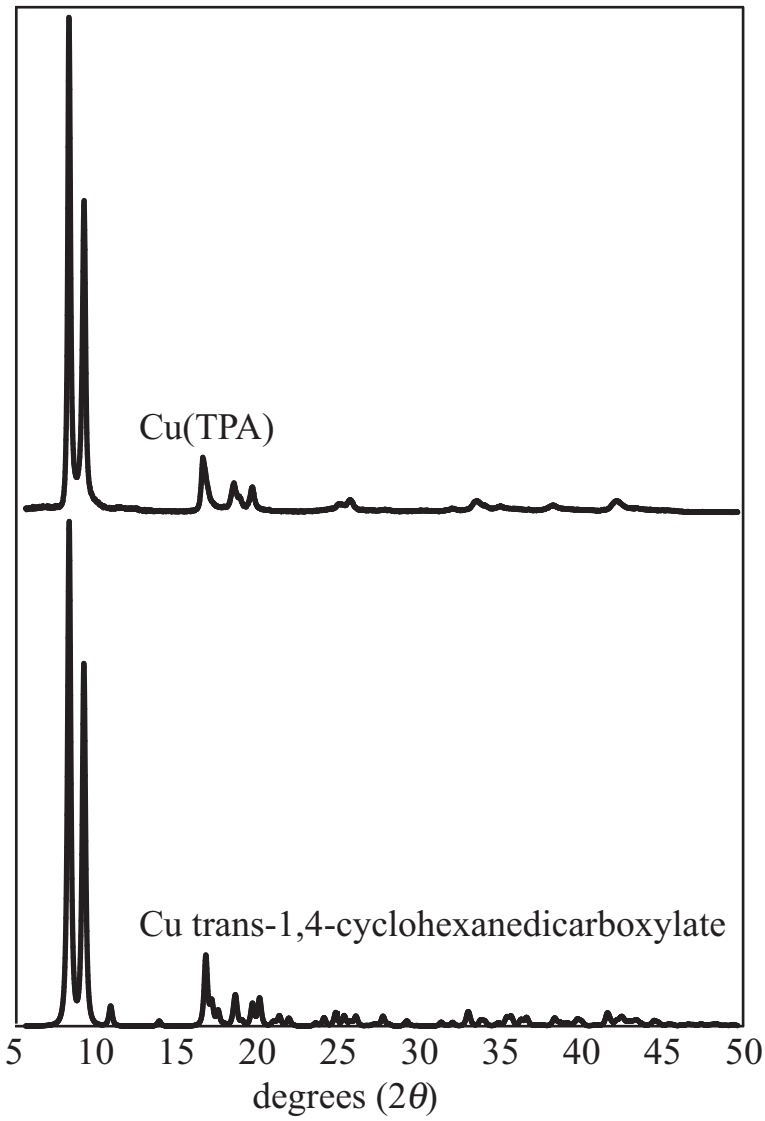

Figure 4.12: A comparison is shown between the experimental X-ray powder diffraction of Cu(TPA) and the predicted X-ray powder diffraction pattern of Cu *trans*-1,4-cyclohexanedicarboxylate.

sieving. The presence of the copper atom and its exposed apical coordination site might also lead to catalysis applications. The similarities of Cu(TPA)·DMF to other related frameworks indicate that novel magnetic materials could be synthesized by the introduction of a heterometallic center to the dimer. If the interest in MOFs like HKUST-1 and MOF-2 is any indication, then the synthesis method described here may have very broad impact on the development of MOFs with a potentially wide array of applications. We anticipate that this high-throughput synthesis and the details of the associated crystal structure of Cu(TPA) will pave the way for applications development and comparison among similarly synthesized MOFs.

CHAPTER V

SURVEY OF METAL TEREPHTHALATES

5.1 Introduction

We wanted to perform a limited comparison between the first row transition metal terephthalates of Co, Ni, Cu, and Zn as well as Mg. Our focus was restricted to those compounds that could be synthesized at 100 °C at ambient temperature in dimethylformamide. This would help us to understand the similarities and differences between these compounds, and thereby make clear which combinations of metal centers were most likely to have demonstrable effects compared to their unmixed counterparts. In addition, no such across the board comparison has been found in the literature, making this review potentially useful to other researchers attempting to draw correlations about the behavior of metal terephthalates as a function of metal center.

The magnetic properties of metal terephthalates have been vigorously investigated ever since the terephthalate anion was shown to mediate exchange coupling between unpaired spins on transition metal centers [94]. This has been particularly true of the metal hydroxyterephthalates of Co [95], Ni [96], and Cu [97]. With the exception of copper, the magnetic properties of simple metal terephthalates have received less attention. This may be related to the fact that the structure of Co terephthalate was reported recently [98], and yet, to our knowledge, the crystal structure of the corresponding Ni compound has not been reported. Fe and Mn terephthalates could not be studied on account of time restrictions.

5.2 Results

5.2.1 Optical microscopy

After syntheses described in the experimental section, an immediate analysis could be carried out by optical microscopy, shown in Figure 5.1. The colors in the Co, Ni, and Cu terephthalates are a natural consequence of the splitting in the d and d^* orbitals in metals with unfilled d subshells. These images revealed much about the nucleation and growth mechanics present under the synthesis conditions used. For example, the synthesis of Co(TPA) crystals was dominated by growth, as this

produced a few crystals that were larger in size than the others. On the other hand, the Ni(TPA) crystals were nucleation dominated, producing large clusters of small crystals. As the nucleation and growth process in these metal terephthalates has not been studied in detail, it is difficult to draw clear relationships between the metal species and the preference of nucleation or growth mechanism.

5.2.2 Powder diffraction

The powder diffraction traces corresponding to synthesized metal terephthalates are shown in Figure 5.2. The crystal structures of Co(TPA) and Zn(TPA) were well known at the start of the study, as reported by Fu [98] (for Co) and by Li [41], Edgar [43], and Hawxwell [44] (for Zn). The analogous structures for Mg, Cu, and Ni terephthalates were unknown at the start of the study. There was a structure for Mg(TPA) reported by Davies, but they chose dimethylacetamide instead of dimethylformamide. However, we have used their values, as the metal coordination environment is likely to be similar [99].

An attempt was made to solve the crystal structure for Ni(TPA)·DMF using data collected at the ChemMatCARS beamline at the Advanced Photon Source at Argonne National Laboratory. The crystal was nominally $Ni_{0.97}Cu_{0.03}$(TPA), as it had a small impurity of Cu in it, aiding in the crystallization, shown in Figure 5.3. Despite the rounded edges, a solution could still be obtained from single crystal diffraction. The solution indicated that the crystal was triclinic, space group P1 with a = 9.6194 Å, b = 14.2483 Å, c = 16.3213 Å, α = 109.079 °, β = 90.367 °, γ = 90.448 °, V = 2113.83 (6)Å^3, d_{calc} = 1.950 g·cm^{-3}. Because of the apparent presence of twinning in the crystal, the structure could not be refined below a standard discrepancy index of R = 0.12. The atomic locations, bond lengths and angles are listed in the appendix. However, shown in Figure 5.4 is the comparison between the predicted powder structure and the Ni(TPA) powder pattern, along with a depiction of the coordination environment around the Ni atom. While not identical, difference between the predicted powder pattern of the $Ni_{0.97}Cu_{0.03}$(TPA)·DMF crystal and the experimental powder pattern of the Ni(TPA)·DMF appears to be small enough that we can reasonably assume that the two structures are the same.

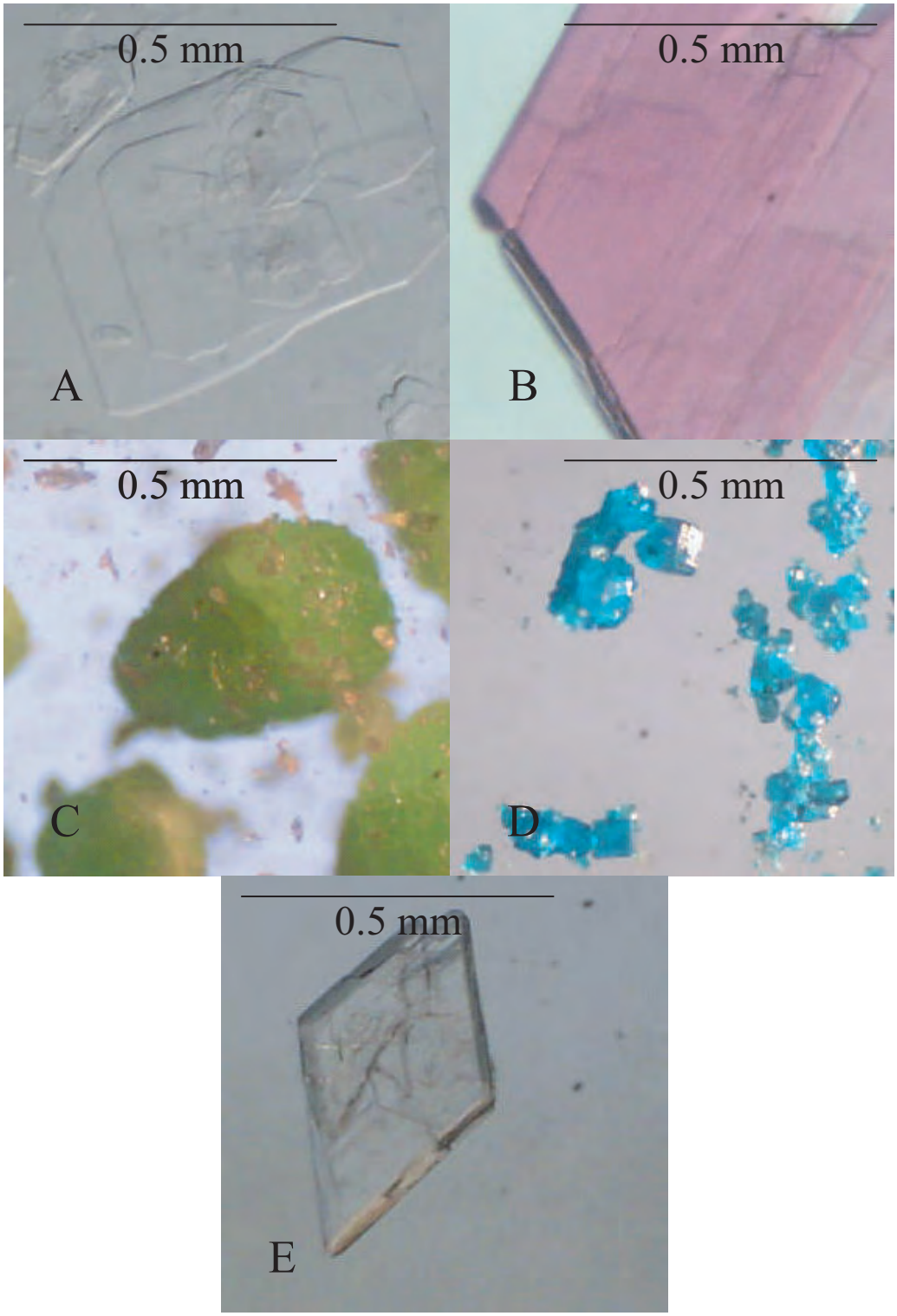

Figure 5.1: Optical micrographs show the different habits of Mg, Co, Ni, Cu, and Zn terephthalates.

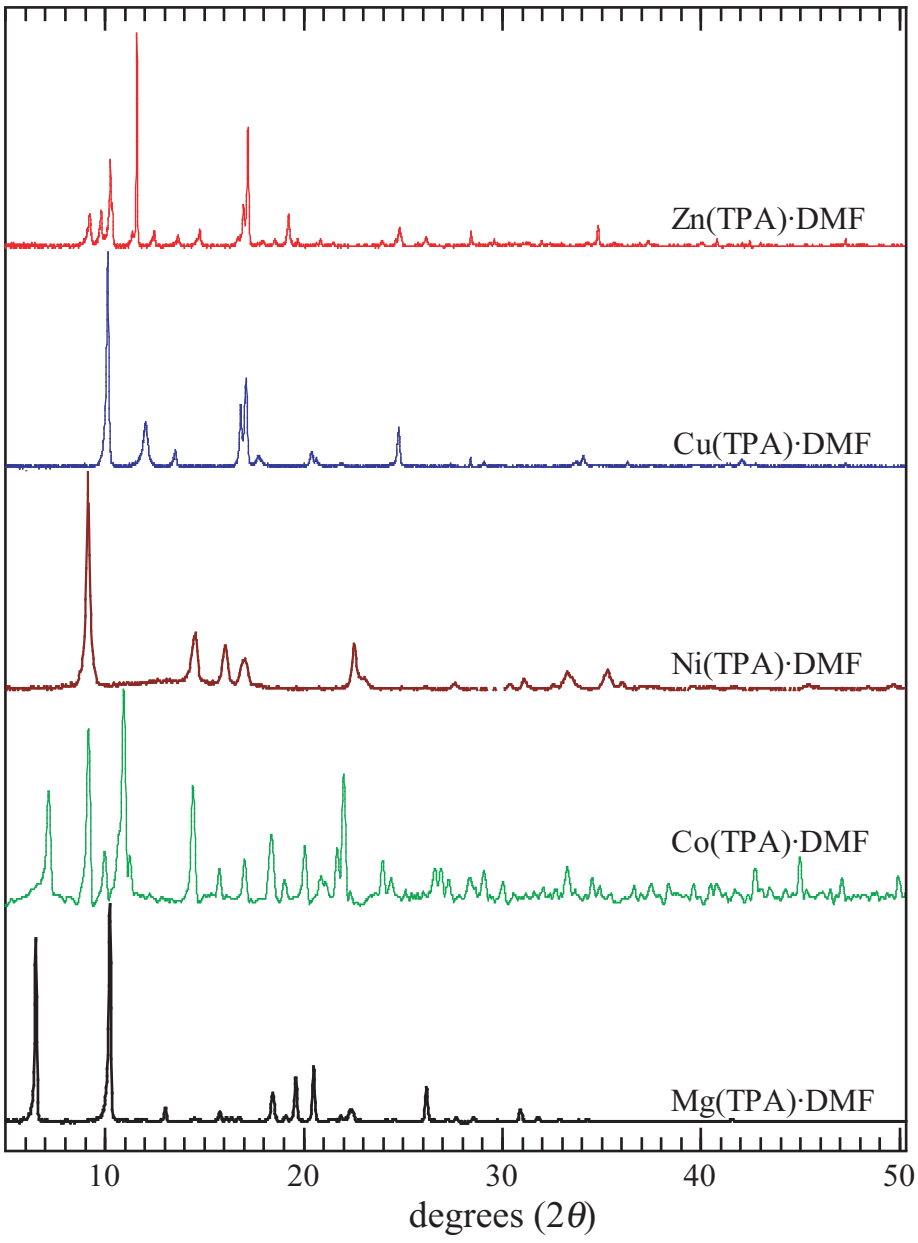

Figure 5.2: The powder diffraction patterns of solvated Mg, Co, Ni, Cu, and Zn terephthalates.

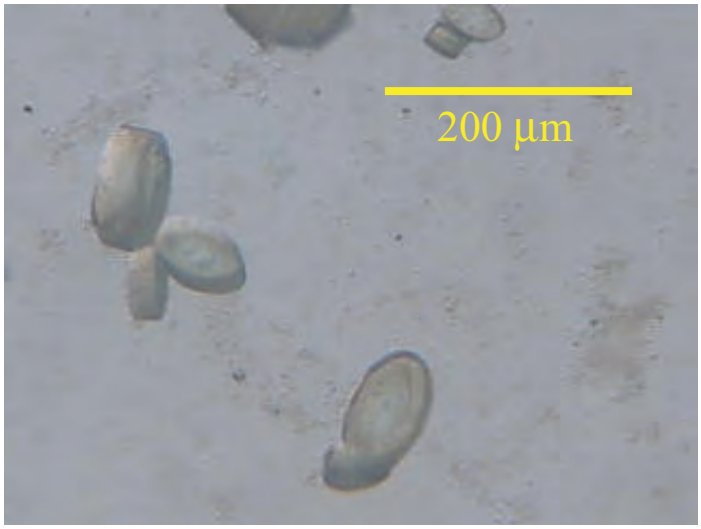

Figure 5.3: Micrograph shows $Ni_{0.97}Cu_{0.03}$(TPA) crystallites. Notice that the well shaped crystallites have rounded corners, often indicative of disorder. These were the same crystals that were sufficient for single crystal analysis to solve the structure described in Figure 5.4.

5.2.3 Thermal analyses

The thermal properties of the MOFs were investigated to isolate trends in the desolvation and pyrolysis temperatures. Previous reports for Zn(TPA) and Mg(TPA) have been made by Li [41] and Davies [99] respectively. Our findings on these materials are roughly in agreement with theirs. There are no previous reports of such studies on Cu(TPA), Co(TPA), or Ni(TPA). The thermogravimetric scans from these MOFs are shown in Figure 5.5. Despite the similarity in composition, there is a wide discrepancy for the desolvation temperatures (between 155 and 274 °C) as well as for the pyrolysis temperatures (between 314 and 514 °C). Also evident is that some of the metal terephthalates, like Cu and Zn(TPA) appear to desolvate in a single weight loss event, whereas this process appears to take two steps in the Mg, Co, and Ni(TPA). The temperatures and mass losses associated with each weight loss event are listed in Table 5.1.

5.2.4 Vibrational spectra and assignments

The FTIR spectra of the five metal terephthalates were recorded both before and after desolvation. Figure 5.6 shows the traces of the five metal terephthalates before and after desolvation. More detailed scans are also shown in the appendix in Figures A.1 to A.5. The peak locations and assignments from the spectra are shown in Tables 5.2 and 5.3. Some of the peaks could not be assigned.

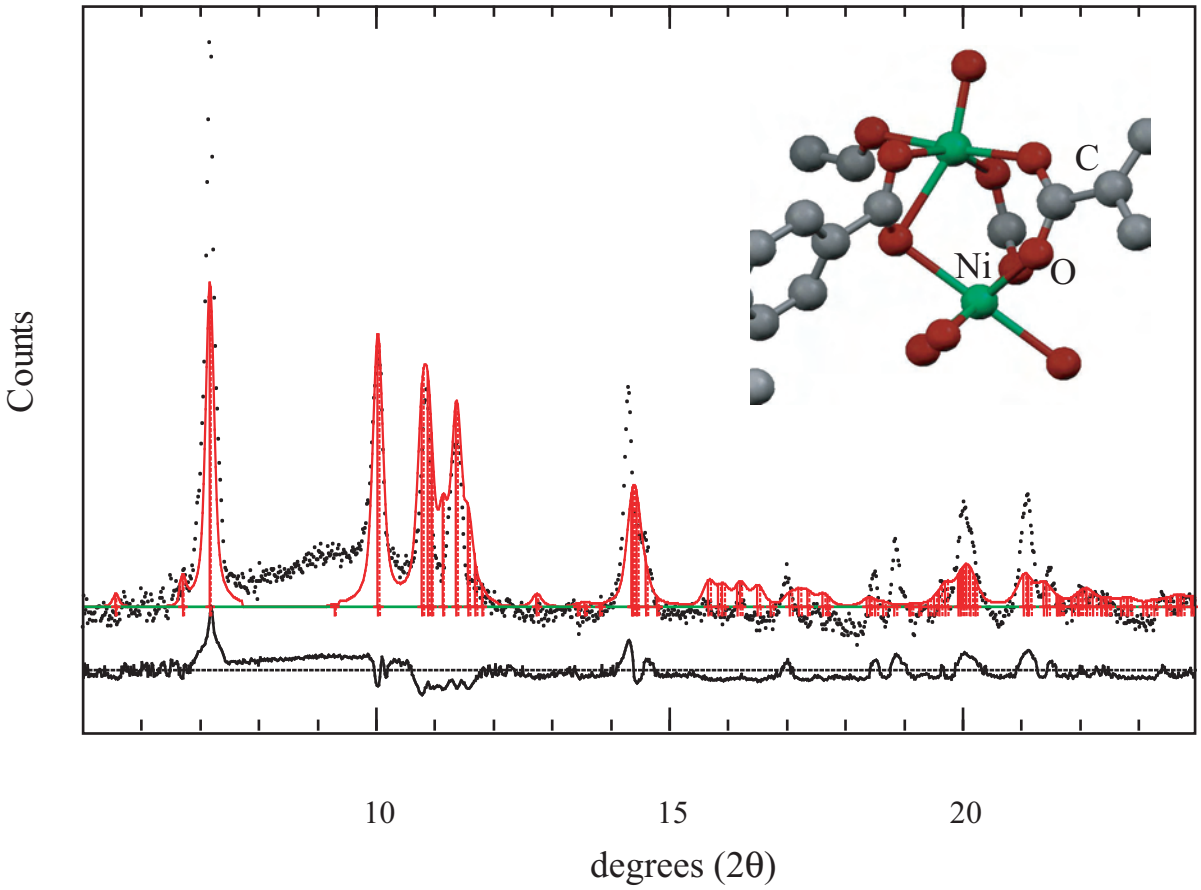

Figure 5.4: The powder pattern of Ni(TPA)·DMF is shown by the black dots. The red line corresponds to the predicted powder pattern from the solution of the $Ni_{0.97}Cu_{0.03}$(TPA) modeled as Ni(TPA). The black line beneath corresponds to the error between the two. The inset shows the coordination environment of the Ni atoms in the Ni(TPA) structure.

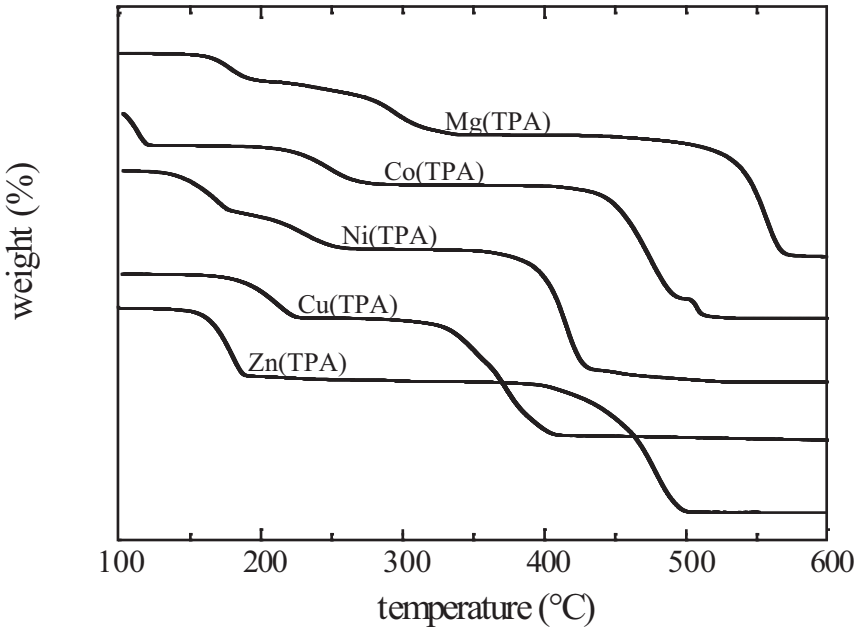

Figure 5.5: The thermogravitational traces of Mg, Co, Ni, Cu, and Zn terephthalates. Notice the similarity between the Ni(TPA) and Mg(TPA) traces. Both go through two sequential weight loss steps before pyrolysis from 400–600 °C. Likewise, the traces for Co, Cu, and Zn(TPA) are also similar, with the exception of a weight loss event for Co(TPA) ending at 123 °C.

Table 5.1: A table with the beginning, peak, and ending desolvation temperatures and pyrolysis temperatures of terephthalates of Mg, Co, Ni, Cu, and Zn. Also displayed are the mass losses associated with each process and the final residue. All temperatures are in °C and all masses in percent.

		Mg(TPA)	Co(TPA)	Ni(TPA)	Cu(TPA)	Zn(TPA)
Desolvation 1	onset (°C)	153	97	127		
	peak (°C)	180	112	167		
	ending (°C)	201	123	180		
	mass loss (%)	9.843	15.32	16.42		
Desolvation 2	onset (°C)	274	207	202	155	152
	peak (°C)	295	247	232	203	178
	ending (°C)	343	280	262	221	189
	mass loss (%)	18.48	15.12	14.13	24.33	23.28
Degradation	onset (°C)	514	432	391	314	445
	peak (°C)	558	473	414	367	474
	ending (°C)	576	498	432	406	512
	mass loss (%)	44.92	51.33	51.06	49.96	47.43
	residue (%)	26.9	18.33	18.2	25.66	28.52

As described in more detail in the last chapter, there is often clear evidence of the removal of DMF. This is noted by the disappearance of peaks in the same region: around 675, 1105, and 1663 cm^{-1}.

5.2.5 Magnetic susceptibility measurements

The magnetic susceptibilities of Co, Ni and Cu terephthalates were measured as a function of temperature from 4–300 K, as shown in Figures 5.7–5.9. The magnetic susceptibility for Cu(TPA) had been previously reported by Mori [42], and while the structure for Co(TPA) had been previously reported, the magnetic susceptibility had not.

The Curie–Weiss law, $\chi = C/(T-\Theta)$, was used to model the data for both the Co and Ni(TPA)·DMF. In this equation, C is the Curie constant and Θ is the Weiss temperature, proportional to the coupling constant, J. A system obeying the Curie–Weiss law gives a straight line when plotted as $1/\chi = f(T)$. The slope of this line, taken from the linear region, is the inverse of the Curie constant and the intercept is the Weiss temperature. A postive Θ indicates ferromagnetic intermolecular interactions and negative Θ indicates antiferromagnetic interactions. As $\chi T \rightarrow 0$, the deviation from linearity becomes more pronounced. If the curve trends upwards, the interaction is ferromagnetic, if downward, antiferromagnetic [89]. The Co(TPA)·DMF was fitted with Θ = -12.9 K, normally indicative of antiferromagnetic coupling, and the Ni(TPA)·DMF with Θ = 8.8 K, indicating ferromagnetic interaction. The magnetic susceptibility data for Cu(TPA)·DMF, shown in Chapter IV, is shown here again for comparison. The Cu(TPA)·DMF demonstrated antiferromagnetic alignment with a coupling constant of J = –321 cm^{-1}.

5.2.6 Surface Areas

The surface areas of the five different metal terephthalates were measured after desolvation to estimate the extent of porosity in the samples. A bar graph comparing these surface areas is shown in Figure 5.10. The metal terephthalates can be ranked from largest to smallest in terms of surface area after desolvation accordingly: Cu, Zn, Co, Mg, and Ni(TPA).

5.3 Discussion

Figure 5.11 shows the crystal structures that are correlated to the metal terephthalates. The coordination modes of these MOFs, as inferred from the powder diffraction patterns and correlated to

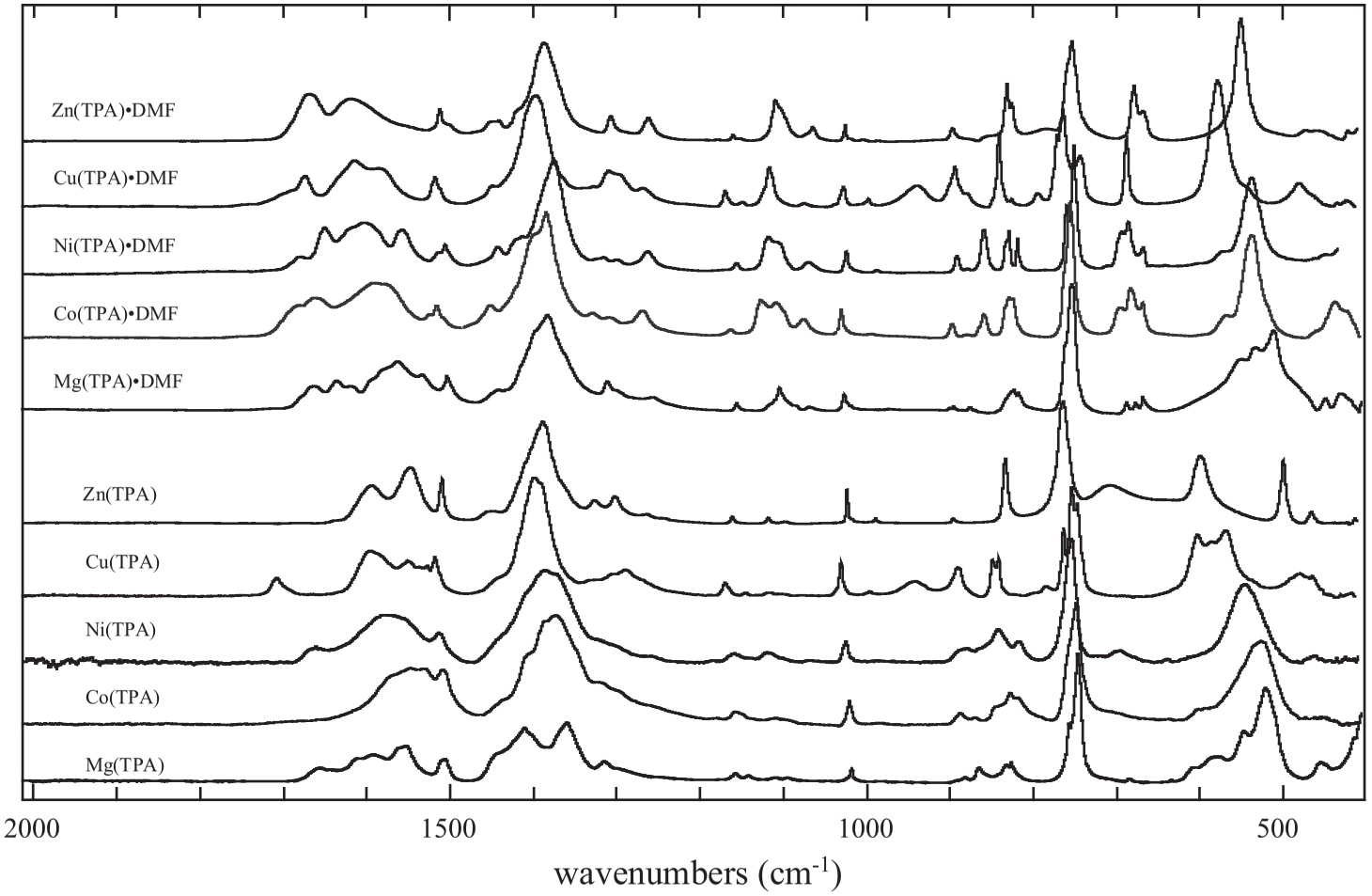

Figure 5.6: The FTIR scans of Zn, Cu, Ni, Co, and Mg terephthalates before and after desolvation.

Table 5.2: A table with the peak locations and assignments of the solvated terephthalates of Mg, Co, Ni, Cu, and Zn.

Mode	DMF [100, 101]	TPA [102]	Mg(TPA)	Co(TPA)	Ni(TPA)	Cu(TPA)	Zn(TPA)
6a		452	448	430		468	466
???			510				
$\omega(COO)_{op}$		525	532	529	532		
16b		564	547	559		565	544
12, free acid		667	667	659	662		
δNCO	659		675	673	680	675	672
4		688	687	685	688		
12, bonded			752	745	744	752	747
12, bonded					753	759	
12, free anion		783			792	782	775
$\delta(COO)_{op}$		813	816	818	812	813	819
ring-breathing		824	822		823	829	824
10a		857		847	852		
11, ν_s(C′N)		882		885	885	882	889
???						927	
17a		964			973	986	
18a		1021	1026	1016	1017	1015	1019
$\delta(CH)_{op}$	1063		1069	1062	1063	1063	1057
???				1095	1101		
$r(CH_3)$	1100		1104	1113	1111	1105	1102
???						1137	
18b		1160	1155	1149	1149	1158	1153
ν_a(NC'), 13	1256	1253	1257	1254	1255	1257	1254
???				1294	1294	1298	1299
14		1320	1311	1313		1316	
$\nu(COO)_{s,op}$		1367	1383	1368	1368	1385	1380
$\delta_s(CH_3)$	1439		1442	1434	1437	1438	1434
19a		1510	1503	1497	1498	1507	1504
$\nu(COO)_{a,ip}$		1550	1564		1550	1573	
$\nu(COO)_{a,op}$		1572	1636	1570	1596	1622	1612
2×823				1643	1643		
ν(CO)DMF	1675		1663	1662	1670	1663	1660

Table 5.3: A table with the peak locations and assignments of the desolvated terephthalates of Mg, Co, Ni, Cu, and Zn.

Mode	TPA [102, 103]	Mg(TPA)	Co(TPA)	Ni(TPA)	Cu(TPA)	Zn(TPA)
6a	452	452		455	468	460
$\omega(COO)_{op}$	530	519	521	540	556	492
16b	564	574				
???		606			590	592
4	688	683		689		701
12	725	745	744	747	741	757
???		755			751	
ring-breathing	824	825	823		829	826
10a	857	831		835	836	
10a		864	865			
11	875	881	883	873	877	889
???					929	
17a	964				984	981
18a	1021	1017	1016	1018	1018	1015
7a	1112	1108	1106	1113	1107	1110
???		1141			1133	
18b	1160	1156	1154	1154	1157	1154
13	1253				1278	1255
???					1294	1294
14	1320	1315	1311		1320	1319
$\nu(COO)_{s,op}$	1367	1360	1369	1379	1387	1380
$\nu(COO)_{s,ip}$	1413	1410				
19a	1510	1506	1506	1506	1507	1502
$\nu(COO)_{a,ip}$	1550	1553	1528	1571	1539	1540
$\nu(COO)_{a,op}$	1572	1592	1544	1604	1584	1586
???		1656		1662	1695	

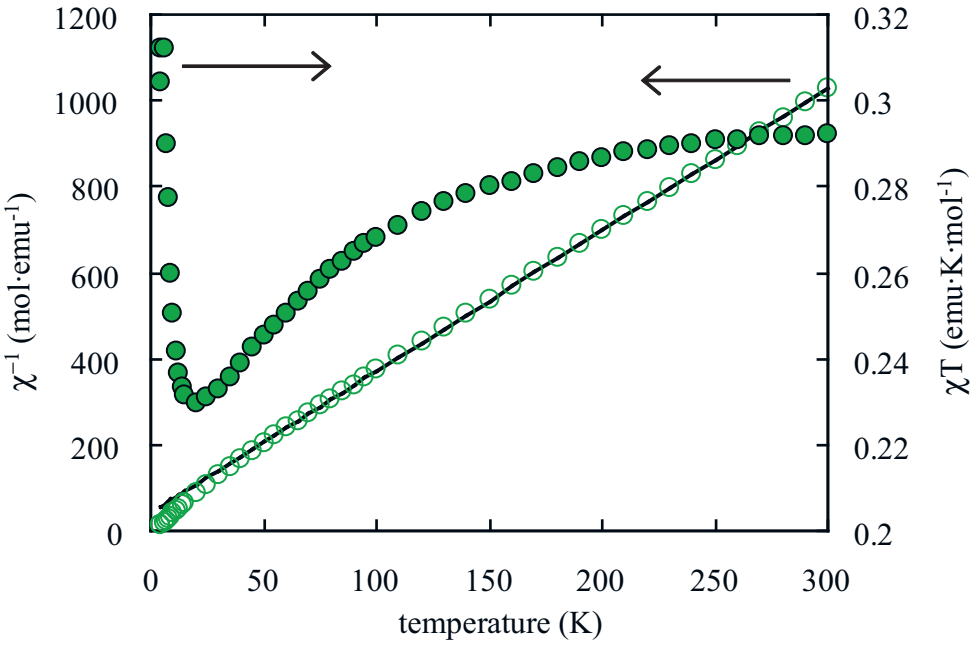

Figure 5.7: Plots of $1/\chi$ and χT versus T for Co(TPA) are shown, indicating paramagnetic behavior with a weak antiferromagnetic component.

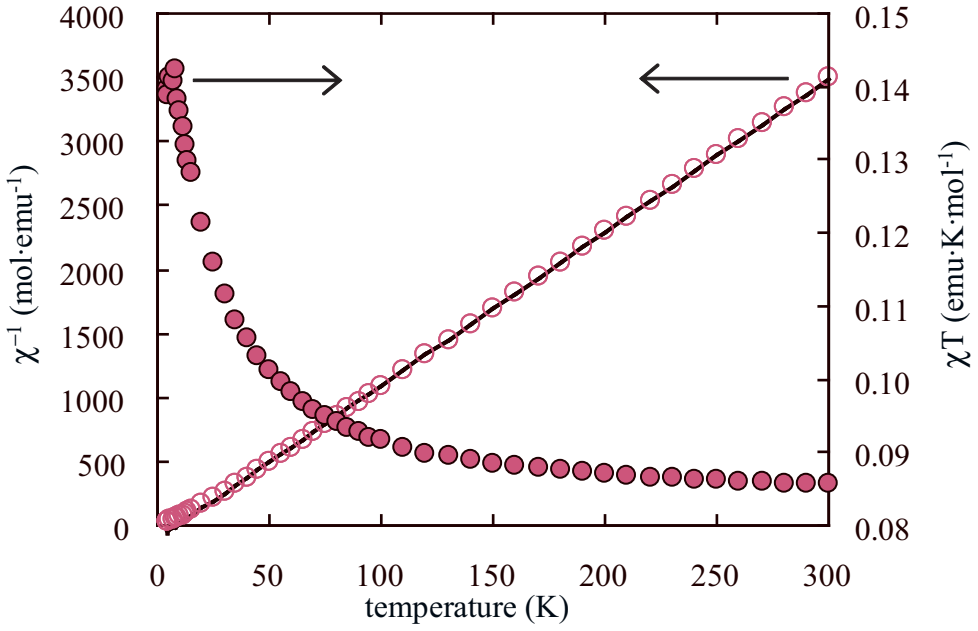

Figure 5.8: Plots of $1/\chi$ and χT versus T for Ni(TPA) are shown, indicating paramagnetic behavior with a weak ferromagnetic component.

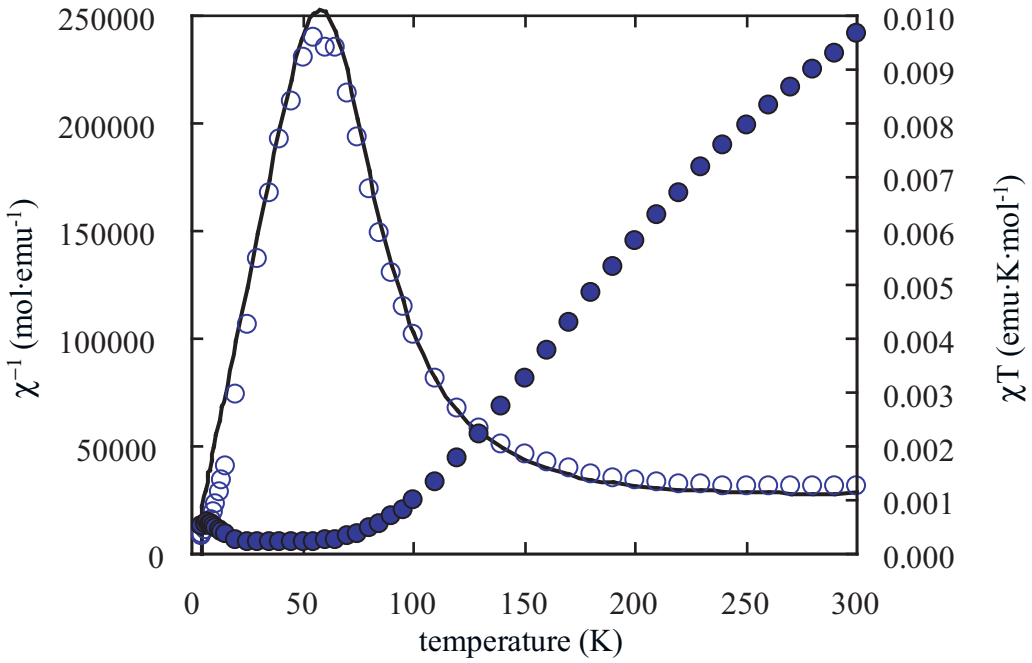

Figure 5.9: Plots of $1/\chi$ and χT versus T for Cu(TPA) are shown indicating antiferromagnetic behavior with a weak paramagnetic impurity.

published structures, can be grouped roughly into three categories. Mg(TPA) and Ni(TPA) both display a mixture of bridge bonding and chelate bonding. These appear to form sheets that are three metal atoms thick, separated and intercalated by solvent molecules.

The Co(TPA) forms a three-dimensional structure that has bonding between adjacent metal atoms through the DMF and through the carboxylate ligand O atoms in one dimension and across the terephthalate ligand in the other two. The Cu(TPA) and Zn(TPA) both form "paddlewheel" structures, where two metal atoms in a dimer share are bonded to the same four terephthalate ligands with a DMF at the apical position.

The electron density around the metal center also appears to play a role in determining the IR absorbances of the solid prior to desolvation. As shown in Figures 5.12 and 5.13, the red-shift in the DMF correlated peak is accompanied by a blue-shift in the TPA correlated peak. As shown by the error bars, This trend is still apparent even when the peak-widths at FWHM are accounted for. When comparing the $\nu(COO)_s$ and the $r(CH_3)$ modes and the 19a and the $r(CH_3)$ modes, a clear difference is seen between two groups. The Mg, Zn, and Cu terephthalates occupy the upper left-hand corner,

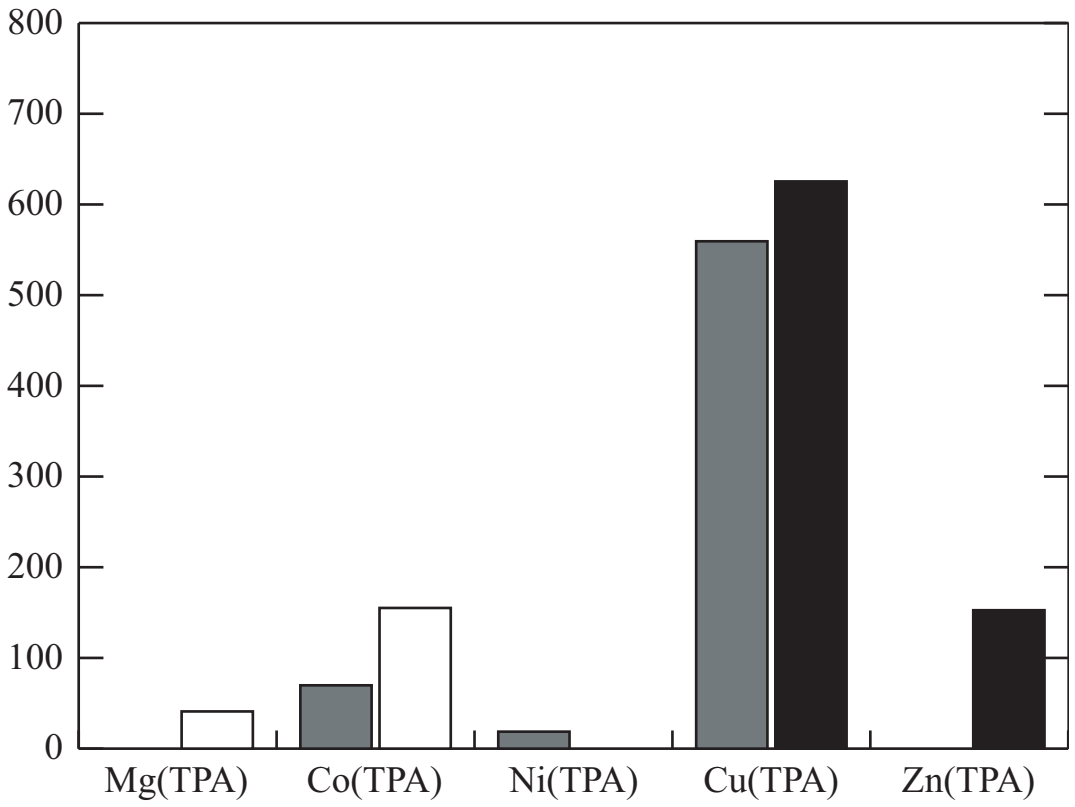

Figure 5.10: The surface areas of Mg, Co, Ni, Cu, and Zn terephthalates after desolvation are shown. The clear, grey, and black series correspond to measurements taken on the correspond Gemini V, Beckmann–Coulter SA-3100, and the Micromeritics ASAP 2020, respectively. The Mg, Ni, and Zn(TPA) were only measured on one machine.

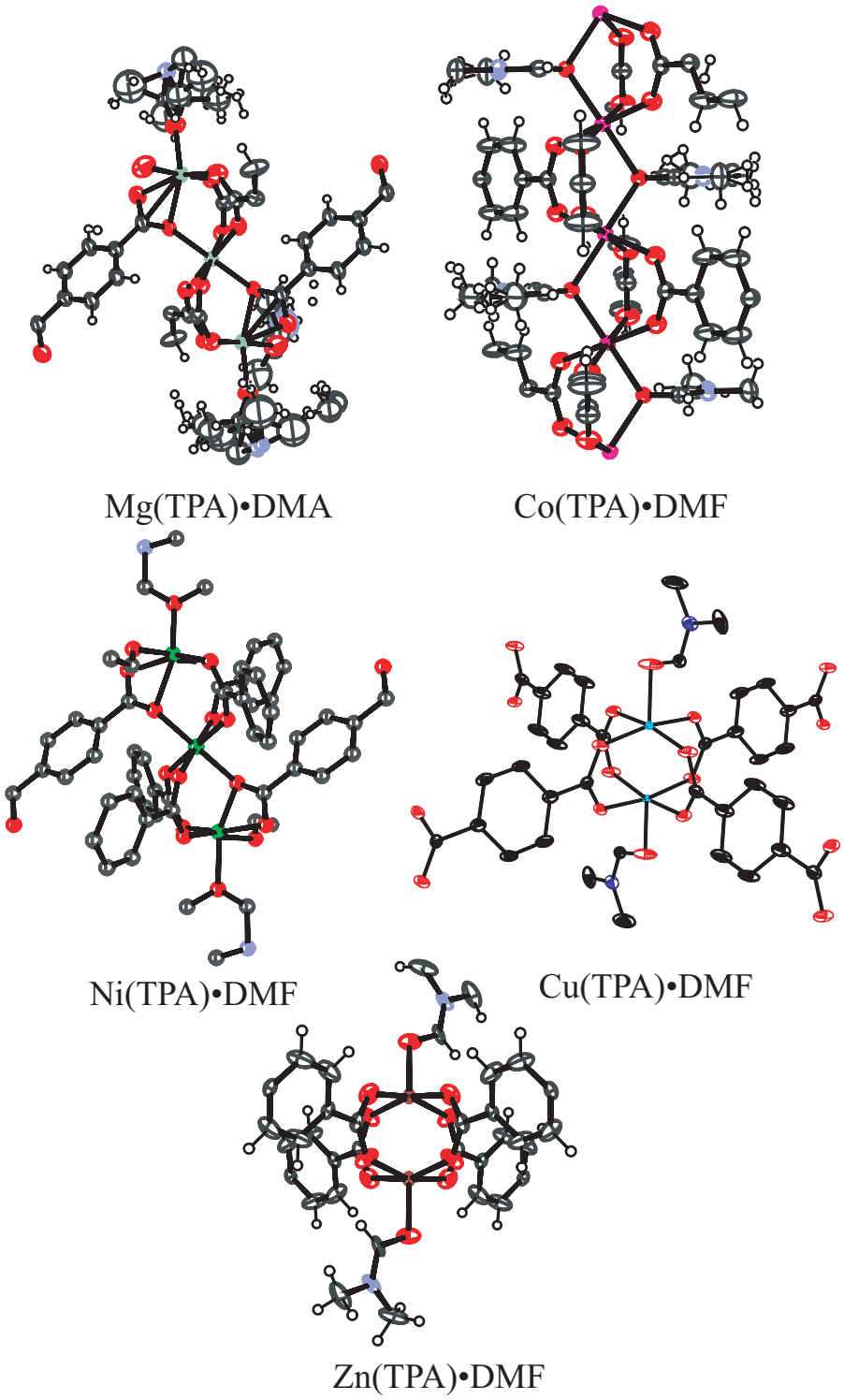

Figure 5.11: The crystal structures of Mg, Co, Ni, Cu, and Zn terephthalates with the coordinated DMF groups (DMA for Mg(TPA)) [45, 98, 99]. Note the similarity between the Ni(TPA)·DMF and Mg(TPA)·DMA, as well as the similarity between Zn(TPA)·DMF and Cu(TPA)·DMF.

displaying a red-shifted $r(CH_3)$ absorbance and a blue-shifted $\nu(COO)_s$ absorbance. By contrast, the Ni and Co terephthalates occupy the lower right-hand corner, displaying a blue-shifted $r(CH_3)$ absorbance and a red-shifted $\nu(COO)_s$.

The segregation between these two groups is attributed to the electron density in the *d* and *d** orbitals. The Mg center, having only an *s* shell can accept no electron density into its *d* orbitals because it has none. This results in very little blue-shifting from the un-coordinated value of 1100 cm^{-1} for the $r(CH_3)$. On the other hand, the lack of *d*-associated t_{2g} orbitals leaves very little electron density to interfere with the $\nu(COO)_s$ absorbance. Similarly, Zn, with a full complement of *d* orbitals, cannot accept any electron density from the DMF, so the presence or absence of the ligand cannot affect the location of the $\nu(COO)_s$ peak. The Cu center, lacking the closed shell of Zn does accept some electron density from the DMF, blue-shifting the DMF-associated $r(CH_3)$ slightly to 1105 cm^{-1}. However, the DMF is unable to destabilize the t_{2g} orbitals and the $\nu(COO)_s$ peak remains blue-shifted. It is only in the presence of a Ni(II) center that the electron density is low enough that the presence of the DMF begins to donate enough electron density to the e_g orbitals on the Ni center that the t_{2g} orbitals become destabilized. This has the effect of causing them to swell and crowding out the O atoms in the carboxylate group. This results in a blue-shifting of the $r(CH_3)$ absorbance, owing to the decreased electron density on the ligand, and a red-shifting of the $\nu(COO)_s$ peak owing to the steric crowding of the t_{2g} orbitals displacing the associated O atoms in the carboxylate groups. These trends were even more clear when substituting the DMF–associated $\nu(CO)$ for the $r(CH_3)$. Such a graph was not presented because the average FWHM of this peak was so broad that likelihood of a trend would be questionable.

These trends can also be seen in the TGA data, where the IR absorbance, and the corresponding energy, seem to indicate the relative thermal stability of a given bond. Figure 5.14 shows the relationship between the $\nu(COO)_s$ after thermal desolvation and pyrolysis temperature. The error bars on the *y*–axis indicate the locations of the FWHM of the IR peaks, and the error bars on the *x*–axis indicate the temperatures that the process begins and ends at. Although the IR peaks are broad in comparison to the difference in peak location, the correlation indicates that the red-shifted $\nu(COO)_s$ in the metal-carboxylate bond leads to lower pyrolysis temperatures. This may be because there is additional electron density in the carboxylate group, red-shifting the $\nu(COO)_s$ while causing a

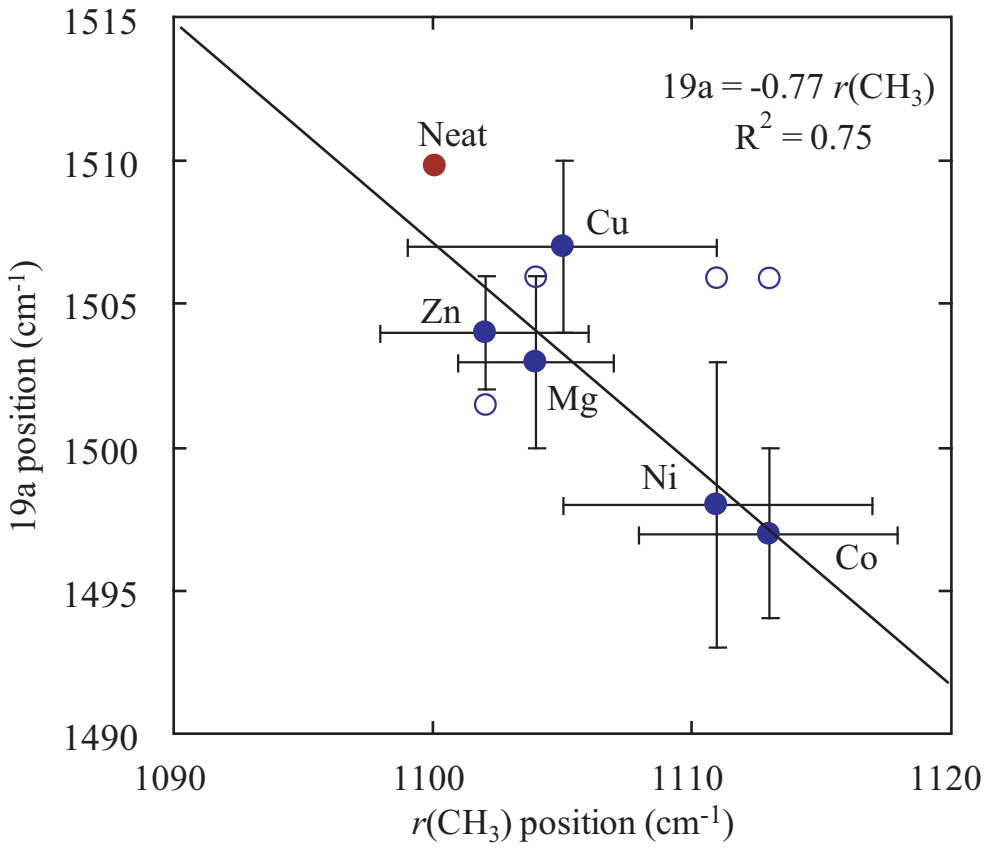

Figure 5.12: The filled circles correspond to the intersection of the 19a mode on the TPA ligand and the $r(CH_3)$ mode on the DMF. The negative correlation indicates that the blue-shifted $r(CH_3)$ results in a red-shifted phenyl 19a mode. Thus the the metal center accepts electron density from the solvent DMF and passes it onto the benzene ring in the terephthalate ligand. The clear circles denote the locations of the generally higher 19a peaks after desolvation, with Cu(TPA) remaining unchanged. The data-point "neat" indicates the locations of the peaks in the absence of a metal center. The error bars correspond to the FWHM of the respective peak.

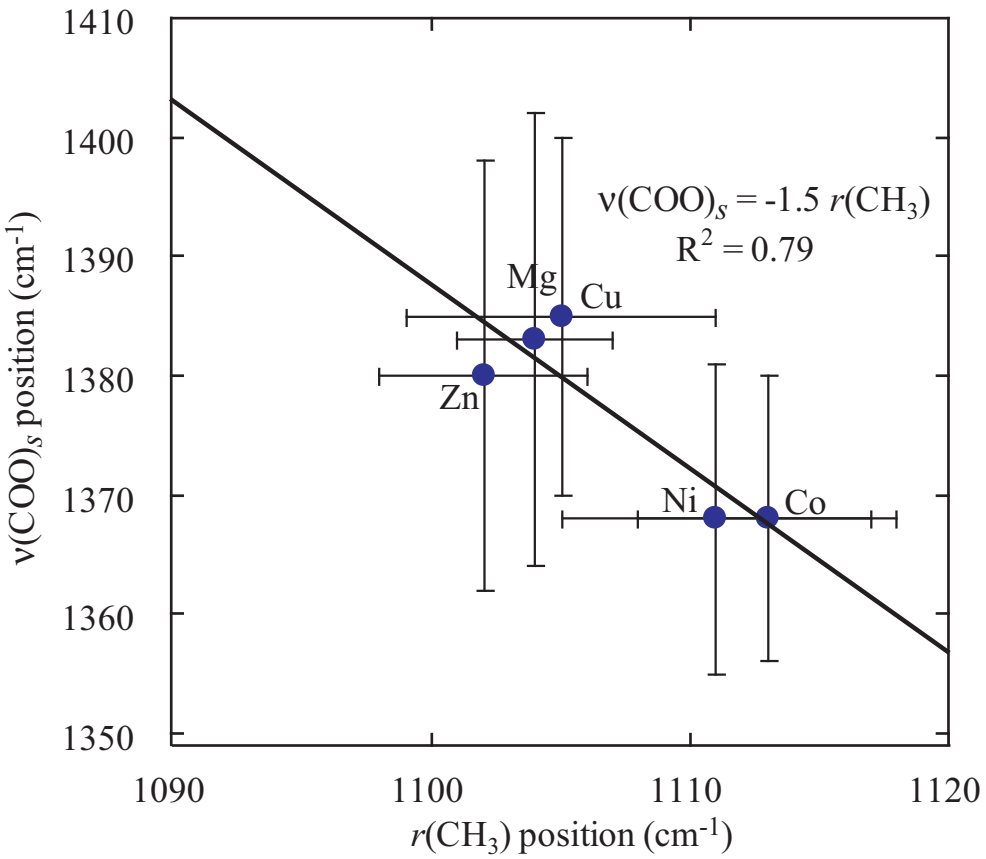

Figure 5.13: The correlation between the $\nu(COO)_s$ and the $r(CH_3)$ modes indicates that the electron density that the metal center accepts from the solvent is taken up by the carboxylate functional group. Thus the blue-shifted $r(CH_3)$ results in a red-shifted bond in the $\nu(COO)_s$. The error bars correspond to the FWHM of the respective peak.

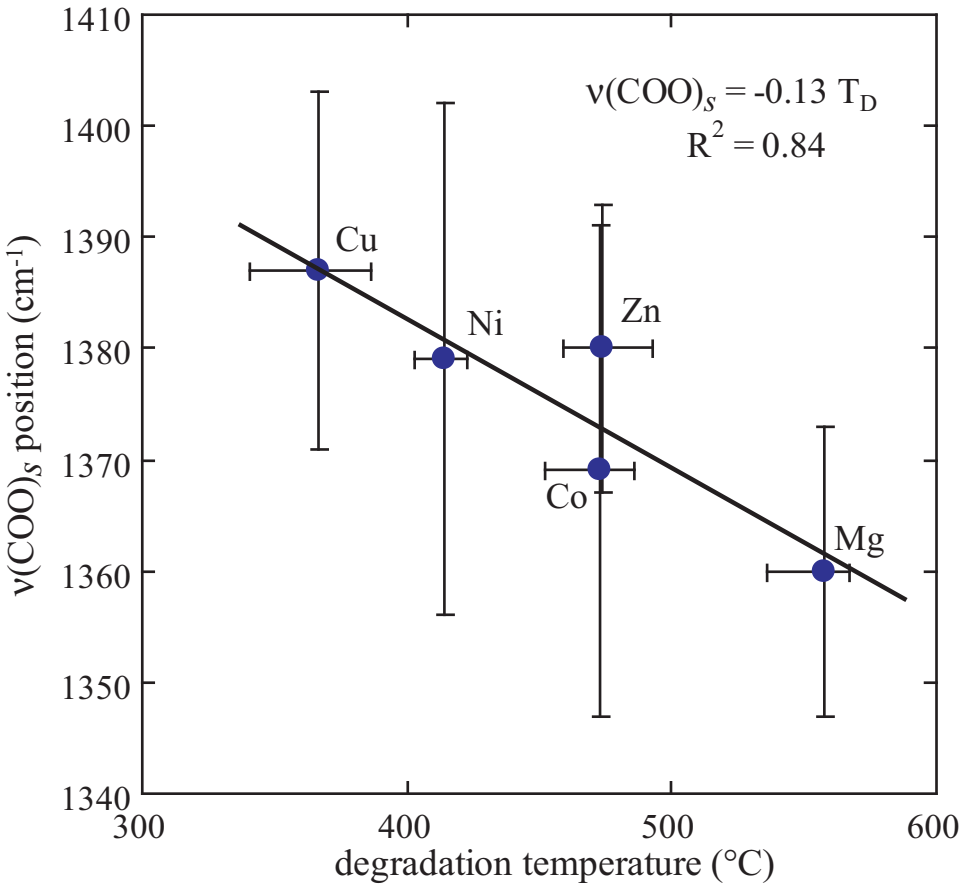

Figure 5.14: The pyrolysis temperatures of Mg Co, Ni, Cu, and Zn terephthalates are shown as a function of the location of the $\nu(COO)_s$ modes in the IR spectra. This graph indicates that the more electron density that the metal center can accept, from the carboxylic functional group, the higher the $\nu(COO)_s$, resulting in increased thermal stability.

greater coulombic attraction between the carboxylate group and the metal center. This increased coulombic attraction results in greater thermal stability and higher pyrolysis temperatures.

The change in desolvation temperatures can also be related to the IR peak positions. Figure 5.15 shows the $r(CH_3)$ absorbance as a function of the desolvation temperature, as estimated from the TGA curves. As the donation from the DMF to the metal center increases and the gets $r(CH_3)$ blue-shifted accordingly, it becomes harder to thermally desolvate the DMF from the metal center. The Cu center appears to avoid pushing away the carboxylate anions like Ni and Co. This is attributed to the strong antiferromagnetic spin coupling between adjacent Cu ions in the same dimer, as compared to the Ni and Co couplings in Figures 5.7 - 5.9. The higher spin results in smaller *d* orbitals and a shorter M-O distance.

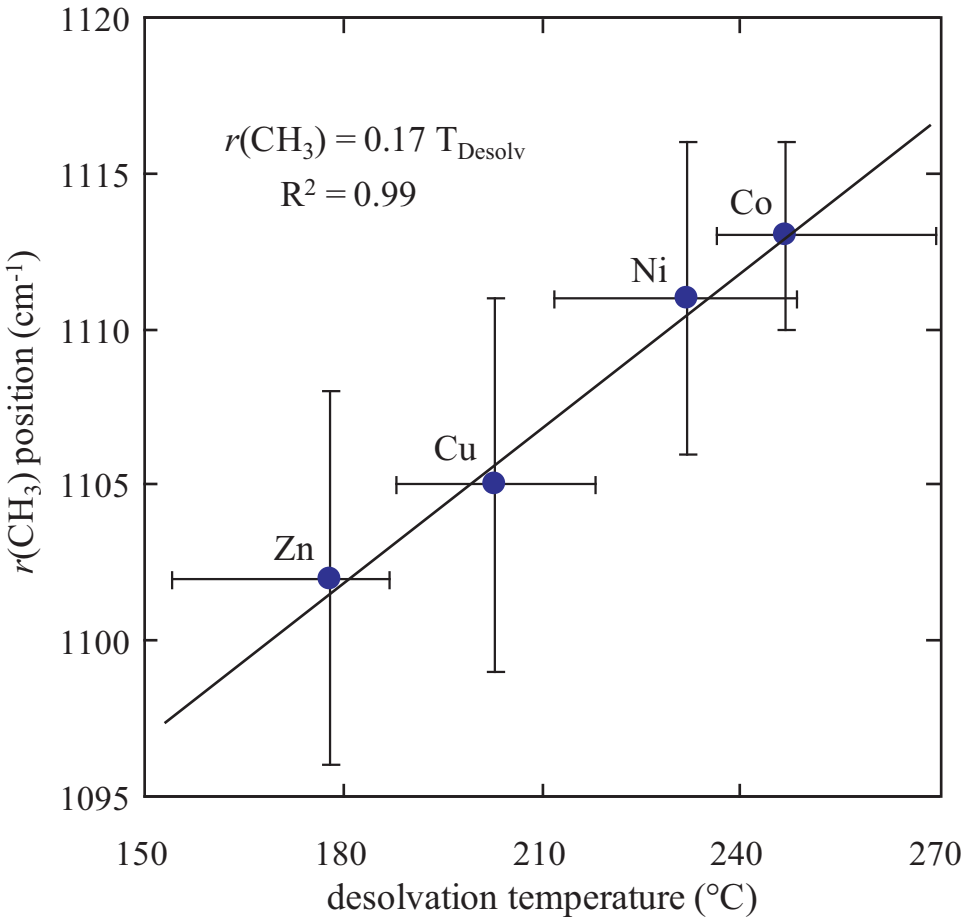

Figure 5.15: The variation in the DMF $r(CH_3)$ is shown as a function of desolvation temperature for Co, Ni, Cu, and Zn(TPA)·DMF. This indicates that the methyl groups on the DMF are sensitive to the electron donating C=O group. Thus as the metal center is able to receive more electron density from the DMF, the greater the thermal stability of that bond and the higher the temperatures needed to desolvate the material.

5.4 Conclusions

The thermal, vibrational, and magnetic properties of the terephthalates of Mg, Co, Ni, Cu, and Zn have been measured and compared. From these comparisons, relationships have been drawn between the thermal and vibrational properties. The thermal stability of the metal terephthalates appears to be related to the electronic configuration of the metal center, rather than the crystal structure of the solid. The magnetic susceptibility measurements reveal that Ni(TPA)·DMF and Co(TPA)·DMF have paramagnetic behavior with weakly ferromagnetic and antiferromagnetic susceptibilities respectively.

While the structure of the Ni(TPA) alone has not been solved, a partial solution was found to the heterometal organic framework, $Ni_{0.97}Cu_{0.03}$(TPA)·DMF. It is shown that the powder diffraction pattern predicted by this solution closely matches the experimental powder pattern of Ni(TPA). This suggests that $Ni_{0.97}Cu_{0.03}$(TPA)·DMF may be forming a dilute molecular magnet that may be ferrimagnetic.

It is noted that the Zn(TPA)·DMF and Cu(TPA)·DMF structures share many of the same features, including the paddlewheel coordination and similar metal-oxygen bond strengths. The heterometal organic framework resulting from the combination of these two materials is the theme of the next chapter.

CHAPTER VI

ZINC COPPER TEREPHTHALATE

6.1 Introduction

Although the literature for heterobimetallic carboxylates is scant for recently developed MOFs, it is more abundant for monomeric systems, dating back to work with $(Cu,M(II))(HCOO)_2 \cdot 2H_2O$ [104, 105]. This type of study was also carried out more recently on $Cu_{0.06}Zn_{0.94}(C_4O_4H_2)\cdot 2H_2O$ as a precursor to a ZnO/CuO catalyst for methanol synthesis [106]. To our knowledge, these studies have not been applied to MOF systems, and so this poses an opportunity to see if the same conclusions can be drawn for macromolecular systems.

We selected as a starting point the adduct of Zn(TPA) in dimethylformamide (DMF). Much of the interest in MOF field began with the discovery of open porosity in MOF-2, a polymorph of Zn(TPA) [41]. Subsequently, a number of different polymorphs of Zn(TPA) have been reported in the literature [43–45,107]. Although the isostructural Cu(TPA)·MeOH was discovered before MOF-2 [42], the crystal structure was unpublished at the start of the research in this thesis. After solving the crystal structure for Cu(TPA)·DMF [88], we discovered that Clausen reported that Zn(TPA) has a polymorph with similar lattice parameters in the C*2/m* space group, forming square grid-like lamellar sheets with Zn(II) dimers or Cu(II) dimers connecting terephthalate linkers, referred to here as MOF-C*2/m* [45]. The similarity between the structures would appear to be a natural product of their adjacency in the periodic table and the ensuing cation size. Whereas in MOF-2, the cation coordinates water at the apical site, in Cu(TPA)·DMF and MOF-C*2/m*, the cation coordinates a DMF molecule at the apical site. The differences in crystal structure are principally a product of the cation and the identity of the coordinated solvent. The consequence of this observation is to ask what the effect of composition is on the structure shared between MOF-2 and Cu(TPA)·DMF. Since the structure for Cu(TPA)·DMF was only recently published [88], we could find no report of the effect of composition on a heterobimetallic Zn-Cu terephthalate. The primary objective then of this study is to measure the effect of metal salt composition on the physical and electronic properties of a

copper zinc heterobimetallic terephthalate framework. The secondary objective is then to determine the extent to which copper and zinc are able to exist within the same dimer in the copper-zinc framework.

6.2 Results

6.2.1 Microscopy

This study was inspired by some preliminary studies on the effect of impurity ions on the crystal structure of Zn(TPA)·DMF. A small amount of copper nitrate added to a DMF solution of zinc nitrate and terephthalic acid produced crystals, like the ones shown in Figure 6.1. These crystals had managed self-organize into a core-shell structure, with the copper apparently trapped in the Zn(TPA)·DMF matrix.We then endeavored to carry out the same experiment on the entire range of composition between Cu and Zn. SEM images of two of the synthesized specimens are shown in Figure 6.2. As is immediately apparent, the presence of a small amount of Cu in a synthesis of Zn(TPA)·DMF can alter the crystallization of the resulting solid. In the absence of Cu, the Zn(TPA)·DMF has a tendency to form large sheets, up to a millimeter across. However, the presence of a small amount of Cu virtually quenches this process, forming crystallites with little aspect ratio that are 100–200 μm in across.

6.2.2 X-ray Powder Diffraction

X-ray diffraction experiments were also carried out to determine the identity and relative quantities of the products. The traces from those scans are shown in Figure 6.3. The peaks in the powder diffraction scans were compared against the predicted peaks from a number of MOF-2 polymorphs in the literature. We were able to reference most of the peaks to MOF-2, MOF-C*2/m*, and Cu(TPA)·DMF. The same analysis was carried out on the samples after desolvation at 230 °C. The corresponding powder diffraction traces are shown in Figure 6.4. The identification of the resulting phases has not been previously reported and remains outside the scope of this study. However, the peaks in the powder diffraction traces of the desolvated material could be unambiguously assigned to the Cu and Zn related phases.

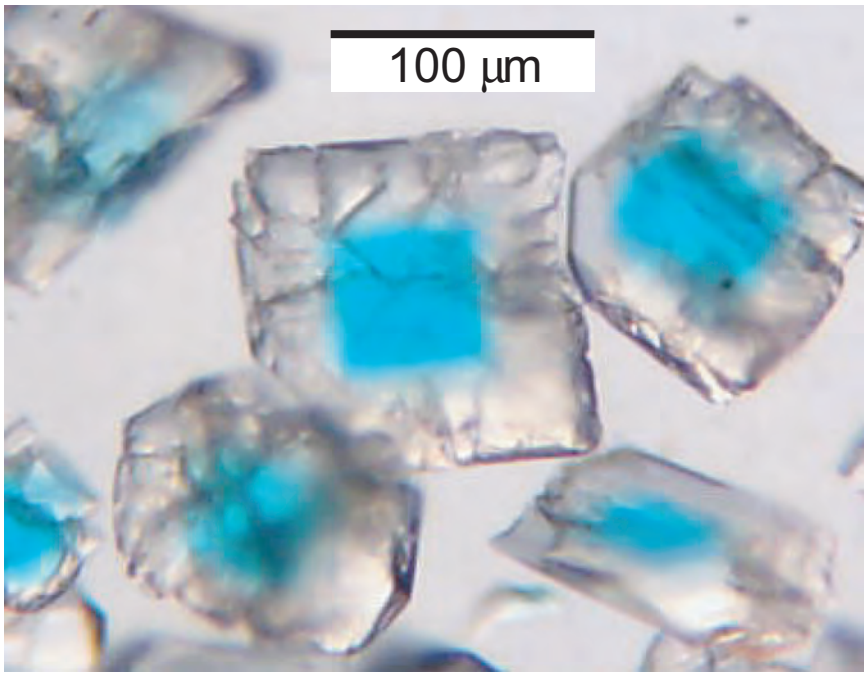

Figure 6.1: A micrograph is shown of a sample of $Zn_{0.97}Cu_{0.03}$(TPA)·DMF. Notice the blue square apparent in the clear crystals. The blue square is attributed to a high Cu content region that forms during crystallization.

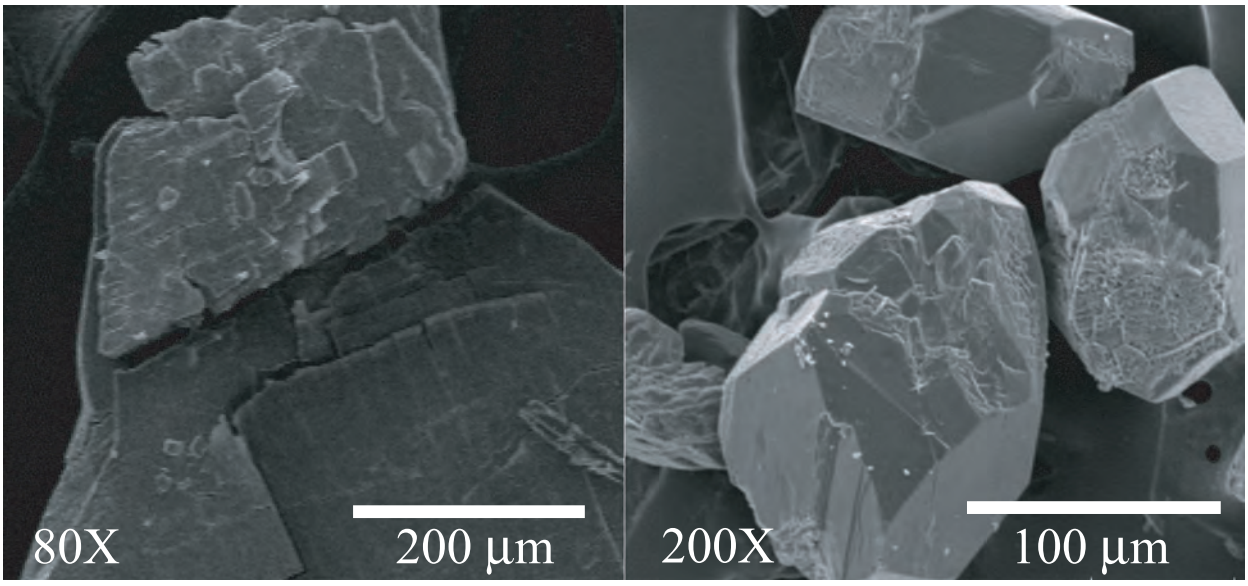

Figure 6.2: The figure shows SEM images of pure Zn(TPA)·DMF (on the left) and $Zn_{0.99}Cu_{0.01}$(TPA)·DMF (on the right). Notice how the presence of Cu at a 1% concentration in the intial salt drastically affects the morphology of the resulting product crystal. No large sheets were found for the $Zn_{0.99}Cu_{0.01}$(TPA)·DMF, indicating that the presence of Cu drastically alters the nucleation during crystallization, preventing the formation of plate-like Zn(TPA)·DMF.

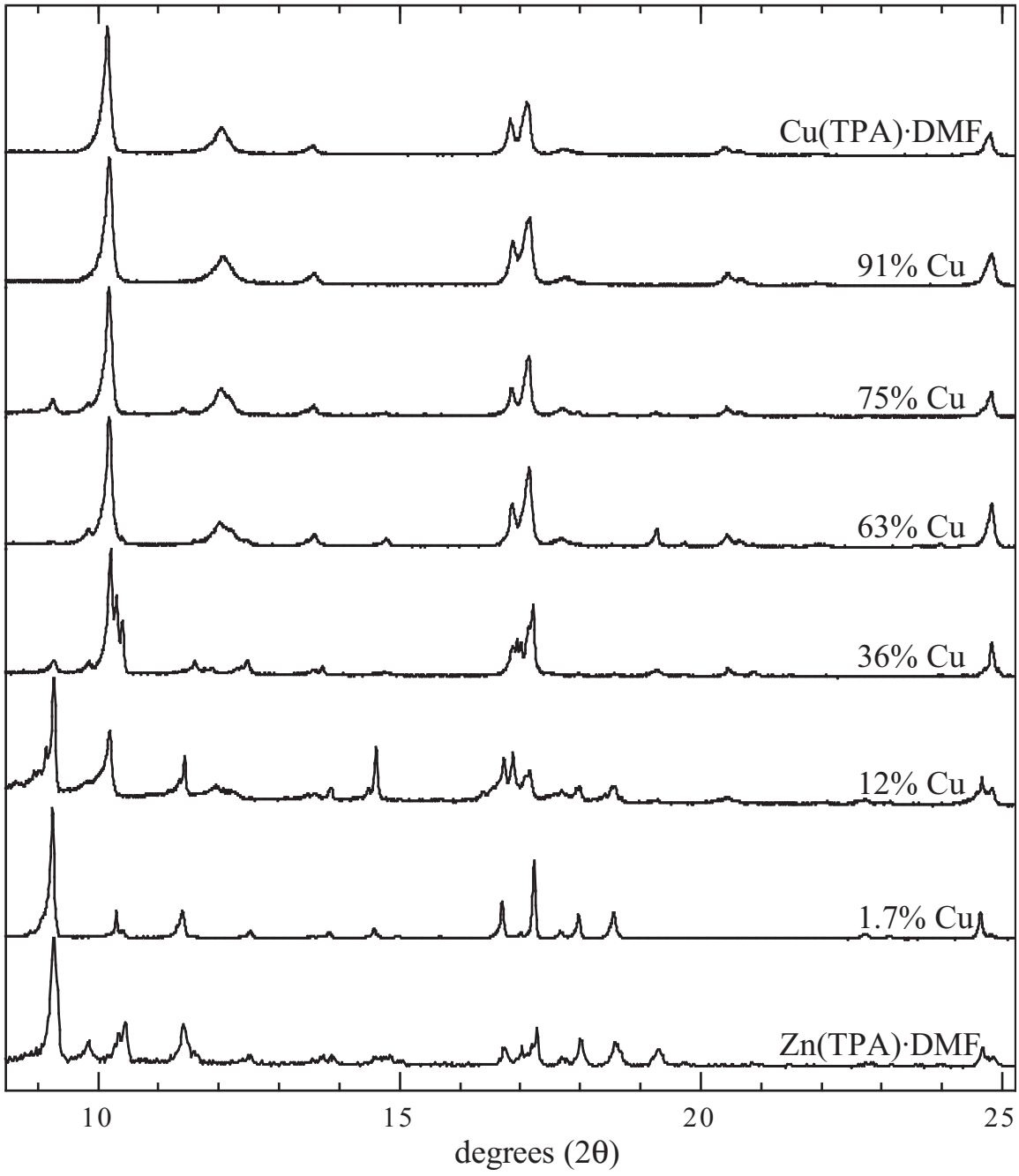

Figure 6.3: The X-ray powder diffraction scans of Zn-Cu(TPA)·DMF prior to desolvation are shown for 0, 1.7, 12, 36, 63, 75, 91, and 100% Cu. The phases present correspond to MOF-2, MOF-C2/*m*, and Cu(TPA)·DMF.

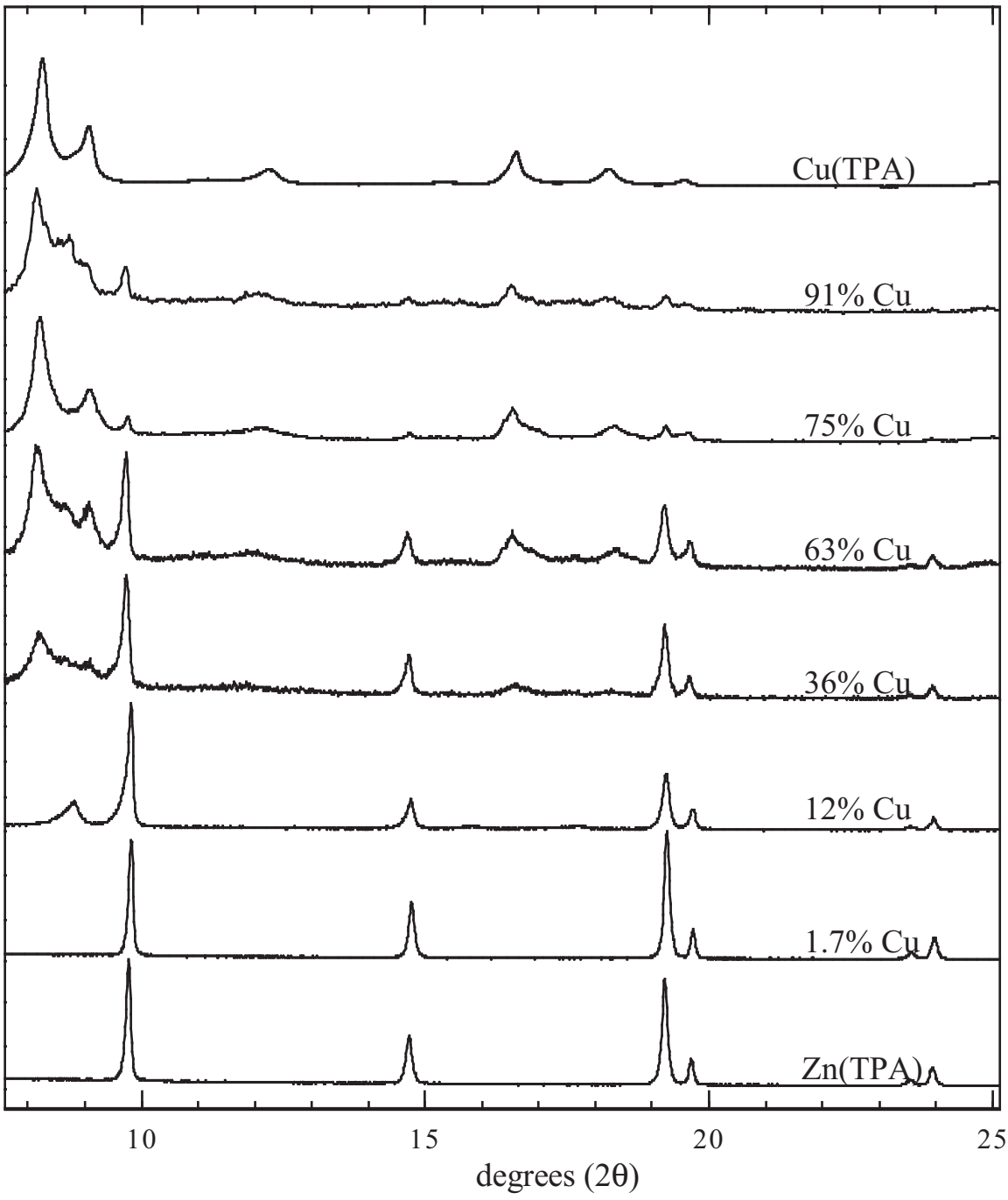

Figure 6.4: The X-ray powder diffraction scans of Zn-Cu terephthalates after desolvation are shown for 0, 1.7, 12, 36, 63, 75, 91, and 100% Cu in scans 1 through 8 respectively. There are only two phases present: Zn(TPA) and Cu(TPA).

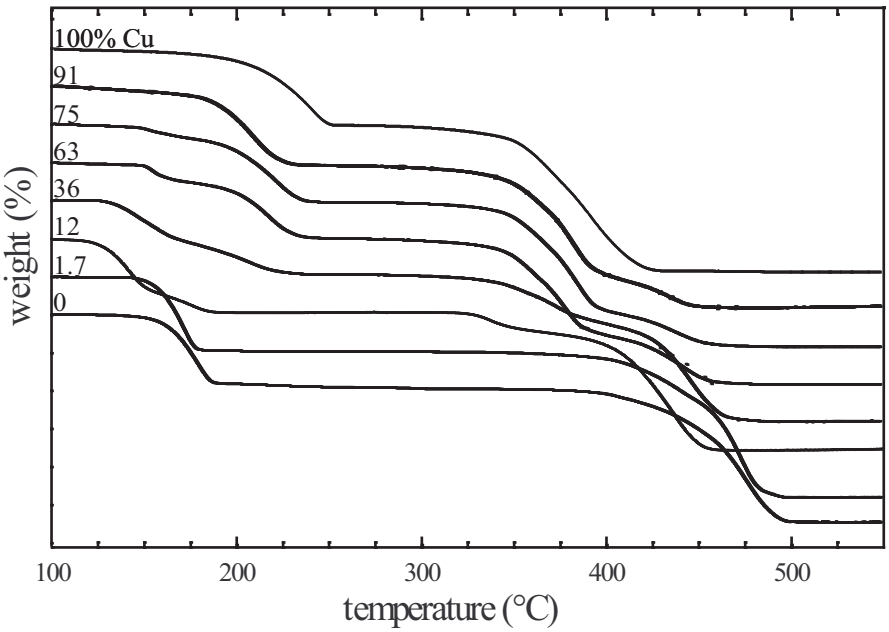

Figure 6.5: Thermogravimetric traces for Zn-Cu terephthalates with 0, 1.7, 12, 36, 63, 75, 91, and 100% Cu are shown.

6.2.3 Thermogravimetric Analysis

Thermogravimetric analyses (TGA) were used to investigate the effect of Zn-Cu composition on the thermal desolvation and degradation of the resulting powders. Figure 6.5 shows the effect of composition on the thermal degradation temperatures. The figure shows how, as the Cu content increases, the desolvation temperature increases and the degradation temperature decreases. Because of the similarity between the structures of the different compositions, the TGA traces from the resulting powders had weight loss regimes that overlapped, making the contributions from the respective weight loss events difficult to judge. However, by taking the derivative of the weight-loss curve with respect to temperature and deconvoluting the overlapped peaks, the contributions from different weight-loss events could be calculated and compared across other samples of different compositions. Figure 6.6 shows the TGA trace for the 63% Cu sample, along with the associated derivative curve and the fitted peaks used to estimate relative contributions from each process. While this process was useful for estimating the relative contributions from overlapped thermal degradation processes, it did not take into account mass-losses outside the peak area. Therefore, there may be minor discrepancies between calculated and actual residues.

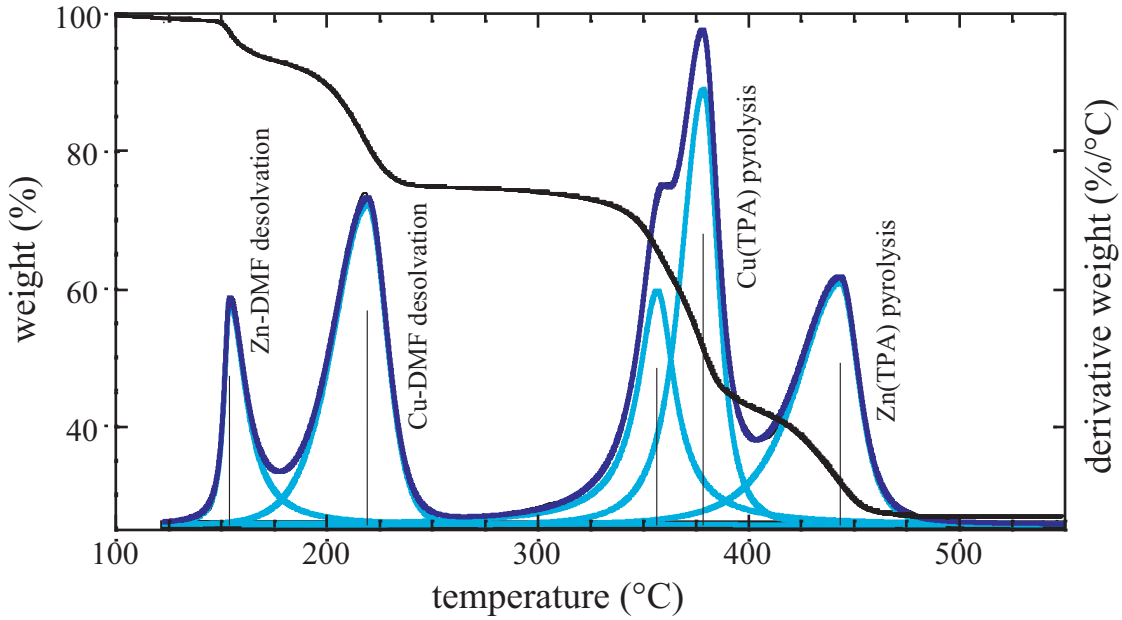

Figure 6.6: The thermogravimetric trace for the 63% Cu is shown with the accompanying derivative curve and the peaks used to estimate the relative contributions from each thermal degradation process.

6.2.4 Porosity and surface area

Figure 6.7 shows the surface areas measured for 0, 1.7, 12, 36, 63, 91 and 100% Cu. The surface area of the desolvated samples was measured with the N_2 BET method to examine the effect of metal salt composition on the resulting surface area. These measurements could only be collected over a period of months after the initial synthesis, but are found to remain consistent.

6.2.5 Infrared spectroscopy

The vibrational properties of the Zn-Cu terephthalates were measured with infra-red spectroscopy. To avoid looking at the effect of solvent in the lattice, these measurements were carried out on powders that had already been desolvated, as evidenced by TGA traces. An attenuated total reflectance (ATR) accessory was used to record the spectra. This ensured that each specimen would have roughly the same absorbance. The relative amplitudes of the spectra were then normalized to the 18a peak around 1018 cm^{-1}, as the location and shape of this peak remained relatively unchanged between specimens. These spectra are shown in Figure 6.8 along with the IR peak locations listed in Table 6.1. From them, the extent to which the framework is behaving like Zn(TPA) or Cu(TPA)

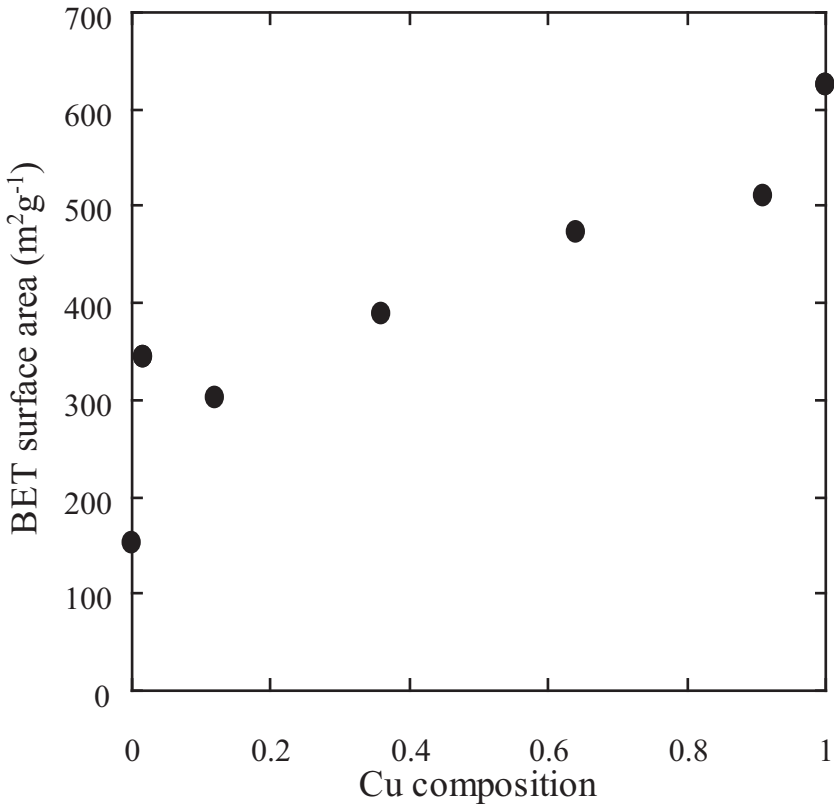

Figure 6.7: The BET surface area is plotted against Cu concentration plotted for the Zn-Cu terephthalates at 0, 1.7, 12, 36, 63, 91, and 100% Cu. The data indicates that a small amount of Cu has the effect of drastically increasing the surface area, and that the behavior thereafter is mostly linear. It also appears that adding a small amount of Zn to a Cu-rich terephthlate has the effect of disproportionately lowering the surface area of the resulting heterometallic terephthalate.

Table 6.1: A table with the IR peak locations and assignments of the desolvated Cu and Zn terephthalates.

Mode	0	1.7	12	36	63	75	91	100 %Cu
6a	460	460	458	457	453	456	453	468
ω(COO),op	492	493	493	493	493			
ω(COO),op				503		504		
ω(COO),op				555	555	555	555	556
???	592	592	583	584	588	586	588	590
4	701	701	701					
12			736	735	735	735	735	735
12			746	743	742	742	742	741
12	757	757	751	751	751	751	751	751
ring-breathing	826	826	826	828	828	829	829	829
10a				837	836	836	838	836
11			882	881	877	879	876	877
11	889	888	888	889	881	880	880	880
???			931	932	931	932	938	929
18a	1015	1015	1016	1917	1018	1018	1019	1018
7a	1111	1111	1110	1110	1109	1108	1108	1107
???		1137	1136	1133	1133	1133	1133	1133
18b	1154	1153	1154	1157	1158	1157	1159	1158
13				1279	1279	1279	1279	1278
???	1294	1294	1294	1296	1293	1294	1294	1294
14	1320	1319	1319	1320	1318	1318	1321	1319
ν(COO)s,o	1380	1381	1380	1388	1387	1388	1390	1387
19b		1439	1439	1439	1439	1439	1439	1439
19a	1502	1502	1502	1506	1506	1506	1506	1507
ν(COO)a,i	1540	1540	1539	1531	1544	1540	1539	1539
ν(COO)a,o	1585	1585	1573	1589	1589	1588	1590	1584
???			1694	1697	1697	1697	1697	1695

can be estimated from the relative peak intensities.

6.2.6 Magnetic susceptibility

A graph showing χT versus T for all of the Zn-Cu terephthalates after desolvation is shown in Figure 6.9. Because of the similarity of the size and coordination of the Zn and Cu ions in the terephthalate framework, it was not possible to isolate the extent to which a Cu center would prefer to dimerize with Zn instead of Cu. This we term “heterometallic dimerization”. We examined the extent of heterometallic dimerization by measuring the magnetic susceptibilities as a function of temperature for the Zn–Cu terephthalates. By modeling the response as a linear function with antiferromagnetic

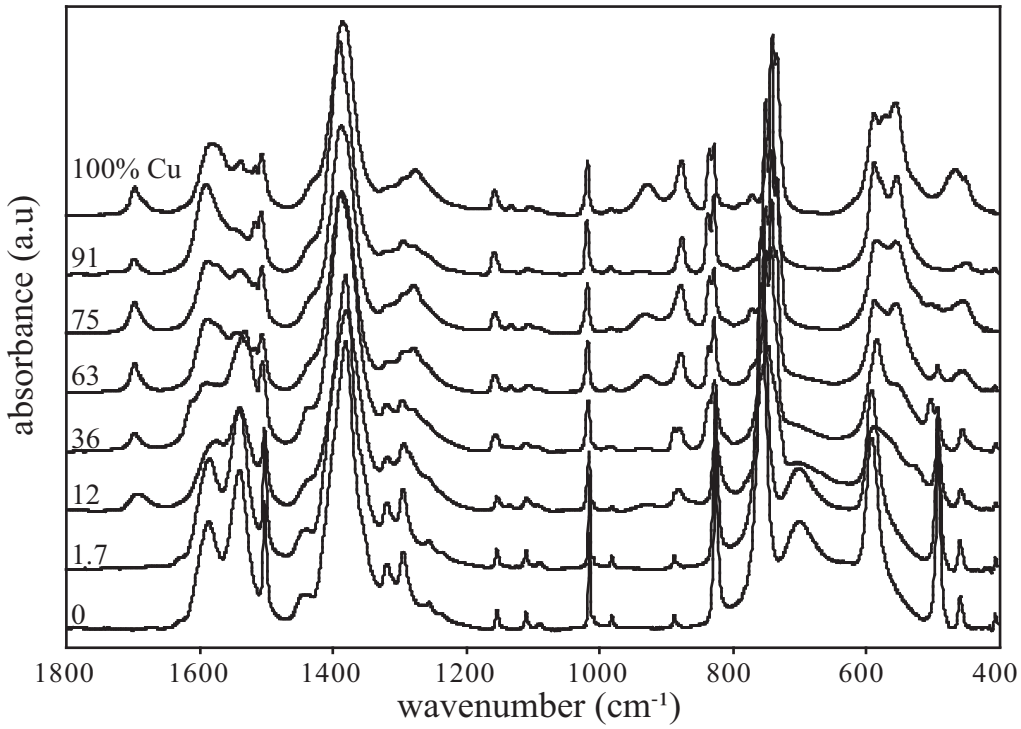

Figure 6.8: Infrared spectra are shown for the desolvated Zn-Cu terephthalates at 0, 1.7, 12, 36, 63, 75, 91, and 100% Cu. Although the two frameworks share many of the same features in the IR spectrum, prominent differences include the absorbances at 492 and 701 cm^{-1} for Zn(TPA), and 929 and 1695 cm^{-1} for Cu(TPA).

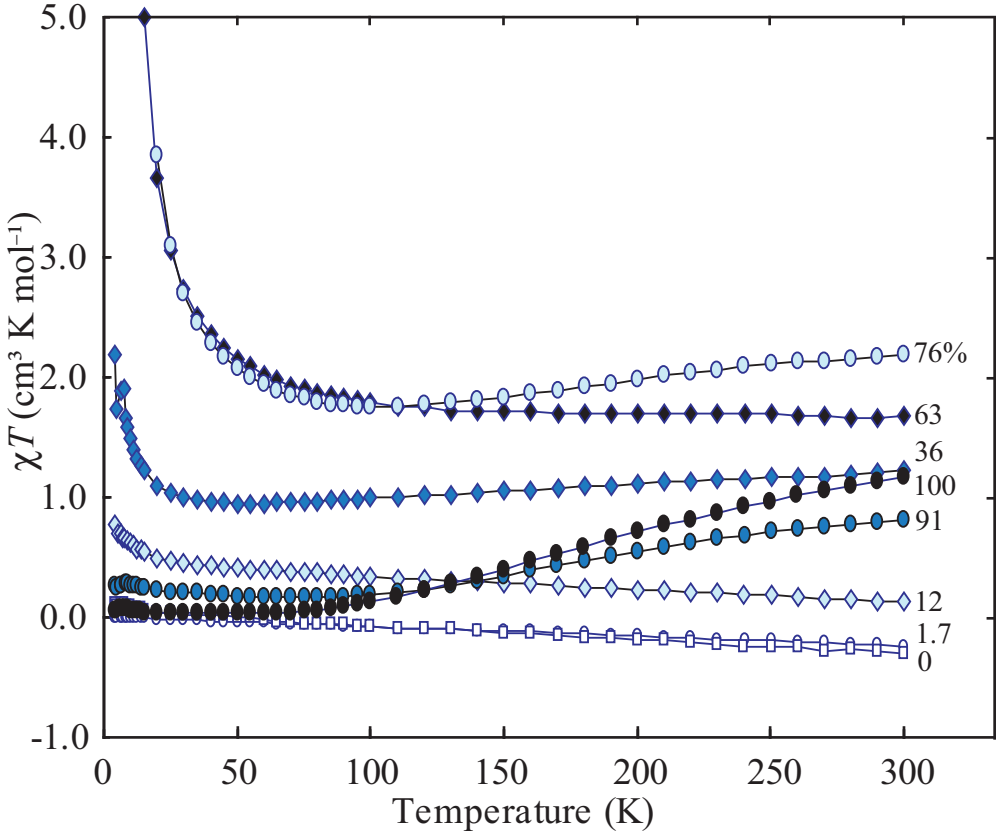

Figure 6.9: χT versus T is plotted for the Zn-Cu terephthalates at 0, 1.7, 12, 36, 63, 75, 91, and 100% Cu. Note how the susceptibilty is predominantly diamagnetic for the low Cu concentrations, paramagnetic for the intermediate ones, and antiferromagnetic for high Cu concentrations.

components and paramagnetic components, the extent amount of Cu–Cu dimers and Cu–Zn dimers can be estimated.

6.3 Discussion

In this system, the Cu(TPA)·DMF is presumed to be nucleating first in solution. Because of the similarity in structure and bonding between Cu(TPA)·DMF and the DMF-coordinated MOF-C*2/m*, any DMF-coordinated Zn ions are easily accommodated into the Cu(TPA)·DMF seed crystal. The coordination environment around the Zn ions is dynamic, so the Zn ions can coordinate water or DMF at any given time. However, when they are coordinated to DMF, they are more likely to be incorporated with the DMF into MOF-C*2/m* and removed from solution. The Cu(TPA) does not appear to have this difficulty, as it forms only one crystal structure and only appears to coordinate DMF in solution. Thus, the presence of Cu ions in a Zn(TPA) solution directs the crystallization

toward the DMF-coordinated MOF-C*2/m* and away from the water-coordinated MOF-2 form.

The first thing that becomes apparent in the image shown in Figure 6.1 is that the pale blue, Cu rich regions blend coherently in to the Zn rich clear regions. This indicates that Cu(TPA)·DMF and the Zn MOF around it have similar crystal structures. Also evident in the image shown in Figure 6.1 is that the rate of nucleation of the Cu(TPA)·DMF must be higher than that of the surrounding Zn MOF. If the reverse were true, The Cu(TPA)·DMF would be visible as part of a wholly separate and disconnected phase or nucleated onto the sides of existing Zn MOF crystals. Therefore, the Cu(TPA)·DMF nucleus must be able to influence and direct the growth of the Zn MOF crystals that grow off of that small nucleus.

These observations are borne out by X-ray powder diffraction measurements of the specimens across the Cu composition range. Figures 6.10 and 6.11 compare the crystalline fractions calculated from the quantitative analysis of the powder diffraction patterns before and after desolvation. The substitution of 10% Zn salt for Cu salt is sufficient to effect a dramatic change in the ratio of MOF-2 to MOF-C*2/m*. In this case, the Cu-free batch is 56% MOF-2 and 44% MOF-C*2/m*. With the addition of 12% Cu, the crystalline fractions are 69, 23, and 8% for MOF-2, MOF-C*2/m*, and Cu(TPA)·DMF respectively. After desolvation, only one crystal structure for Zn(TPA) is seen and the comparison between this structure and that of Cu(TPA) indicates that the resulting crystalline powder is much more like a binary mixture than a heterometallic product.

The first striking feature about the comparison between the desolvated crystalline fractions is that the ratio between MOF-2 and MOF-C*2/m* has changed from roughly 1:1 to 1:9. The second is that, for a 10% addition of Cu to the initial salt solution, 23% of the product is behaving as Cu(TPA)·DMF. These results would only be possible if the Cu(TPA)·DMF nuclei were able to serve as the nuclei for the Zn MOF and direct the MOF into MOF-C*2/m*. It is also apparent that these Cu(TPA)·DMF nuclei must also incorporate Zn ions without adopting the crystal structure of the surrounding MOF-C*2/m* lattice. One way for this to occur would be for the resulting MOF to incorporate heterometallic zinc and copper dimers. As mentioned earlier, Cu(TPA)·DMF is also in the C*2/m* space group, and the difference between the Cu(II) and Zn(II) ionic radii is 1.1% [45]. The distance between the coordinated oxygen on the DMF molecule and the metal center in Cu(TPA)·DMF is 2.152 Åand the distance in MOF-C*2/m* is 1.978 or 2.0 Å. This may explain the

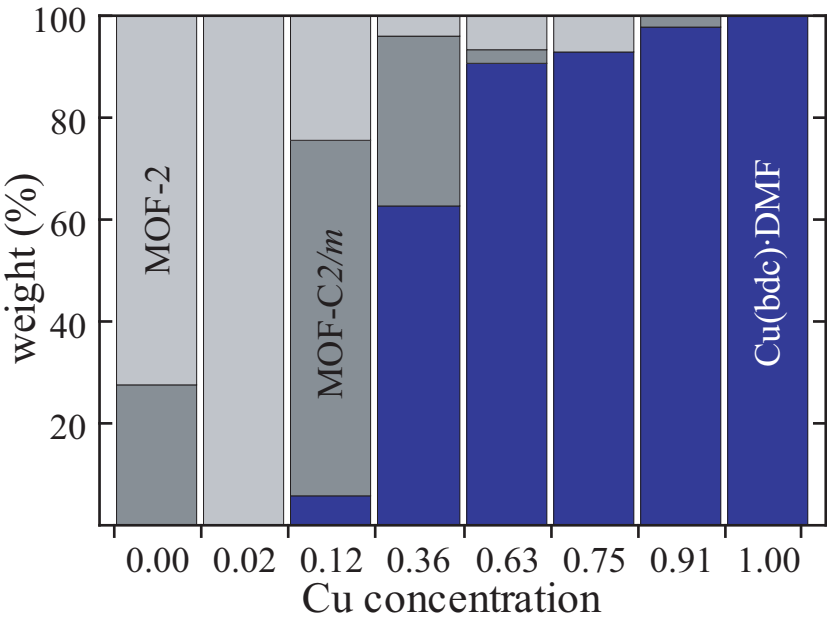

Figure 6.10: The bar graph compares the quantitative estimates of the crystalline fractions of the Zn-Cu terephthalates prior to desolvation. The blue series corresponds to Cu(TPA)·DMF, the dark gray to MOF-C*2/m*, and the light gray to MOF-2. The presence of 12% Cu in the framework has the effect of changing the dominant Zn MOF from MOF-2 to MOF-C*2/m*. Moreover, the percentage of Cu(TPA)·DMF tends to be higher than the amount of Cu added to the synthesis.

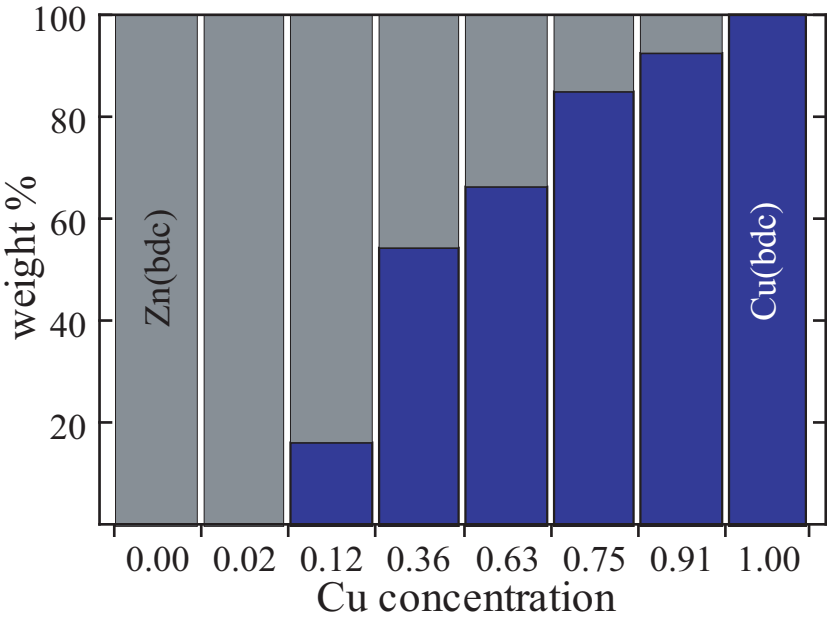

Figure 6.11: The bar graph compares the quantitative estimates of the crystalline fractions of the Zn-Cu terephthalates after desolvation. The blue series corresponds to Cu(TPA)·DMF, the dark gray to the desolvated Zn(TPA). After desolvation, the composition begins to look more like a binary mixture, but the percentage of Cu(TPA) still tends to be higher than the actual Cu composition.

difference in interlayer spacing in the framework prior to desolvation. In MOF-C*2/m* the interlayer spacing is 5.11 Å, and in Cu(TPA)·DMF the interlayer spacing is 5.21 Å [45].

The thermogravimetric analyses reveal a striking effect of the presence of Cu impurity in a Zn(TPA) matrix. A decrease in the desolvation temperature, from 162 to 123 °C appears with the addition of 10% Cu to the initial solution. The initial temperature of 162 °C is close to what has been reported for MOF-2 [41], but it appears that the presence of the copper, and perhaps the larger amount of solvent, acts to initiate desolvation at a lower temperature. Notable is that the changes in crystal structure were intrinsic, and not dependent upon the presence of the solvent. If the changes in the crystal structure were dependent on the presence of the solvent, the upper degradation temperatures for the Zn-rich side of the phase diagram would have been unchanged. However, Figure 6.12 shows that the peak associated with the primary degradation temperature, occurring after desolvation, increases from 403 to 439 °C.

In addition to the temperature changes, Figure 6.13 shows that the mass fractions associated with the different degradation temperature events are changing with respect to Cu concentration. Specifically, the relative ratios associated with the two Zn(TPA) coordination modes change drastically, with the high temperature form decreasing from 45% to zero with the presence of a 12% Cu concentration. Accordingly, the mass fraction associated with the low temperature mode increases from 10 to 40% with the same 12% Cu concentration. The difference between the two is offset by a 10% increase in the amount of solvent present in the initial structure. For gas sieving and separation applications, this is a beneficial change as it indicates that the structure should have more open porosity and greater surface area. As shown in Figure 6.7, the BET overall curve indicates that there is a disproportionate increase in the surface area for a small amount of Cu, as indicated by uptake of solvent seen in the TGA analyses. On the other hand, the addition of a small amount of Zn to a Cu-rich terephthalate seems to have the effect of preferentially lowering the surface areas.

These results are also supported by mass fraction estimates from the XRD analyses. Figure 6.14 shows a comparison between estimates of the fraction of Cu(TPA)·DMF as a function of Cu. Prior to desolvation, there is a larger portion of the solid behaving as Cu(TPA)·DMF. For both TGA and XRD estimates, the behavior becomes more linear after desolvation, indicating that Zn that had

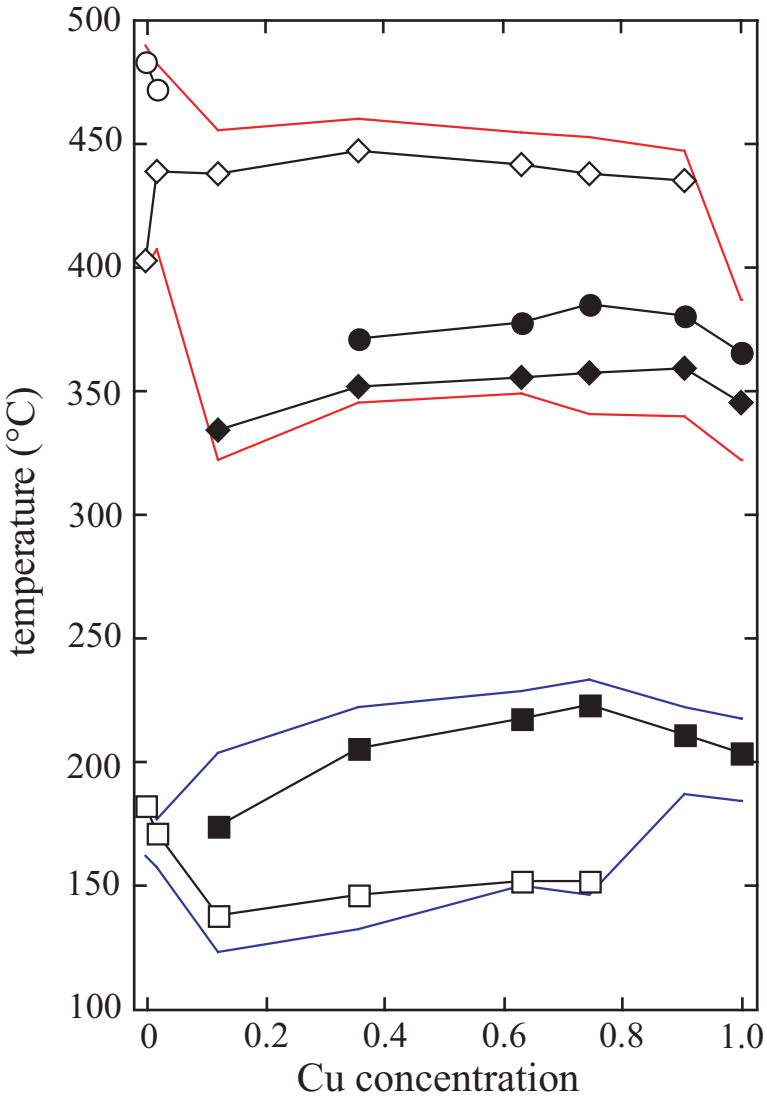

Figure 6.12: The temperature at which different weight loss events take place is plotted as a function of Cu concentration in the Zn-Cu terephthalates. The clear squares (□), diamonds (◇), and circles (○) correspond to the desolvation of Zn(TPA) and its first and second framework degradation events. The dark squares (■), diamonds (◆), and circles (●) correspond to the desolvation of Cu(TPA) and its first and second framework degradation events. In addition the blue and red lines indicate where the desolvation and degradation steps start and end.

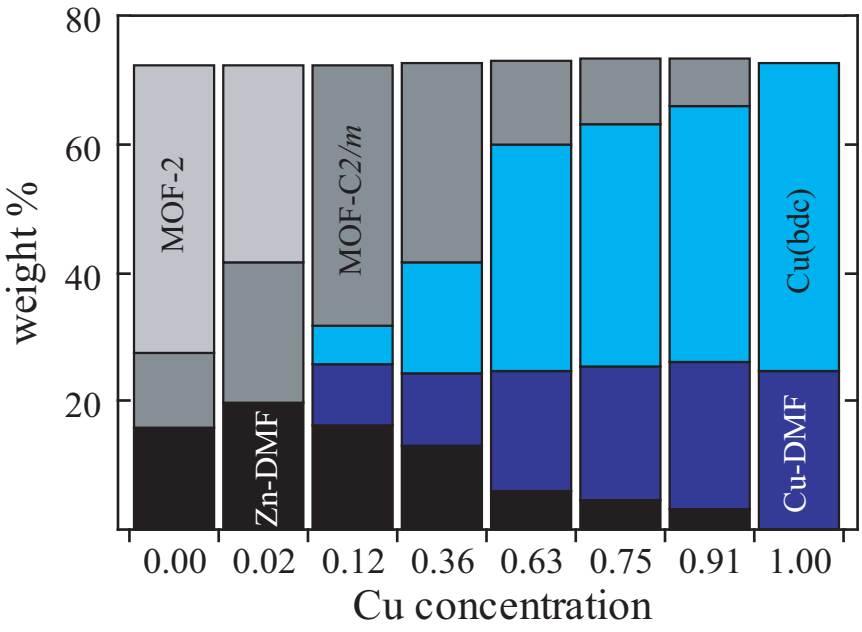

Figure 6.13: The bar graph compares the quantitative estimates of the mass fractions taken from TGA measurements. The black series corresponds to the DMF associated with MOF-2 or MOF-C*2/m*. The dark blue series corresponds to the DMF coordinated to Cu(TPA)·DMF. The dark gray series corresponds to the terephthalate associated with MOF-2. The light blue series corresponds to the terephthalate associated with Cu(TPA). The light gray series corresponds to the terephthalate associated with MOF-C*2/m*. In addition to taking up more solvent, the thermal degradation events in the Zn(TPA) appear to switch places, with the MOF-C*2/m* process dominating in the presence of 12% Cu.

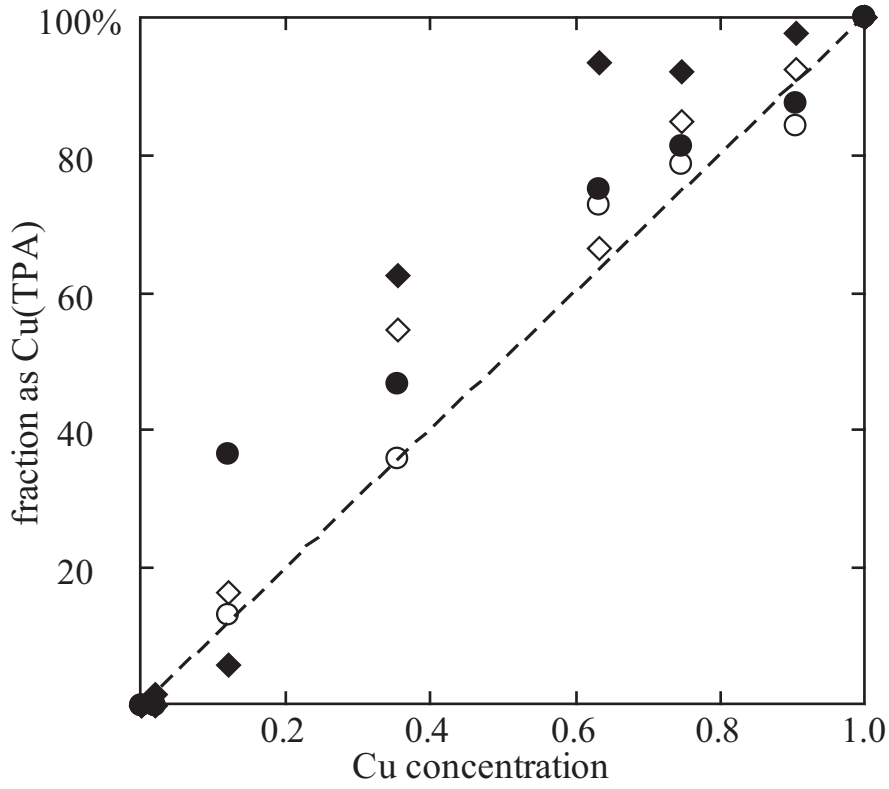

Figure 6.14: The estimated percentage of product acting as Cu(TPA) is shown as a function of Cu present. The black and white diamonds ((◆) and (◇)) correspond to the estimates from XRD measurements before and after desolvation, respectively and the black and white circles (● and ○) correspond to estimates taken from TGA measurements before and after desolvation, respectively. Notable is that, the Cu(TPA) incorporates Zn ions, rather than Cu being incorporated by a MOF-2 or MOF-C*2/m* structure.

formerly behaved as Cu(TPA)·DMF became indistinguishable from the rest of the desolvated Zn lattice. Notable is that both solvated and desolvated structures tend to behave more like Cu(TPA)·DMF than one of the Zn MOFs. The exception to this was the 91% Cu sample, which for the TGA-based estimates, indicated that Cu was behaving as Zn(TPA) rather than the other way around.

Evidence of this same phenomenon appeared in the IR spectra as well. As predicted, the vibrational spectra did not reveal substantial changes in the coordination geometry around the metal center, regardless of Cu concentration. Figure 6.15 shows the area under a given peak as a function of Cu concentration. For the most part, the trends are linear, favoring Cu(TPA)·DMF over Zn(TPA). However, the sample with 91% Cu did not follow the same trend as the others, with very small peaks that absorb strongly on both adjacent compositions. Figure 6.16 shows the absorbance of Zn(TPA)

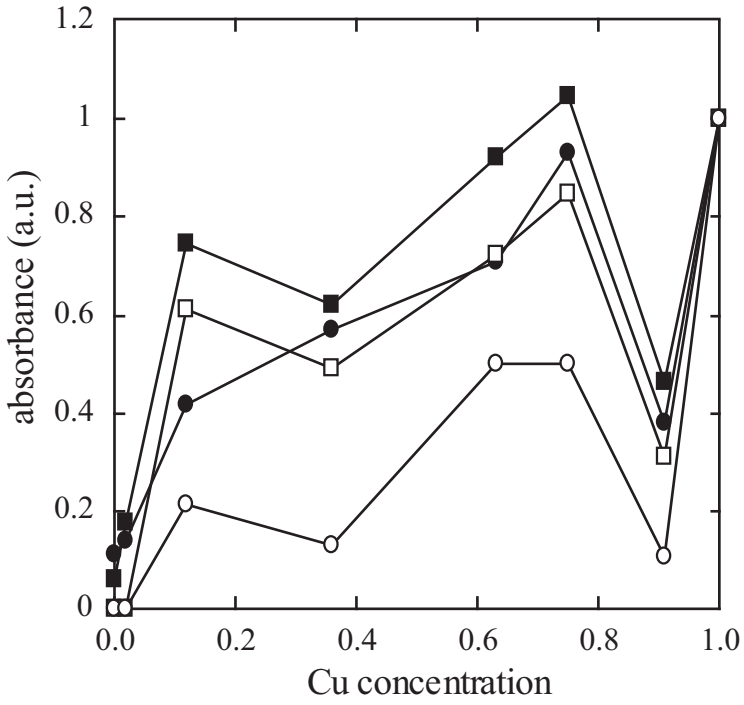

Figure 6.15: The relative absorbance of four different Cu(TPA) correlated peaks: 880 (black circles, ●), 928 (white circles, ○), 1133 (black squares, (■)), and 1697 cm^{-1} (white squares, □). Note the large drop in all the peaks for the 91% Cu specimen.

correlated peaks as a function composition. Whereas we would expect from Figure 6.15 that the absorbances from the Zn(TPA) correlated peaks would be high for the 91% Cu sample, they are also low. This measurement was repeated with different samples of the same composition with little variation.

The curious thing about this pattern is that, if a simple binary mixture had been produced between the Cu and Zn terephthalates, one would expect to see more peaks, not fewer. Even in the event that all the Zn(II) ions were dimerizing with Cu(II) ions, the broken symmetries present would dictate that more peaks would appear. Thus, these results possibly suggest the presence of a line compound in this phase diagram.

The clearest evidence of dimerization in the Zn-Cu terephthalates appears in the magnetic susceptibilities. These were modeled according to a variation on the Bleaney-Bowers-Kahn Equation 6.1:

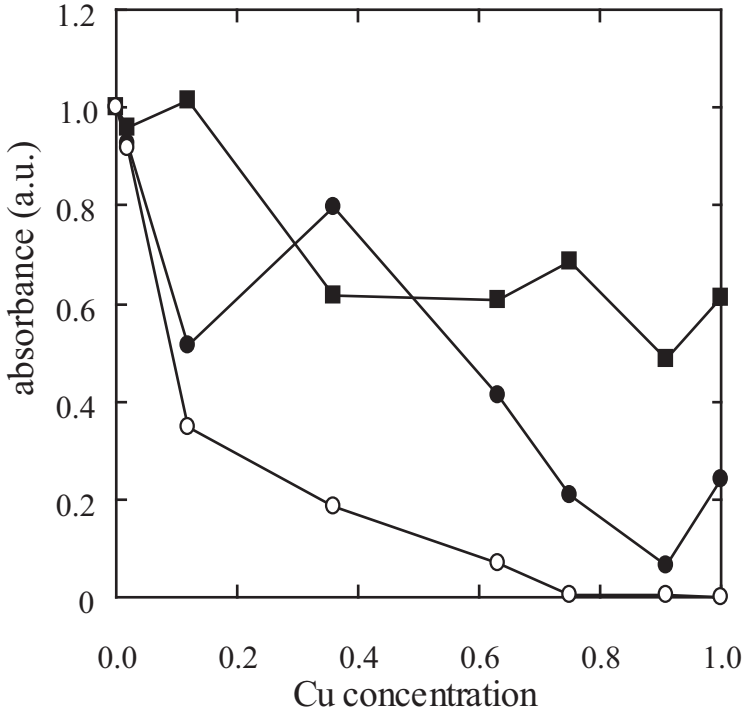

Figure 6.16: The absorbance of three different Zn(TPA) correlated peaks: 451 (black circles, ●), 493 (white circles, ○), and 829 cm^{-1} (black squares, ■).

$$\chi_M = \frac{2N_a g^2 \mu_B^2}{k} \left\{ \left[3 + \exp\left(\frac{-J}{kT}\right) \right]^{-1} \frac{1-\rho}{T} + \frac{\rho}{4(T-\Theta)} \right\} \tag{6.1}$$

$$f_{para} = \rho \cdot f_{Cu} \tag{6.2}$$

The meaning of the symbols is the same as that in chapter 4. In addition, the splitting energy, J is fixed at 311 cm^{-1} and the g-factor is fixed at μ_B^2 = 2.12. Because the Bleaney-Bowers-Kahn assumes only a small paramagnetic impurity, and because that paramagnetic "impurity" dominates the susceptibility, a Weiss temperature Θ was added to the paramagnetic side of the equation. In addition, the temperature independent paramagnetism (TIP) was added to the equation. This term arises when electrons in the diamagnetic ground state couple with those in excited states. For the antiferromagnetic Cu(TPA) the TIP is negligible, but as the number of paramagnetic centers increased, the need for a TIP term became necessary. Table 6.2 shows the values of the different parameters as a function of Cu concentration.

The least squares fitting of the data above results in an estimate of the paramagnetic and antiferromagnetic contributions of the susceptibility, shown in Figure 6.17. The results indicate that

Table 6.2: A table showing the values for the fraction of paramagnetic centers, the Weiss temperature, TIP, and fit standard deviations as a function of Cu concentration.

f_{Cu} (%)	0.12	0.36	0.63	0.75	0.91	1
ρ (%)	68.5	90.1	73.8	52.9	20.7	2.4
f_{Para} (%)	8.2	32.4	46.5	39.7	18.9	2.4
Θ (K)	1.5	4.3	10.7	10.1	1.8	2.4
TIP ($emu \cdot mol^{-1} \times 10^{-6}$)	21.7	9.3	30.2	51.3	11.2	1.5
R^2 of fit	0.991	0.990	0.999	0.998	1.000	1.000

a large number of interstitial Cu ions are present for the 64 and 75% samples. This is evident in that the fraction of paramagnetic Cu exceeds the fraction of Zn centers. It is speculated that the additional paramagnetic component may be derived from "interstitial" Cu ions that are not part of the framework.

In addition, the Weiss temperature results are plotted in Figure 6.18. As noted earlier, the Weiss temperature is an indicator of the antiferromagnetic or ferromagnetic character of the interaction parameter, J. The positive numbers shown in Figure 6.18 indicate a strong ferromagnetic component to the fraction of paramagnetic Cu centers. The Weiss temperature of 10 K for the compositions of 63 and 75% Cu was higher than other reports for related systems. Examples include the hydrated $Cu(TPA)(H_2O)_2$ synthesized by Deakin that has been reported to show Θ = +0.8 K [81]. However, the character of our samples may have more in common with a layered Cu hydroxyterephthalate $Cu_2(TPA)(OH)_2$, which was reported to have Θ = +25 K [97]. The variation in the Weiss temperature is attributed to weak inter-layer superexchange of Cu atoms. As these measurements were carried out after desolvation, there is an opportunity for adjacent layers to interact through the O atoms on the carboxylate groups. At low concentrations, the Cu atoms are spaced too far apart, and the next nearest metal center is another Zn atom on the adjacent layer. At higher Cu concentrations, the likelihood of two heterometallic dimers interacting magnetically increases, increasing the interaction between them. At 100% Cu, only the interstitial Cu is present.

6.4 Conclusions

This study demonstrates that the thermal and structural properties of Zn(TPA) can be modified by the presence of a Cu salt impurity. This also has the effect of changing the crystal morphology

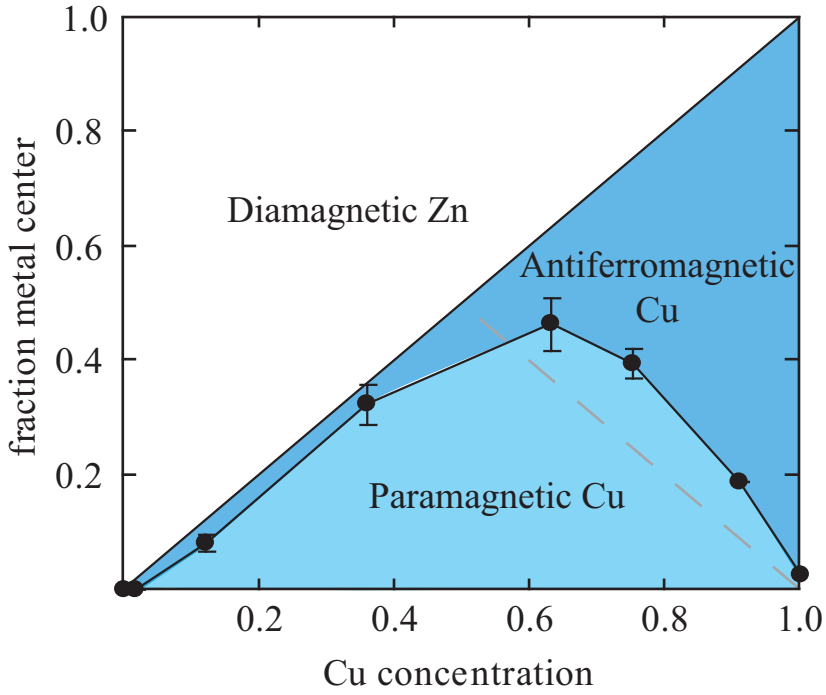

Figure 6.17: The total fraction of metal centers displaying paramagnetic susceptibility is shown above in the dark circles (●). Because the Cu centers in the framework must be dimerized with Zn centers to behave paramagnetically, the actual value in the framework must be below the Cu concentration (solid line) and below the Zn concentration (dashed line). The excess paramagnetic component is attributed to interstitial Cu ions.

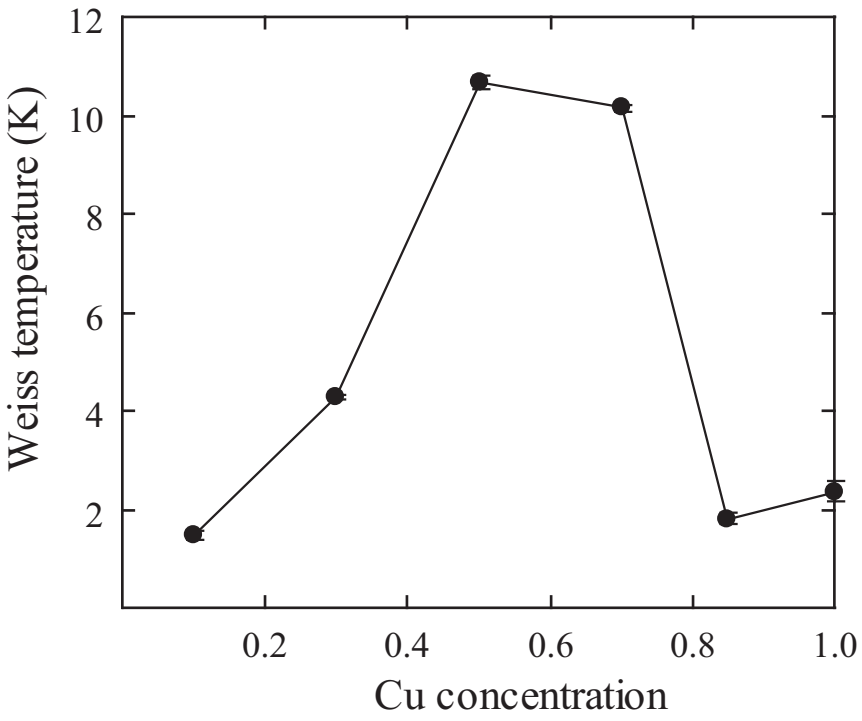

Figure 6.18: The graph shows the Weiss temperature, Θ, of the paramagnetic component of the Zn-Cu terephthalate framework as a function of Cu concentration. The variation is attributed to the extent of interaction between heterometallic dimers on adjacent layers.

and increasing the available surface area after desolvation. For Cu rich samples, the presence of a small amount of Zn has the effect of dimerizing with Cu and changing the magnetic properties from antiferromagnetic to paramagnetic. This results in a drastic increase in the room temperature magnetic susceptibility as well as an increase in the Weiss temperature. These findings are expected to have application in a few areas. For example, the heterometallic dimerization of Zn and Cu could play a role in the synthesis of methanol. If Zn(TPA) MOFs were ever synthesized on a large scale, Cu salts could be added to increase the surface area. To a wider extent, it is hoped that this study serves as an example of how existing homometallic MOF systems could be improved by the addition of a heterometallic impurity.

CHAPTER VII

CONCLUSIONS

The developments in supra-molecular chemistry over the past decades have produced many materials with promising electrical and optical properties. That promise is not always deliverable, but the process of uncovering the many mechanisms at work can result in greater understanding of structure and bonding interaction for a wider variety of systems. As an example of this, poly-$[Rh(pdi)^{+}_{4/2}(Cl)^{-}]_n$ was assumed to display semi-conducting behavior at 1 kHz. Although our measurements showed that this was not the case under direct current, we were able to show through electrical and structural measurements that the presumed dominant mechanism of conductivity, metal-metal bonding, was likely the correct one. In addition, through thermal and chemical methods, we were able to construct a mechanism for the degradation of the polymer in air, and how this degradation was quenching the dominant conduction mechanism.

Deciding to investigate a less expensive, more stable ligand and a non-precious metal center, we were able to develop a synthesis and provide a structure for Cu(TPA)·DMF. When thermally desolvated, this metal organic framework demonstrated a surface area of 625 m^2g^{-1} and a thermal stability above 300 °C. This was an important step in laying a foundation for the use of 2-dimensionally coordinated, high surface area MOFs. HKUST-1 (Cu benzentricarboxylate) and MOF-5 are among some of the better studied MOFs that are very similar to the Cu(TPA).

We expanded our inquiry to include other metal terephthalates: Mg, Co, Ni, and Zn. In the process we were able to solve the structure of Ni(TPA)·DMF as well as drawing inferences about the nature of the chemical environment around the metal center from the IR spectra. The magnetic susceptibilities of Co and Ni(TPA)·DMF, which to our knowledge had not been reported previously, were also measured. The understanding of these basic systems serves as a basis by which some of the more complicated MOFs being produced can be understood. This type of study is also useful as a means of finding relationships between apparently disparate chemical systems.

Finally, we attempted to design and synthesize a MOF with heterometallic secondary building

units, something that, to our knowledge has not been previously reported. We chose the Zn-Cu terephthalate system on account of its spectacular suitability during a set of combinatorial experiments with a range of mixed metal salt solutions. The Zn-Cu terephthalate system was found to prefer to crystallize in the Cu(TPA)·DMF beyond the amount of Cu present in the system. There was also evidence that this was the case even after thermal desolvation. Adding Cu to Zn also had the effect of drastically increasing the surface area. These changes in crystallization were attributed to the ability of Cu(TPA)·DMF to nucleate faster than Zn(TPA)·DMF. The DMF-coordinated Zn ions could then be incorporated into the Cu(TPA)·DMF seed crystals and removed from solution much more quickly than the water-coordinated Zn ions. This had the effect of changing the dominant crystal structure from MOF-2 to MOF-C*2/m*. In addition, the magnetic susceptibility measurements performed over the entire compositional range demonstrated the presence of heterometallic dimerization in the framework. To our knowledge, this has not been previously reported and is expected to have application in catalysis, where the combination of easy access to catalytic sites, and a combination of metal centers is expected to have novel applications.

What has been accomplished so far is only the beginning. There were many possible leads that could not reach their desired conclusions in time to write this thesis. Our work with the research group of Prof. Seung-Soon Jang has led to a computational model of the crystalline structure of the desolvated Cu(TPA). This model, arrived at through a combination of Rietveld refinement and molecular dynamics energy optimization, can form a template for predicting the vibrational properties of both Cu(TPA) and similar systems. It is hoped that Cu(TPA) will also see adoption along-side HKUST-1 as a basis for studying the properties of MOFs with different geometries.

We have also worked with Jason Ward and Ryan Adams from the research group of Prof. William Koros to investigate the suitability of mixed membranes of Cu(TPA). Making mixed membranes with micro-porous materials, often zeolites, can be difficult because the gas separation properties are dependent upon the strength of the interface between the polymer and the filler. If the interface is weak, then voidspaces are created, making the gas separation difficult to maintain. While none have yet been tested, some of the preliminary work looks very promising. Figure 7.1 shows an SEM image, taken by Jason Ward, of a fracture surface of a mixed membrane of Cu(TPA) and a cross-linking polymer. Because Cu(TPA)·DMF was originally added and then it was cured at

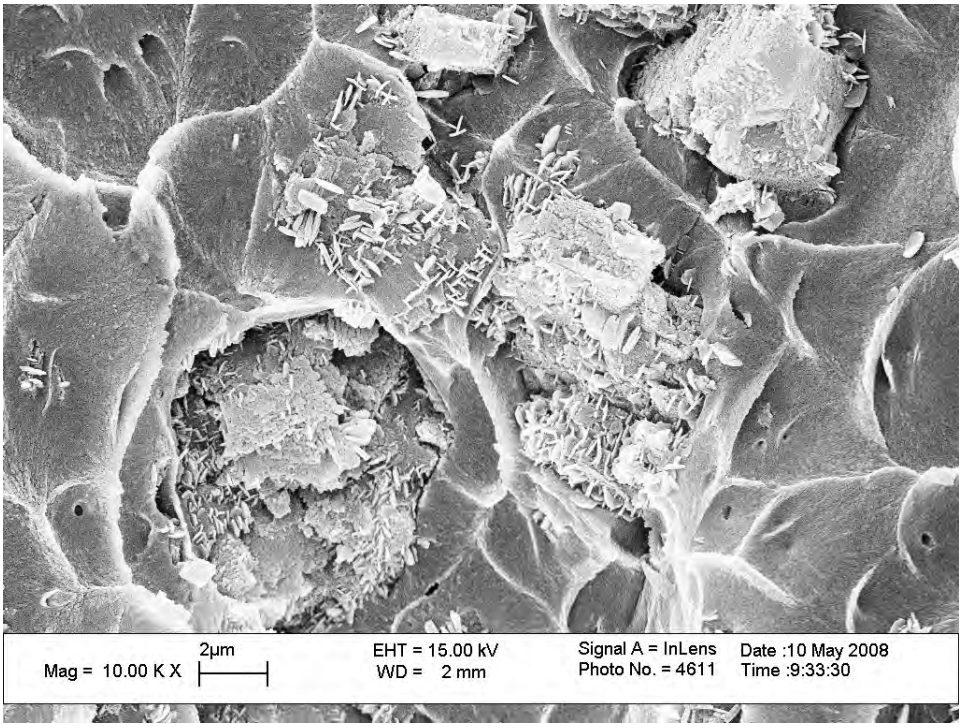

Figure 7.1: Shown is an SEM image of the fracture surface of a cured mixed membrane of Cu(TPA) and crosslinking polymer. Note attachment of the smaller platelets.

220 °C, the desolvation to Cu(TPA) and the associated change in unit cell volume resulted in large voidspaces being created. This meant that this film was unsuitable for use as a gas separation membrane. However, closer inspection will reveal that the smaller platelets have good adhesion to the polymer, these undergoing desolvation prior to the completion of the high-temperature cure. There are plans to repeat this experiment with Cu(TPA) desolvated prior to mixing in the resin and curing. In addition, we are prepared to examine the feasibility and utility of synthesizing a layer of Cu(TPA) on the surface of the Zeolite particle. We have done preliminary work with the research group of Prof. David Sholl in the School of Chemical and Biochemical Engineering to model the gas permeation constants for Cu(TPA).

We have also been synthesizing new heterometallic terephthalates. Although we were unable to proceed further with characterization of the $Ni_{0.97}Cu_{0.03}$(TPA), it presents exciting opportunities. The heterobimetallic molecular magnet from the coupling of Ni(TPA), with ferromagnetic coupling, and the Cu(TPA), with anti-ferromagnetic coupling, might yield a magnetically dilute system with interesting properties. Of particular interest is $Zn_{1-x}Rh_x$(TPA), another framework that changes

from pale yellow to bright red when placed in an X-ray beam.

For all that has not been accomplished within the alloted time for this work, it is hoped that the results presented in this thesis have paved the way for others to make rapid progress in this arena should they choose to do so.

APPENDIX A

INFRARED SPECTROSCOPY DATA

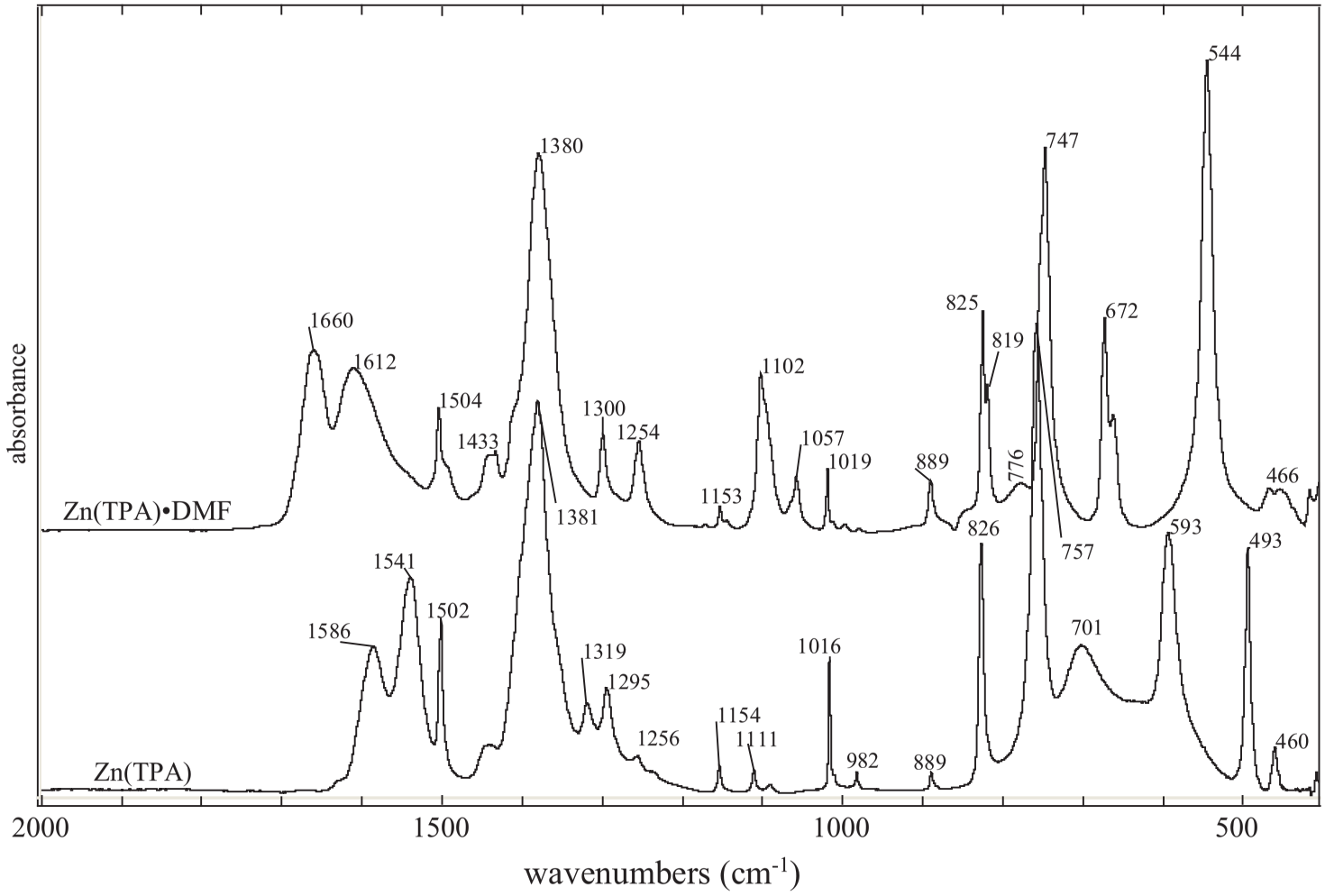

Figure A.1: The FTIR spectra of Zn(TPA) both before and after desolvation are shown as function of wavenumber.

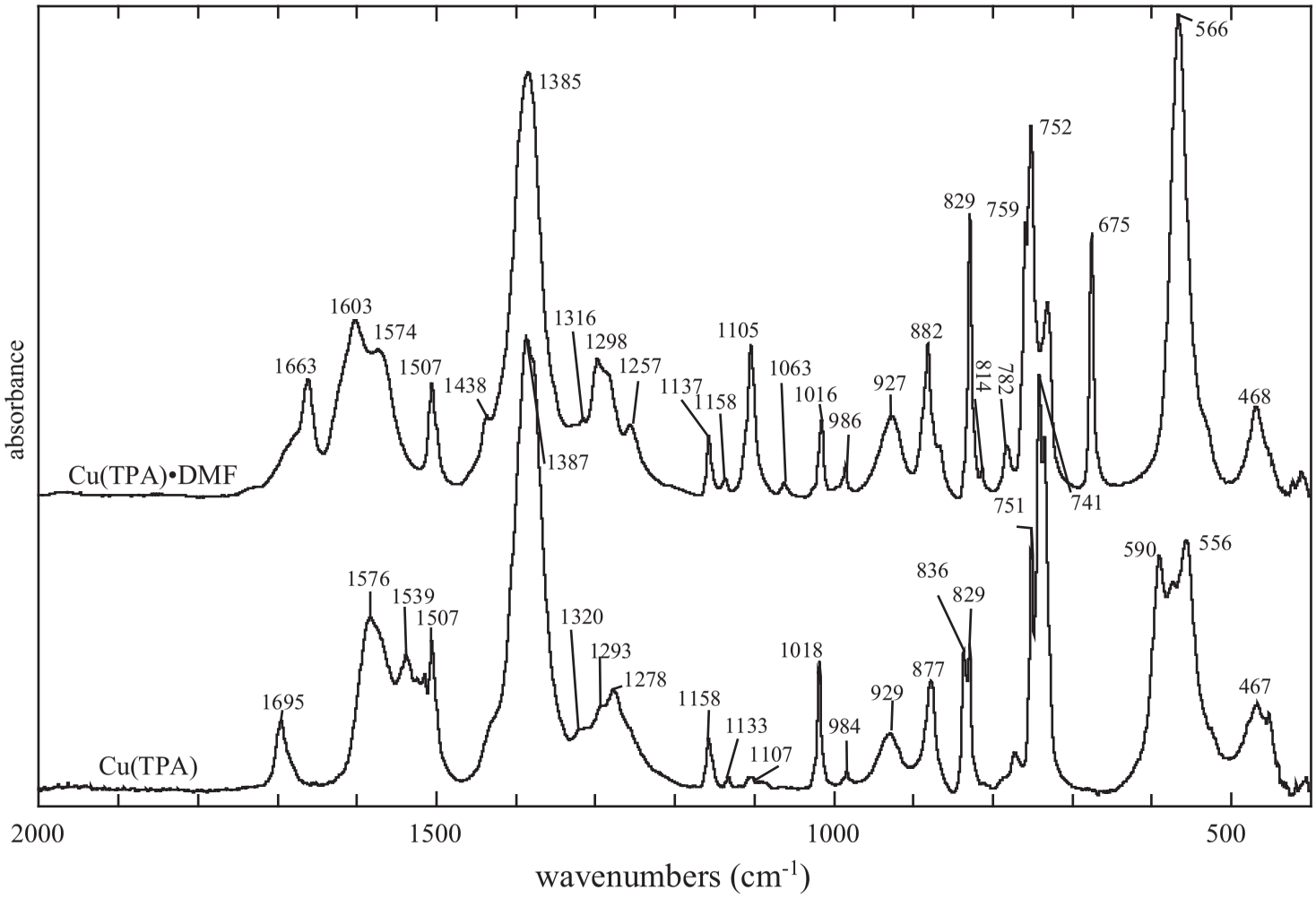

Figure A.2: The FTIR spectra of Cu(TPA) both before and after desolvation are shown as function of wavenumber.

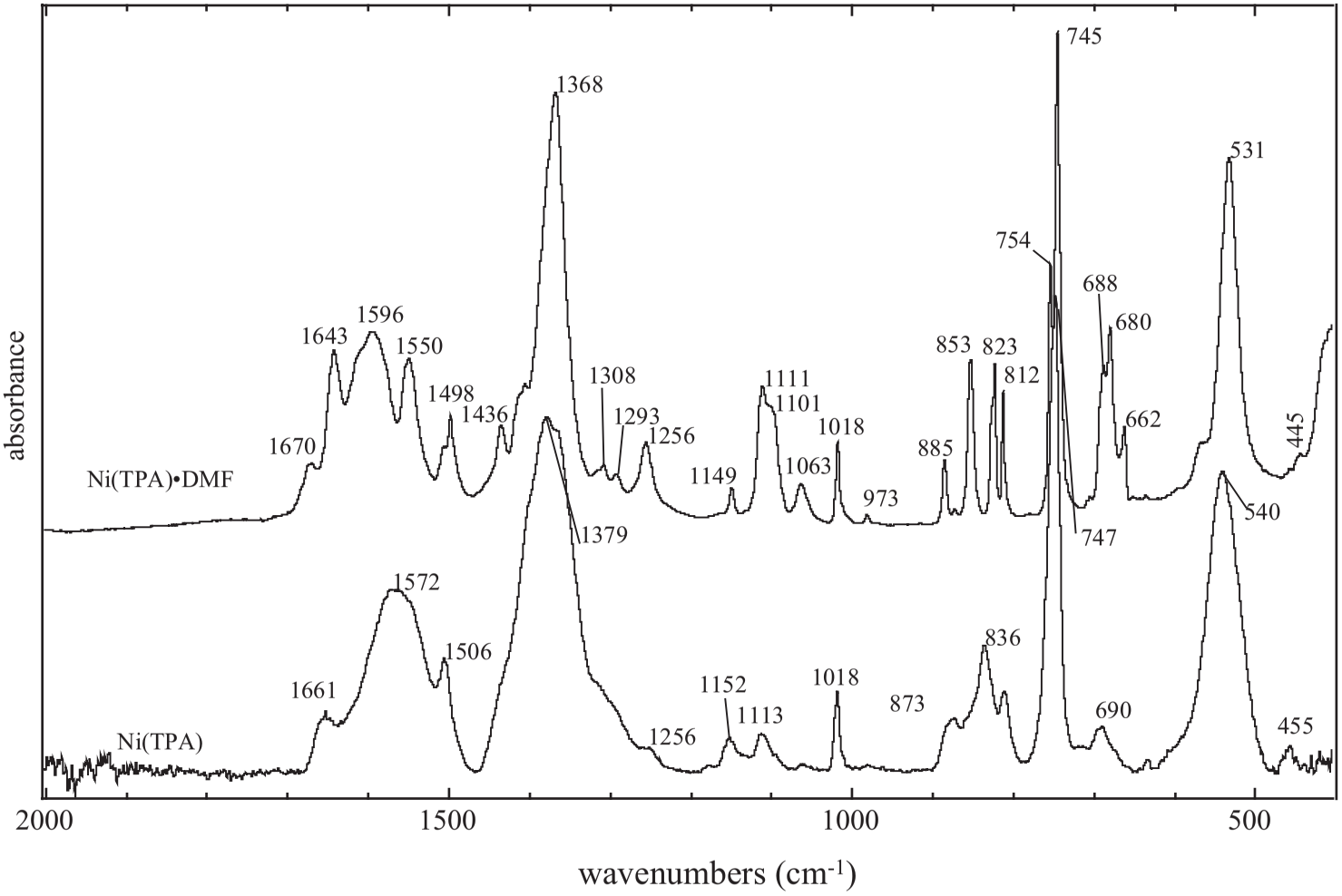

Figure A.3: The FTIR spectra of Ni(TPA) both before and after desolvation are shown as function of wavenumber.

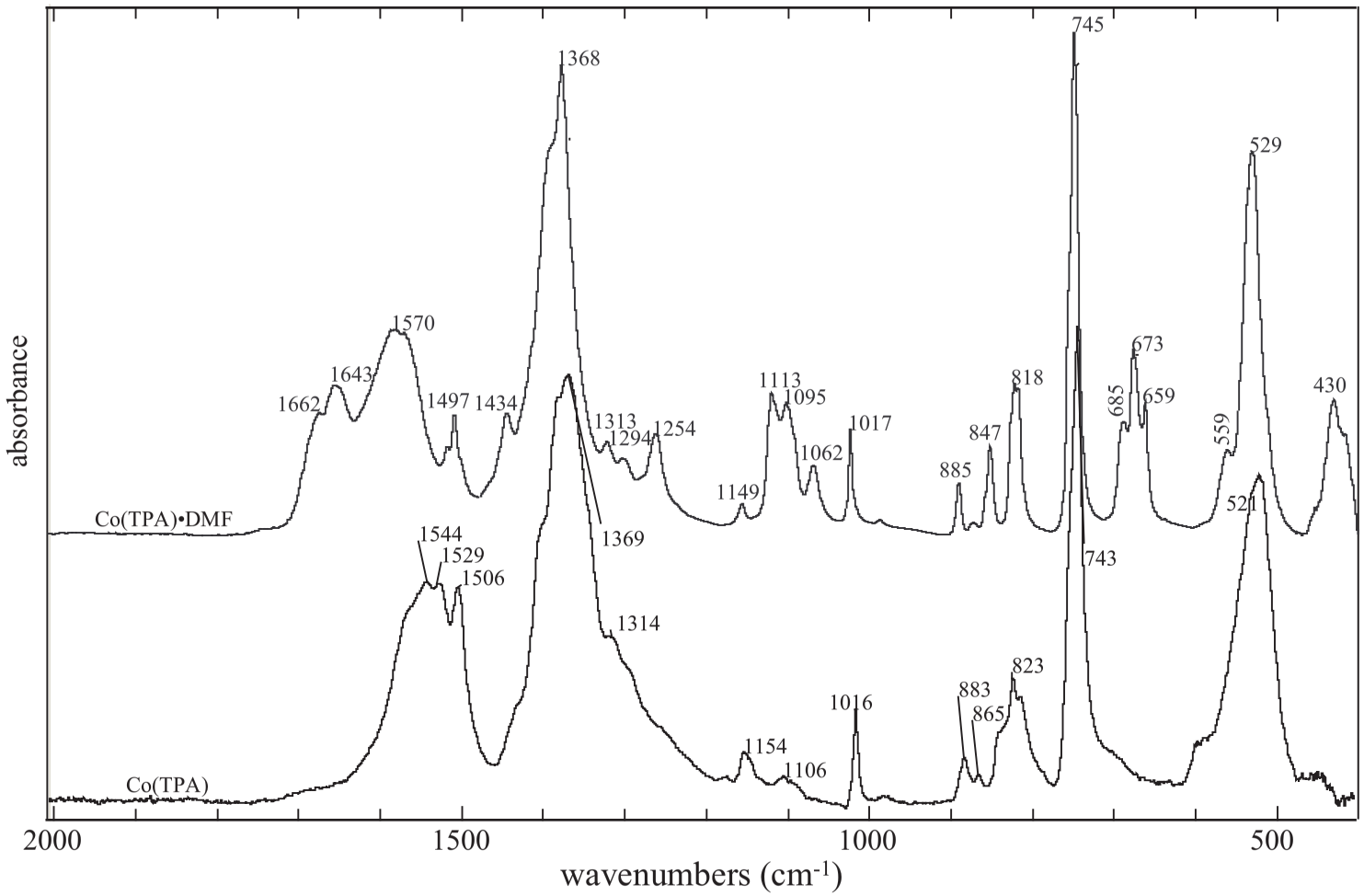

Figure A.4: The FTIR spectra of Co(TPA) both before and after desolvation are shown as function of wavenumber.

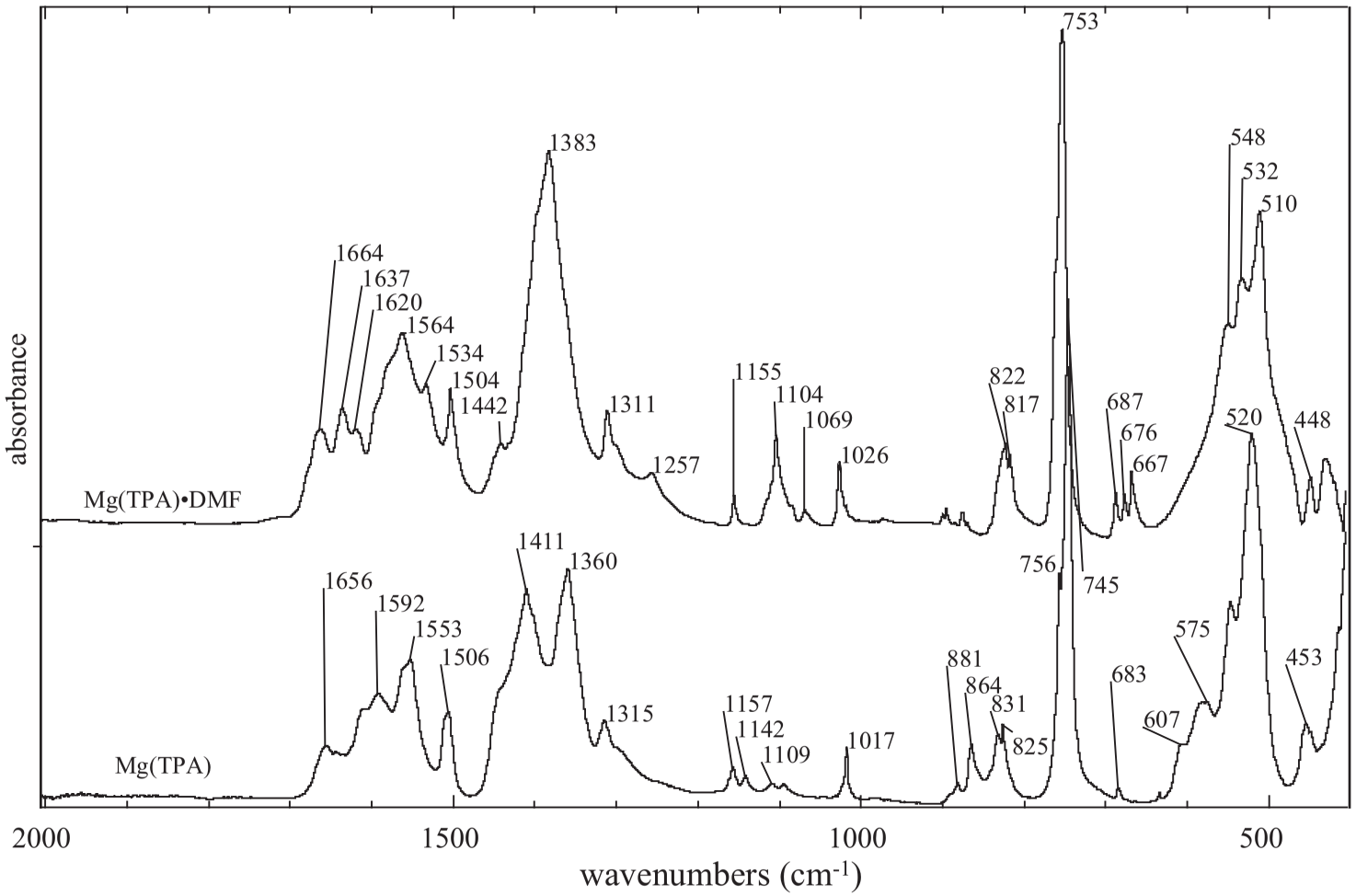

Figure A.5: The FTIR spectra of Mg(TPA) both before and after desolvation are shown as function of wavenumber.

APPENDIX B

CRYSTAL STRUCTURE

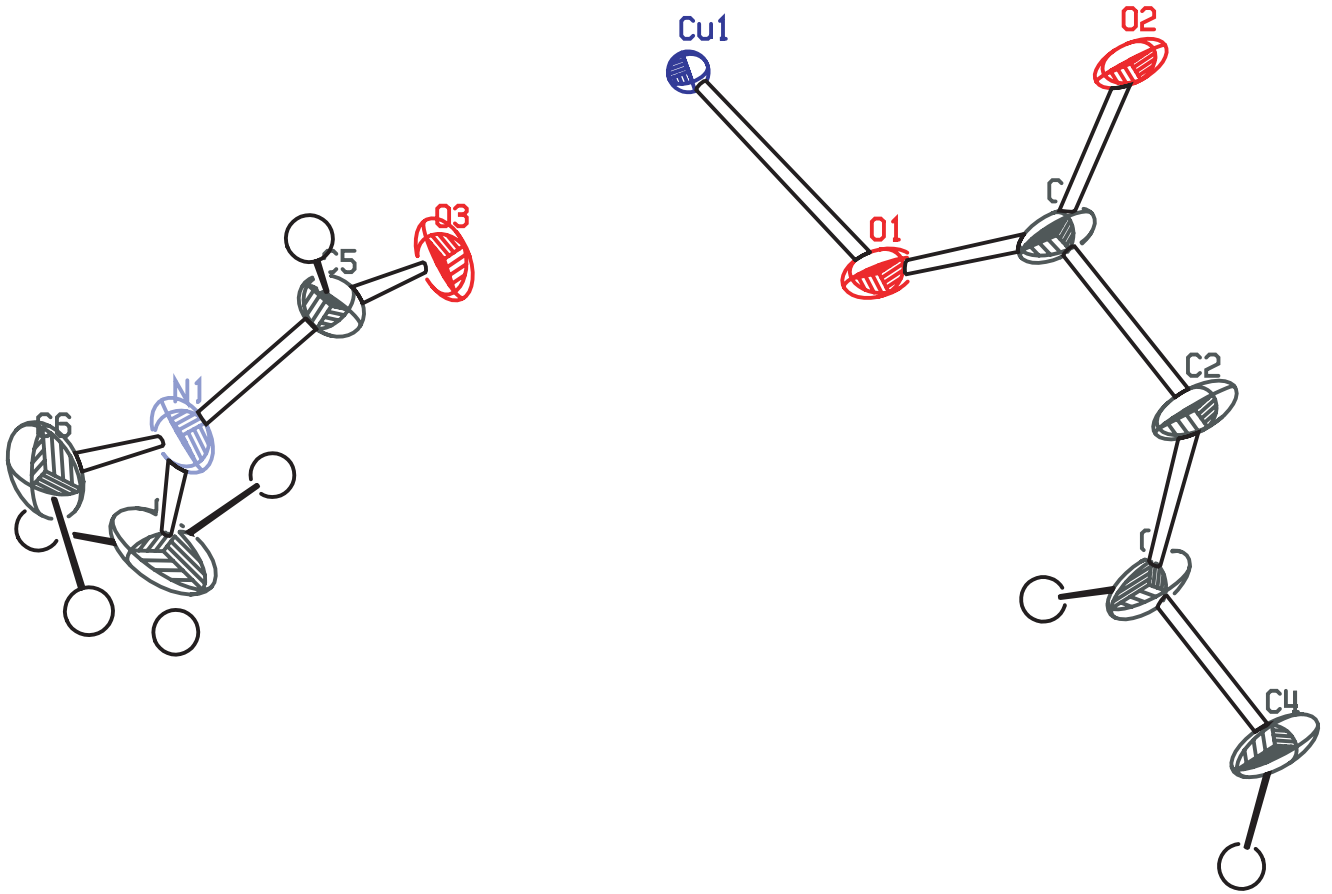

Figure B.1: The ORTEP drawing of the asymmetric unit of Cu(TPA)·DMF. Thermal ellipsoids are drawn at 50% probability.

Table B.1: A table with the fractional coordinates of the atoms in the Cu(TPA)·DMF crystal structure. Also included are the associated anisotropic parameters.

Num	Label	SFAC	Coordinates			Uij coordinates					
1	C1	1	-0.1130	0.1210	0.2750	0.0390	0.0220	0.0168	0.0096	0.0129	0.0202
2	C2	1	-0.1840	0.1880	0.1330	0.0510	0.0370	0.0208	0.0177	0.0200	0.0324
3	C3	1	-0.1650	0.1900	-0.0360	0.0570	0.0470	0.0240	0.0195	0.0248	0.0440
4	C4	1	-0.2300	0.2510	-0.1670	0.0610	0.0480	0.0206	0.0210	0.0266	0.0420
5	C5	1	0.3280	0.0670	0.3970	0.0200	0.0170	0.0240	0.0010	0.0110	-0.0010
6	C6	1	0.5180	0.1530	0.4400	0.0230	0.0250	0.0730	0.0130	0.0130	-0.0100
7	C7	1	0.4310	0.0460	0.1750	0.0560	0.0790	0.0620	0.0130	0.0490	0.0050
8	H3	2	-0.1140	0.1480	-0.0720	0.0100	0.0000	0.0000	0.0000	0.0000	0.0000
9	H4	2	-0.2140	0.2570	-0.2810	0.0100	0.0000	0.0000	0.0000	0.0000	0.0000
10	H6	2	0.3490	0.1030	0.5160	0.0460	0.0000	0.0000	0.0000	0.0000	0.0000
11	H7	2	0.3530	0.0000	0.1560	0.0460	0.0000	0.0000	0.0000	0.0000	0.0000
12	H8	2	0.4290	0.0760	0.1250	0.0460	0.0000	0.0000	0.0000	0.0000	0.0000
13	H9	2	0.5050	0.0000	0.1870	0.0460	0.0000	0.0000	0.0000	0.0000	0.0000
14	H10	2	0.5010	0.2110	0.3610	0.0460	0.0000	0.0000	0.0000	0.0000	0.0000
15	O1	3	-0.0110	0.0940	0.2660	0.0343	0.0280	0.0236	0.0161	0.0164	0.0176
16	O2	3	-0.1610	0.0960	0.3930	0.0396	0.0438	0.0223	0.0232	0.0187	0.0301
17	O3	3	0.2430	0.0000	0.3210	0.0148	0.0810	0.0204	0.0000	0.0089	0.0000
18	Cu1	4	0.0890	0.0000	0.4250	0.0082	0.0000	0.0000	0.0000	0.0000	0.0000
19	N1	5	0.4250	0.0860	0.3430	0.0180	0.0300	0.0420	0.0080	0.0160	0.0020

Table B.2: The interatomic distances of Cu(TPA)·DMF are listed.

A	B	Distance
C1	O1	1.252
C1	O2	1.256
C1	C2	1.495
C2	C4	1.391
C2	C3	1.396
C2	C1	1.495
C3	H3	0.935
C3	C4	1.378
C3	C2	1.396
C4	H4	0.961
C4	C3	1.378
C4	C2	1.391
C5	H6	1.017
C5	N1	1.324
C5	O3	1.367
C6	H10	1.016
C6	C6	1.13
C6	N1	1.45
C7	H9	1.045
C7	H7	1.079
C7	C7	1.304
C7	N1	1.447
H3	C3	0.935
H4	C4	0.961
H6	C5	1.017
H7	C7	1.079
H7	C7	1.079
H9	C7	1.045
H9	C7	1.045
H10	C6	1.016
O1	C1	1.252
O1	Cu1	1.941
O2	C1	1.256
O2	Cu1	1.963
O3	C5	1.367
O3	C5	1.367
Cu1	O1	1.941
Cu1	O1	1.941
Cu1	O2	1.963
Cu1	O2	1.963
Cu1	Cu1	2.631
N1	C5	1.324
N1	C7	1.447
N1	C6	1.45

Table B.3: The interatomic angles of Cu(TPA)·DMF are listed.

A	B	C	Angle
O1	C1	O2	125.79
O1	C1	C2	116.99
O2	C1	C2	117.22
C4	C2	C3	119.65
C4	C2	C1	120.62
C3	C2	C1	119.73
H3	C3	C4	114.87
H3	C3	C2	125.08
C4	C3	C2	119.91
H4	C4	C3	121.62
H4	C4	C2	117.78
C3	C4	C2	120.44
H6	C5	N1	101.75
H6	C5	O3	132.77
N1	C5	O3	124.14
H10	C6	C6	117.00
H10	C6	N1	104.66
C6	C6	N1	92.31
H9	C7	H7	104.12
H9	C7	C7	51.37
H9	C7	N1	115.85
H7	C7	C7	52.82
H7	C7	N1	95.67
C7	C7	N1	113.72
C7	H7	C7	74.37
C7	H9	C7	77.26
C1	O1	Cu1	123.04
C1	O2	Cu1	122.69
C5	O3	C5	89.25
O1	Cu1	O1	87.88
O1	Cu1	O2	90.38
O1	Cu1	O2	168.27
O1	Cu1	Cu1	84.53
O1	Cu1	O2	168.27
O1	Cu1	O2	90.38
O1	Cu1	Cu1	84.53
O2	Cu1	O2	88.97
O2	Cu1	Cu1	83.76
O2	Cu1	Cu1	83.76
C5	N1	C7	118.89
C5	N1	C6	121.00
C7	N1	C6	119.92

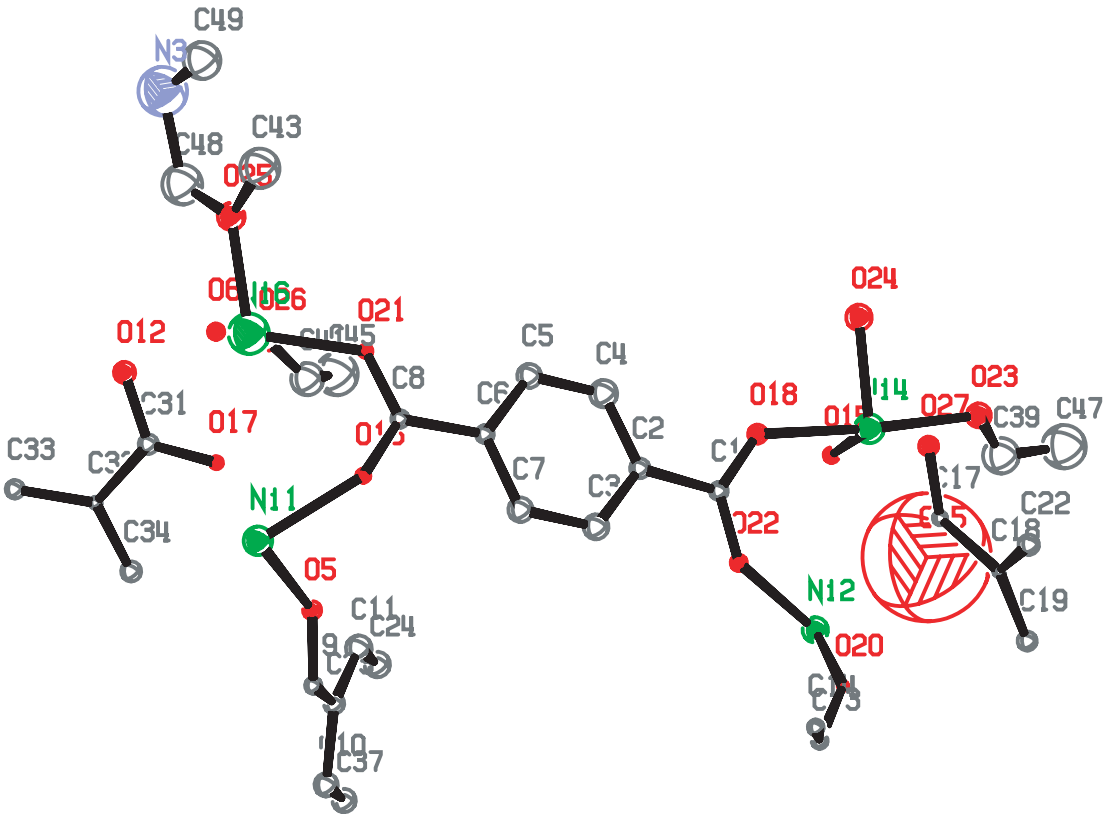

Figure B.2: The ORTEP drawing of the asymmetric unit of Ni(TPA)·DMF. Thermal ellipsoids are drawn at 50% probability.

Table B.4: A table with the fractional coordinates of the atoms in the Ni(TPA)·DMF crystal structure. Only one set of anisotropic parameters could be refined.

Num	Label	SFAC	Coordinates			U coordinate
1	O5	1	1.037	0.934	0.372	0.0097
2	O6	1	0.972	0.950	0.695	0.0073
3	O12	1	1.275	0.908	0.636	0.0133
4	O15	1	0.587	0.265	0.037	0.008
5	O16	1	0.861	0.891	0.487	0.0056
6	O17	1	1.151	0.909	0.527	0.005
7	O18	1	0.531	0.445	0.192	0.011
8	O20	1	0.360	0.612	0.017	0.0032
9	O21	1	0.911	0.767	0.540	0.0053
10	O22	1	0.539	0.561	0.128	0.0081
11	O23	1	0.303	0.210	0.031	0.0183
12	O24	1	0.425	0.263	0.192	0.0204
13	O25	1	1.077	0.775	0.707	0.0212
14	O26	1	1.194	0.714	0.531	0.0176
15	O27	1	0.227	0.407	0.137	0.0107
16	O35	1	0.310	0.409	0.011	0.4977
17	Ni1	2	1.000	1.000	0.500	0.0227
18	Ni2	2	0.500	0.500	0.000	0.0202
19	Ni4	2	0.421	0.326	0.106	0.026
20	Ni6	2	1.076	0.825	0.610	0.0472
21	C1	4	0.561	0.530	0.189	0.0098
22	C2	4	0.629	0.600	0.270	0.0115
23	C3	4	0.653	0.697	0.276	0.0182
24	C4	4	0.683	0.568	0.336	0.0221
25	C5	4	0.753	0.630	0.404	0.0171
26	C6	4	0.770	0.732	0.413	0.0093
27	C7	4	0.717	0.763	0.348	0.0173
28	C8	4	0.852	0.800	0.484	0.0089
29	C9	4	1.060	0.966	0.309	0.008
30	C10	4	1.180	0.929	0.163	0.0167
31	C11	4	1.156	0.799	0.226	0.0211
32	C13	4	0.352	0.699	0.020	0.0074
33	C14	4	0.272	0.766	0.088	0.0069
34	C17	4	0.235	0.427	0.068	0.006
35	C18	4	0.113	0.466	0.032	0.0046
36	C19	4	0.114	0.459	-0.055	0.0107
37	C22	4	0.001	0.504	0.086	0.0117
38	C23	4	1.129	0.896	0.235	0.0126
39	C24	4	1.220	0.733	0.157	0.0212
40	C31	4	1.262	0.927	0.567	0.0111
41	C32	4	1.385	0.967	0.533	0.0044
42	C33	4	1.498	1.009	0.585	0.0103
43	C34	4	1.385	0.957	0.446	0.0123
44	C37	4	1.247	0.864	0.093	0.0175
45	C39	4	0.319	0.176	-0.040	0.041
46	C41	4	1.183	0.681	0.460	0.0322
47	C43	4	0.963	0.781	0.756	0.0435
48	C45	4	1.229	0.593	0.405	0.0575
49	C47	4	0.266	0.090	-0.095	0.0616
50	C48	4	1.191	0.750	0.733	0.0469
51	C49	4	1.079	0.718	0.841	0.0389
52	N3	5	1.198	0.715	0.814	0.0691

Table B.5: The interatomic distances of Ni(TPA)·DMF are listed.

A	B	Distance
O5	C9	1.271
O5	Ni1	2.026
O6	C9	1.262
O12	C31	1.246
O15	C13	1.351
O15	Ni4	1.991
O16	C8	1.285
O16	Ni1	1.998
O17	C31	1.228
O17	Ni1	2.098
O18	C1	1.257
O18	Ni4	2.087
O20	C13	1.223
O20	Ni2	2.040
O21	C8	1.284
O21	Ni6	1.957
O22	C1	1.244
O22	Ni2	2.012
O23	C39	1.123
O23	Ni4	2.035
O24	Ni4	1.895
O25	C48	1.277
O25	C43	1.353
O25	Ni6	1.934
O26	C41	1.100
O26	Ni6	2.039
O27	C17	1.241
O35	C17	1.137
Ni1	O16	1.998
Ni1	O16	1.998
Ni1	O5	2.026
Ni1	O5	2.026
Ni1	O17	2.098
Ni1	O17	2.098
Ni2	O22	2.012
Ni2	O22	2.012
Ni2	O20	2.040
Ni2	O20	2.040
Ni4	O24	1.895
Ni4	O15	1.991
Ni4	O23	2.035
Ni4	O18	2.087
Ni6	O25	1.934
Ni6	O21	1.957
Ni6	O26	2.039
C1	O22	1.244
C1	O18	1.257
C1	C2	1.513
C2	C3	1.374
C2	C4	1.395
C2	C1	1.513
C3	C2	1.374
C3	C7	1.384
C4	C5	1.347
C4	C2	1.395
C5	C4	1.347
C5	C6	1.430
C6	C7	1.378
C6	C5	1.430
C6	C8	1.467
C7	C6	1.378
C7	C3	1.384
C8	O21	1.284
C8	O16	1.285
C8	C6	1.467
C9	O6	1.262
C9	O5	1.271
C9	C23	1.464
C10	C37	1.377
C10	C23	1.472
C11	C24	1.368
C11	C23	1.372
C13	O20	1.223
C13	O15	1.351
C13	C14	1.435
C14	C37	1.399
C14	C13	1.435
C14	C24	1.445
C17	O35	1.137
C17	O27	1.241
C17	C18	1.501
C18	C19	1.390
C18	C22	1.409
C18	C17	1.501
C19	C22	1.375
C19	C18	1.390
C22	C19	1.375
C22	C18	1.409
C23	C11	1.372
C23	C9	1.464
C23	C10	1.472
C24	C11	1.368
C24	C14	1.445
C31	O17	1.228
C31	O12	1.246
C31	C32	1.488
C32	C33	1.379
C32	C34	1.393
C32	C31	1.488
C33	C32	1.379
C33	C34	1.384
C34	C33	1.384
C34	C32	1.393
C37	C10	1.377
C37	C14	1.399
C39	O23	1.123
C39	C47	1.354
C41	O26	1.100
C41	C45	1.364
C43	O25	1.353
C45	C41	1.364
C47	C39	1.354
C48	O25	1.277
C48	N3	1.564
C49	N3	1.221
N3	C49	1.221
N3	C48	1.564

Table B.6: The interatomic angles of Ni(TPA)·DMF are listed.

A	B	C	Angle
C9	O5	Ni1	134.63
C13	O15	Ni4	123.06
C8	O16	Ni1	141.00
C1	O18	Ni4	131.69
C13	O20	Ni2	141.78
C8	O21	Ni6	125.94
C1	O22	Ni2	135.74
C39	O23	Ni4	121.00
C48	O25	C43	117.75
C48	O25	Ni6	119.90
C43	O25	Ni6	121.50
C41	O26	Ni6	124.88
O16	Ni1	O16	179.95
O16	Ni1	O5	86.68
O16	Ni1	O5	93.32
O16	Ni1	O5	93.32
O16	Ni1	O5	86.68
O5	Ni1	O5	179.97
O22	Ni2	O22	180.00
O22	Ni2	O20	86.61
O22	Ni2	O20	93.39
O22	Ni2	O20	93.39
O22	Ni2	O20	86.61
O20	Ni2	O20	180.00
O24	Ni4	O15	100.30
O24	Ni4	O23	88.03
O24	Ni4	O18	88.26
O15	Ni4	O23	90.04
O15	Ni4	O18	94.26
O23	Ni4	O18	174.77
O25	Ni6	O21	106.38
O25	Ni6	O26	95.40
O21	Ni6	O26	90.41
O22	C1	O18	127.26
O22	C1	C2	117.60
O18	C1	C2	115.12
C3	C2	C4	117.98
C3	C2	C1	118.71
C4	C2	C1	122.85
C2	C3	C7	120.96
C5	C4	C2	122.33
C4	C5	C6	119.45
C7	C6	C5	118.20
C7	C6	C8	120.49
C5	C6	C8	120.95
C3	C7	C6	120.79
O16	C8	O21	123.60
O16	C8	C6	116.69
O21	C8	C6	119.70
O6	C9	O5	127.16
O6	C9	C23	117.64
O5	C9	C23	115.20
C37	C10	C23	120.94
C24	C11	C23	124.57
O20	C13	O15	123.96
O20	C13	C14	119.06
O15	C13	C14	116.97
C37	C14	C13	123.31
C37	C14	C24	118.36
C13	C14	C24	118.27
O35	C17	O27	135.87
O35	C17	C18	100.97
O27	C17	C18	121.85
C19	C18	C22	122.19
C19	C18	C17	119.04
C22	C18	C17	118.67
C22	C19	C18	118.17
C19	C22	C18	119.54
C11	C23	C9	123.98
C11	C23	C10	115.84
C9	C23	C10	120.15
C11	C24	C14	119.21
O17	C31	O12	119.56
O17	C31	C32	121.95
O12	C31	C32	118.37
C33	C32	C34	119.86
C33	C32	C31	122.29
C34	C32	C31	117.83
C32	C33	C34	123.18
C33	C34	C32	116.95
C10	C37	C14	120.95
O23	C39	C47	127.17
O26	C41	C45	129.26
O25	C48	N3	121.63
C49	N3	C48	106.42

REFERENCES

[1] S. Hong, R. Reifenberger, W. Tian, S. Datta, J. I. Henderson, and C. P. Kubiak. Molecular conductance spectroscopy of conjugated, phenyl-based molecules on Au(111): the effect of end groups on molecular conduction. *Superlattices Microstruct.*, 28(4):289–303, **2000**.

[2] D. K. James and J. M. Tour. Electrical measurements in molecular electronics. *Chem. Mater.*, 16(23):4423–4435, **2004**.

[3] N. D. Lang and P. Avouris. Electrical conductance of individual molecules. *Phys. Rev. B*, 6412(12):125323–125329, **2001**.

[4] J. J. Stapleton, T. A. Daniel, S. Uppili, O. M. Cabarcos, J. Naciri, R. Shashidhar, and D. L. Allara. Self-assembly, characterization, and chemical stability of isocyanide-bound molecular wire monolayers on gold and palladium surfaces. *Langmuir*, 21(24):11061–11070, **2005**.

[5] A. S. Martin, J. R. Sambles, and G. J. Ashwell. Molecular rectifier. *Phys. Rev. Lett.*, 70(2):218–221, **1993**.

[6] J. O. Lee, G. Lientschnig, F. Wiertz, M. Struijk, R. A. J. Janssen, R. Egberink, D. N. Reinhoudt, P. Hadley, and C. Dekker. Absence of strong gate effects in electrical measurements on phenylene-based conjugated molecules. *Nano Lett.*, 3(2):113–117, **2003**.

[7] J. Chen, M. A. Reed, A. M. Rawlett, and J. M. Tour. Large on-off ratios and negative differential resistance in a molecular electronic device. *Science*, 286(5444):1550–1552, **1999**.

[8] R. L. Carroll and C. B. Gorman. The genesis of molecular electronics. *Angew. Chem., Int. Ed.*, 41(23):4379–4400, **2002**.

[9] C. J. F. Dupraz, U. Beierlein, and J. P. Kotthaus. Low temperature conductance measurements of self-assembled monolayers of 1,4-phenylene diisocyanide. *Chem. Phys. Chem.*, 4(11):1247–1252, **2003**.

[10] R. M. Metzger. Unimolecular electrical rectifiers. *Chem. Rev.*, 103(9):3803–3834, **2003**.

[11] S. R. Batten and K. S. Murray. Structure and magnetism of coordination polymers containing dicyanamide and tricyanomethanide. *Coord. Chem. Rev.*, 246(1-2):103–130, **2003**.

[12] P. H. Dinolfo, M. E. Williams, C. L. Stern, and J. T. Hupp. Rhenium-based molecular rectangles as frameworks for ligand-centered mixed valency and optical electron transfer. *J. Am. Chem. Soc.*, 126(40):12989–13001, **2004**.

[13] T. Hirao. Conjugated systems composed of transition metals and redox-active pi-conjugated ligands. *Coord. Chem. Rev.*, 226(1-2):81–91, **2002**.

[14] R. P. Kingsborough and T. M. Swager. Transition metals in polymeric pi-conjugated organic frameworks. In *Prog. Inorg. Chem.*, volume 48 of *Progress in Inorganic Chemistry*, pages 123–231. Wiley-VCH, **1999**.

[15] A. Petitjean, F. Puntoriero, S. Campagna, A. Juris, and J. M. Lehn. Multicomponent supramolecular devices: Synthesis, optical, and electronic properties of bridged bis-dirhodium and -diruthenium complexes. *European Journal of Inorganic Chemistry*, (19):3878–3892, **2006**.

[16] R. Tannenbaum. Radiation enhancement of the catalytic properties of three-dimensional coordination polymers of Ru(II) with diisocyanide ligands. *J. Mol. Catal. A: Chem.*, 107(1-3):207–215, **1996**.

[17] I. Feinstein-Jaffe and A. Efraty. Electrical semiconductivity of stacked layer coordination polymers of rhodium(I). *Macromolecules*, 19(7):2076–2077, **1986**.

[18] S. Lawrence, K. Lott, and I. Feinstein-Jaffe. Novel polymeric complexes of rhodium(I)-cobalt(II) and 4,4'-diisocyanobiphenyl with good electrical conductivity. *Polyhedron*, 7(9):741–745, **1988**.

[19] S. A. Lawrence, K. A. K. Lott, P. A. Sermon, E. L. Short, and I. Feinstein-Jaffe. Electron delocalization in rhodium (1+) bis diisocyanobiphenyl chloride polymers with direct rhodium-rhodium interactions. *Polyhedron*, 6(11):2027–2029, **1987**.

[20] A. Efraty, I. Feinstein, L. Wackerle, and F. Frolow. Template polymerization of rhodium(I) with rigid bent diisocyanide ligands. *Angew. Chem., Int. Ed.*, 19(8):633–634, **1980**.

[21] A. Efraty and I. Feinstein. Catalytic hydrogenation and isomerization of 1-hexene with $[RhCl(CO)(1,4\text{-}(CN)_2C_6H_4)]_n$ in the dark and under irradiation. *Inorg. Chem.*, 21(8):3115–3118, **1982**.

[22] A. Efraty, I. Feinstein, F. Frolow, and L. Wackerle. Two-dimensional coordination polymers of rhodium(1+) with rigid collinear diisocyanide bridges and stacked layers arrangement. *J. Am. Chem. Soc.*, 102(20):6341–6343, **1980**.

[23] I. Feinstein-Jaffe, F. Frolow, L. Wackerle, A. Goldman, and A. Efraty. Tetragonal coordination polymers of rhodium(I) with stereochemically rigid aryl di-isocyanide linkages. *J. Chem. Soc., Dalton Trans.*, (2):469–476, **1988**.

[24] S. A. Lawrence, P. A. Sermon, and I. Feinstein-Jaffe. An investigation into the role of cooperative effects in polymeric rhodium(I) bis-4,4'-diisocyanobiphenyl chloride catalysts in olefin hydrogenation reactions. *J. Mol. Catal.*, 51(2):117–127, **1989**.

[25] R. Tannenbaum. The synthesis and characterization of some Ru(II) complexes containing carbon-monoxide and isocyanide groups. *Inorg. Chim. Acta*, 148(2):199–202, **1988**.

[26] C. G. Carson, R. A. Gerhardt, and R. Tannenbaum. Chemical stability and characterization of rhodium-diisocyanide coordination polymers. *Journal of Physical Chemistry, B*, 111:14114–14121, **2007**.

[27] G. Ferey, C. Mellot-Draznieks, C. Serre, and F. Millange. Crystallized frameworks with giant pores: Are there limits to the possible? *Accounts of Chemical Research*, 38(4):217–225, **2005**.

[28] H. Li, M. Eddaoudi, M. O'Keeffe, and O. M. Yaghi. Design and synthesis of an exceptionally stable and highly porous metal-organic framework. *Nature*, 402(6759):276–279, **1999**.

[29] C. N. R. Rao, S. Natarajan, and R. Vaidhyanathan. Metal carboxylates with open architectures. *Angewandte Chemie-International Edition*, 43(12):1466–1496, **2004**.

[30] W. Mori and S. Takamizawa. Microporous materials of metal carboxylates. *Journal of Solid State Chemistry*, 152(1):120–129, **2000**.

[31] G. Ferey, M. Latroche, C. Serre, F. Millange, T. Loiseau, and A. Percheron-Guegan. Hydrogen adsorption in the nanoporous metal-benzenedicarboxylate $M(OH)(O_2C\text{-}C_6H_4\text{-}CO_2)$ (M = Al^{3+}, Cr^{3+}), MIL-53. *Chemical Communications*, (24):2976–2977, **2003**.

[32] M. Frisch and C. L. Cahill. Syntheses, structures and fluorescent properties of two novel coordination polymers in the U-Cu-H(3)pdc system. *Dalton Transactions*, (8):1518–1523, **2005**.

[33] L. Alaerts, E. Seguin, H. Poelman, F. Thibault-Starzyk, P. A. Jacobs, and D. E. De Vos. Probing the lewis acidity and catalytic activity of the metal-organic framework $[Cu_3(btc)_2]$ (BTC = benzene-1,3,5-tricarboxylate). *Chemistry-A European Journal*, 12(28):7353–7363, **2006**.

[34] R. J. Acheson and A. K. Galwey. Thermal decomposition of nickel terephthalate and nickel salts of other carboxylic acids. *Journal of the Chemical Society a -Inorganic Physical Theoretical*, (7):1174–1179, **1967**.

[35] F. G. Sherif. Heavy metal terephthalates. *Industrial & Engineering Chemistry Product Research and Development*, 9(3):408–421, **1970**.

[36] S. Cueto, V. Gramlich, W. Petter, F. S. Rys, and P. Rys. Structure of copper(II) terephthalate trihydrate. *Acta Crystallographica Section C-Crystal Structure Communications*, 47:75–78, **1991**.

[37] O. M. Yaghi, G. M. Li, and H. L. Li. Selective binding and removal of guests in a microporous metal-organic framework. *Nature*, 378(6558):703–706, **1995**.

[38] O. M. Yaghi and H. L. Li. Hydrothermal synthesis of a metal-organic framework containing large rectangular channels. *Journal of the American Chemical Society*, 117(41):10401–10402, **1995**.

[39] O. M. Yaghi, C. E. Davis, G. M. Li, and H. L. Li. Selective guest binding by tailored channels in a 3-D porous zinc(II)-benzenetricarboxylate network. *Journal of the American Chemical Society*, 119(12):2861–2868, **1997**.

[40] O. M. Yaghi, H. L. Li, C. Davis, D. Richardson, and T. L. Groy. Synthetic strategies, structure patterns, and emerging properties in the chemistry of modular porous solids. *Accounts of Chemical Research*, 31(8):474–484, **1998**.

[41] H. Li, M. Eddaoudi, T. L. Groy, and O. M. Yaghi. Establishing microporosity in open metal-organic frameworks: Gas sorption isotherms for Zn(BDC) (BDC = 1,4-benzenedicarboxylate). *Journal of the American Chemical Society*, 120(33):8571–8572, **1998**.

[42] W. Mori, F. Inoue, K. Yoshida, H. Nakayama, S. Takamizawa, and M. Kishita. Synthesis of new adsorbent copper(II) terephthalate. *Chemistry Letters*, (12):1219–1220, **1997**.

[43] M. Edgar, R. Mitchell, A. M. Z. Slawin, P. Lightfoot, and P. A. Wright. Solid-state transformations of zinc 1,4-benzenedicarboxylates mediated by hydrogen-bond-forming molecules. *Chemistry-a European Journal*, 7(23):5168–5175, **2001**.

[44] S. M. Hawxwell, H. Adams, and L. Brammer. Two-dimensional metal-organic frameworks containing linear dicarboxylates. *Acta Crystallographica Section B-Structural Science*, 62:808–814, **2006**.

[45] H. F. Clausen, R. D. Poulsen, A. D. Bond, M. A. S. Chevallier, and B. B. Iversen. Solvothermal synthesis of new metal organic framework structures in the zinc-terephthalic acid-dimethyl formamide system. *Journal of Solid State Chemistry*, 178(11):3342–3351, **2005**.

[46] U. Mueller, M. Schubert, F. Teich, H. Puetter, K. Schierle-Arndt, and J. Pastre. Metal-organic frameworks - prospective industrial applications. *Journal of Materials Chemistry*, 16(7):626–636, **2006**.

[47] S. Kitagawa, R. Kitaura, and S. Noro. Functional porous coordination polymers. *Angewandte Chemie-International Edition*, 43(18):2334–2375, **2004**.

[48] L. Pan, B. S. Finkel, X. Y. Huang, and J. Li. The first pillared three-dimensional structure constructed by carboxylate ligands bridging heterometallic trilayers. *Chemical Communications*, (01):105–106, **2001**.

[49] W. J. Feng, Y. Xu, G. P. Zhou, C. L. Zhang, and X. F. Zheng. Hydrothermal synthesis, crystal structure and strong blue fluorescence of a novel 3D coordination polymer containing copper and zinc centers linked by isonicotinic acid ligands. *Inorganic Chemistry Communications*, 10(1):49–52, **2007**.

[50] G. L. Wang, X. L. Yang, Y. Liu, Y. Z. Li, H. B. Du, and X. Z. You. A 3d-3d heterometallic organic framework consisting of two cross-linked coordination polymers. *Inorganic Chemistry Communications*, 11(7):814–817, **2008**.

[51] N. Kourkoumelis. Powdll 2.19. http://users.uoi.gr/nkourkou/powdll.htm, **2005**.

[52] D. Briggs. *Surface analysis of polymers by XPS and static SIMS*. Cambridge University Press, Cambridge, UK, **1998**. Clarke, D. R. and Suresh, S. and Ward, I. M.

[53] C. G. Carson, R. A. Gerhardt, and R. Tannenbaum. Dielectric properties of [Rh(1,4-diisocyanobenzene)$^{+}_{4/2}$(Cl)$^{-}$]$_n$ with respect to moisture. In *Abstracts of Papers, 233 ACS National Meeting*, page 148. ACS, American Chemical Society, Chicago, IL, **2007**.

[54] A. K. Jonscher. *Dielectric Relaxation in Solids*. Chelsea Dielectrics Press, London, UK, **1983**.

[55] W. Q. Cao and R. Gerhardt. Calculation of various relaxation-times and conductivity for a single dielectric-relaxation process. *Solid State Ionics*, 42(3-4):213–221, **1990**.

[56] R. A. Gerhardt. Impedance spectroscopy and mobility spectra. In P. W. G. Bassani, G. Leidl, editor, *Encyclopedia of Condensed Matter Physics*, page 350. Elsevier, Boston, **2005**. ISBN 0122276108.

[57] R. Gerhardt. Impedance and dielectric-spectroscopy revisited - distinguishing localized relaxation from long-range conductivity. *J. Phys. Chem. Solids*, 55(12):1491–1506, **1994**.

[58] A. Dakhel and Y. Ali-Mohamed Ahmed. Electrical properties of thermally evaporated nickel-dimethylglyoxime thin films. *J. Phys. Chem. Solids*, 66(6):1080–1084, **2005**.

[59] C. Diaz, M. L. Valenzuela, and M. Barbosa. A facile organometallic-induced cross-linking of copolymers of phosphazene. *Mater. Res. Bull.*, 39(1):9–19, **2004**.

[60] J. A. Crayston, D. C. Cupertino, and H. S. Forster. Synthesis, characterization and electrical-conductivity of ruthenium coordination polymers. *Synth. Met.*, 35(3):365–370, **1990**.

[61] A. Bansod and A. Aswar. Synthesis, thermal, electrical and catalytic studies of some transition metal polychelates of bis-bidentate schiff base. *Chin. J. Chem.*, 25(2):154–158, **2007**.

[62] I. Jaffe. Aryl diisocyanide organometallic coordination polymers. *Rev. Inorg. Chem.*, 13(1):1, **1993**.

[63] V. Huc, J. P. Bourgoin, C. Bureau, F. Valin, G. Zalczer, and S. Palacin. Self-assembled mono- and multilayers on gold from 1,4-diisocyanobenzene and ruthenium phthalocyanine. *J. Phys. Chem. B*, 103(47):10489–10495, **1999**.

[64] S. Lin and R. L. McCarley. Surface-confined monomers on electrode surfaces. 6. adsorption and polymerization of 1,6-diisocyanohexane on Au and Pt. *Langmuir*, 15(1):151–159, **1999**.

[65] L. Pranger, A. Goldstein, and R. Tannenbaum. Competitive self-assembly of symmetrical, difunctional molecules on ambient copper surfaces. *Langmuir*, 21(12):5396–5404, **2005**.

[66] L. Pranger and R. Tannenbaum. Self-assembly of 1,4-phenylene diisocyanide and terephthalic acid on Ni, Cu and Pt. *J. Colloid Interface Sci.*, 292(1):71–78, **2005**.

[67] M. A. Ansell, E. B. Cogan, and C. J. Page. Coordinate covalent cobalt-diisocyanide multilayer thin films grown one molecular layer at a time. *Langmuir*, 16(3):1172–1179, **2000**.

[68] S. M. Gruenbaum, M. H. Henney, S. Kumar, and S. Z. Zou. Surface-enhanced raman spectroscopic study of 1,4-phenylene diisocyanide adsorbed on gold and platinum-group transition metal electrodes. *J. Phys. Chem. B*, 110(10):4782–4792, **2006**.

[69] M. J. Robertson and R. J. Angelici. Adsorption of aryl and alkyl isocyanides on powdered gold. *Langmuir*, 10(5):1488–1492, **1994**.

[70] S. Semancik, G. L. Haller, and J. T. Yates. The adsorption and dissociation of methyl isocyanide on Rh(111). *J. Chem. Phys.*, 78(11):6970–6981, **1983**.

[71] K. Onitsuka, T. Mori, M. Yamamoto, F. Takei, and S. Takahashi. Helical sense selective polymerization of bulky aryl isocyanide possessing chiral ester or amide groups initiated by arylrhodium complexes. *Macromolecules*, 39(21):7224–7231, **2006**.

[72] K. Onitsuka, M. Yamamoto, T. Mori, F. Takei, and S. Takahashi. Living polymerization of bulky aryl isocyanide with arylrhodium complexes. *Organometallics*, 25(5):1270–1278, **2006**.

[73] J. Tabei, M. Shiotsuki, F. Sanda, and T. Masuda. Determination of helical sense of poly(N-propargylamides) by exciton-coupled circular dichroism. *Macromolecules*, 38(23):9448–9454, **2005**.

[74] R. Arshady, M. Zecca, and B. Corain. Polymeric isocyanides - synthesis, properties and applications. *React. Polym.*, 20(3):147–173, **1993**.

[75] J. A. Crayston, D. C. Cupertino, and T. J. Dines. Infrared and resonance raman-spectroscopic characterization of electronically conducting ruthenium(II) coordination polymers. *Dalton Trans.*, (6):1603–1608, **1991**.

[76] H. A. Pohl and M. Pollak. Nomadic polarization in quasi-one-dimensional solids. *J. Phys. Chem.*, 66(9):4031–4040, **1977**.

[77] J. Rasko and J. Kiss. Adsorption and surface reactions of acetonitrile on Al_2O_3-supported noble metal catalysts. *Applied Catalysis A-General*, 298:115–126, **2006**.

[78] D. T. Clark and A. Harrison. ESCA applied to polymers. a theoretical investigation of molecular core binding and relaxation energies in a series of prototype systems for nitrogen and oxygen functionalities in polymers. *J. Polym. Sci. Polym. Chem.*, 19(8):1945–1955, **1981**.

[79] S. Cueto, P. Rys, F. S. Rys, R. Sanjinez, and H. P. Straumann. Electrical and magnetic-properties of new copper arylcarboxylates. *Journal of Magnetism and Magnetic Materials*, 104:1096–1097, **1992**.

[80] W. Mori, T. Sato, C. N. Kato, T. Takei, and T. Ohmura. Discovery and development of microporous metal carboxylates. *Chemical Record*, 5(6):336–351, **2005**.

[81] L. Deakin, A. M. Arif, and J. S. Miller. Observation of ferromagnetic and antiferromagnetic coupling in 1-d and 2-d extended structures of copper(II) terephthalates. *Inorganic Chemistry*, 38(22):5072–5077, **1999**.

[82] S. M. Hawxwell and L. Brammer. Solvent hydrolysis leads to an unusual Cu(II) metal-organic framework. *Crystengcomm*, 8(6):473–476, **2006**.

[83] L. Gao, B. J. Zhao, G. H. Li, Z. Shi, and S. H. Feng. Mixed solvothermal synthesis and x-ray characterization of a layered copper coordination polymer, $Cu(H_2O)$(1,3-BDC)$\cdot H_2O$ (BDC = benzenedicarboxylate). *Inorganic Chemistry Communications*, 6(9):1249–1251, **2003**.

[84] K. Seki. Design of an adsorbent with an ideal pore structure for methane adsorption using metal complexes. *Chemical Communications*, 30(16):1496–1497, **2001**.

[85] A. Domenech, H. Garcia, M. T. Domenech-Carbo, and F. Llabres-i Xamena. Electrochemistry nanometric patterning of MOF particles: Anisotropic metal electrodeposition in Cu/MOF. *Electrochemistry Communications*, 8(12):1830–1834, **2006**.

[86] H. Ding, W. Chen, Q. Yue, J. S. Chen, and S. N. Wang. Synthesis, structure and photoluminescence of two zinc carboxylate polymers with different coordination architectures. *Chinese Journal of Chemistry*, 21(10):1305–1308, **2003**.

[87] J. Y. Sun, Y. M. Zhou, Q. R. Fang, Z. X. Chen, L. H. Weng, G. S. Zhu, S. L. Qiu, and D. Y. Zhao. Construction of 3D layer-pillared homoligand coordination polymers from a 2D layered precursor. *Inorganic Chemistry*, 45(21):8677–8684, **2006**.

[88] C. G. Carson, K. Hardcastle, J. Schwartz, X. T. Liu, C. Hoffmann, R. A. Gerhardt, and R. Tannenbaum. Synthesis and structure characterization of copper terephthalate metal organic frameworks. *European Journal of Inorganic Chemistry*, **2009**. In press.

[89] O. Kahn. *Molecular Magnetism*. VCH, New York, NY, **1993**.

[90] S. C. Manna, J. Ribas, E. Zangrando, and N. R. Chaudhuri. Supramolecular networks of dinuclear copper(II): Synthesis, crystal structure and magnetic study. *Inorganica Chimica Acta*, 360(8):2589–2597, **2007**.

[91] S. S. Y. Chui, S. M. F. Lo, J. P. H. Charmant, A. G. Orpen, and I. D. Williams. A chemically functionalizable nanoporous material $[Cu_3(TMA)_2(H_2O)_3]_n$. *Science*, 283(5405):1148–1150, **1999**.

[92] B. Panella, M. Hirscher, H. Pütter, and U. Müller. Hydrogen adsorption in metalorganic frameworks: Cu-MOFs and Zn-MOFs compared. *Advanced Func Materials*, 16(4):520–524, **2006**.

[93] H. Kumagai, M. A. Tanaka, K. Inoue, H. Takahashi, K. Kobayashi, S. Vilminot, and K. Mohamedally. Metal-organic frameworks from copper dimers with cis- and trans-1,4- cyclohexanedicarboxylate and cis,cis-1,3,5-cyclohexanetricarboxylate. *Inorganic Chemistry*, 46(15):5949–5956, **2007**.

[94] J. Cano, G. DeMunno, J. L. Sanz, R. Ruiz, J. Faus, F. Lloret, M. Julve, and A. Caneschi. Ability of terephthalate (ta) to mediate exchange coupling in ta-bridged copper(II), nickel(II), cobalt(II) and manganese(II) dinuclear complexes. *Journal of the Chemical Society, Dalton Transactions: Inorganic Chemistry*, (11):1915–1923, **1997**.

[95] Z. L. Huang, M. Drillon, N. Masciocchi, A. Sironi, J. T. Zhao, P. Rabu, and P. Panissod. Ab-initio XRPD crystal structure and giant hysteretic effect (H-c=5.9 T) of a new hybrid terephthalate-based cobalt(II) magnet. *Chemistry of Materials*, 12(9):2805–2812, **2000**.

[96] A. Carton, A. Mesbah, T. Mazet, F. Porcher, and M. Francois. Ab initio crystal structure of nickel(II) hydroxy-terephthalate by synchrotron powder diffraction and magnetic study. *Solid State Sciences*, 9(6):465–471, **2007**.

[97] S. Abdelouhab, M. Francois, E. Elkaim, and P. Rabu. Ab initio crystal structure of copper(II) hydroxy-terephthalate by synchrotron powder diffraction and magnetic properties. *Solid State Sciences*, 7(2):227–232, **2005**.

[98] Y. L. Fu, J. L. Ren, and S. W. Ng. The 1 : 1 adduct of cobalt(II) terephthalate with N,N-dimethylformamide. *Acta Crystallographica Section E-Structure Reports Online*, 60:M1507–M1509, **2004**.

[99] R. P. Davies, R. J. Less, P. D. Lickiss, and A. J. P. White. Framework materials assembled from magnesium carboxylate building units. *Dalton Transactions*, (24):2528–2535, **2007**.

[100] X. F. Zhou, J. A. Krauser, D. R. Tate, A. S. VanBuren, P. R. Clark, J. A. Moody, and L. R. F. Theoretical study of the structure and vibrational spectrum of N,N-dimethylformamide. *Journal of Physical Chemistry*, 100(42):16822–16827, **1996**.

[101] G. Durgaprasad, D. N. Sathyanaranya, and C. C. Patel. Infrared spectra and normal vibrations of n,n-dimethylformamide and n,n-dimethylthioformamide. *Bull. Chem. Soc. Japan*, 44(2):316–322, **1671**.

[102] G. N. R. Tripathi and S. J. Sheng. Solid-state vibrational spectra and structures of terephthalic acid and the terephthalate ion. *J. Mol. Struct*, 15(12):21–34, **1979**.

[103] G. Varsanyi. *Assignments for Vibrationals Spectra of Seven Hundred Benzene Derivatives*, volume 1. John Wiley & Sons, New York, **1974**.

[104] T. Ogata, T. Taga, and K. Osaki. Cation distribution in mixed formates .1. change in lattice-constants and in ir-spectra with chemical constitution of (Cu,MII)$(HCOO)_2 \cdot 2H_2O$. *Bulletin of the Chemical Society of Japan*, 50(7):1674–1679, **1977**.

[105] T. Ogata, T. Taga, and K. Osaki. Cation distribution in mixed formates .2. structure of mixed-crystal $Cu_{0.5}Zn_{0.5}(HCOO)_2 \cdot 2H_2O$. *Bulletin of the Chemical Society of Japan*, 50(7):1680–1682, **1977**.

[106] J. Cernak, J. Chomic, C. Kappenstein, and F. Robert. Copper zinc oxide catalysts: Preparation, structure and thermal properties of a zinc copper maleate precursor $Cu_{0.06}Zn_{0.94}C_4H_2 \cdot 2H_2O$. *Journal of the Chemical Society-Dalton Transactions*, (17):2981–2985, **1997**.

[107] S. Y. Yang, Z. G. Sun, L. S. Long, R. B. Huang, and L. S. Zheng. Crystal structure of a 3D coordination polymer: Sodium zinc terephthalate hydrate N,N-dimethylformamide solvate. *Main Group Metal Chemistry*, 25(9):579–580, **2002**.